VOLUME 11 JULY 2017

# nature photonics

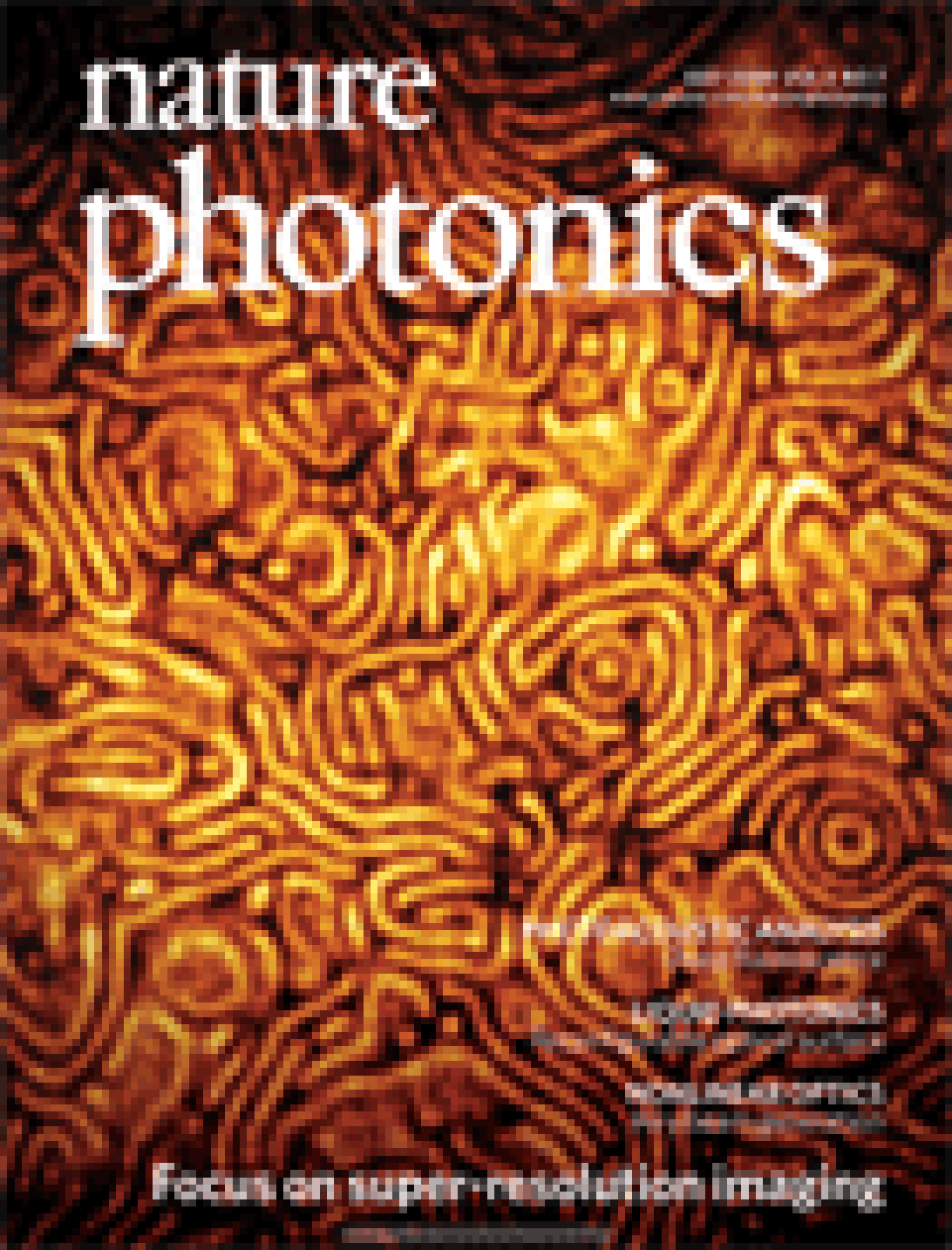

Focus on super-resolution imaging

nature photonics



**ORIGINAL RESEARCH TYPESET BY** Techset Composition Ltd, www.techset.co.uk
**PRINTED BY** Wyndeham Grange, www.wyndeham.co.uk

FOCUS
SUPER-RESOLUTION
IMAGING

JULY 2009 VOL 3 ISSUE 7

nature photonics

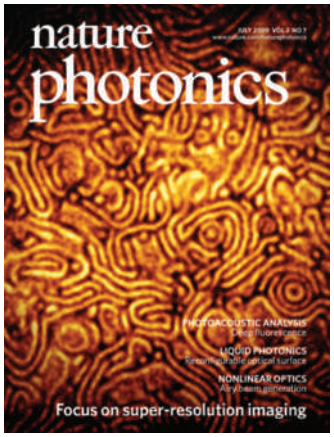


**COVER IMAGE**

**The advent of super-resolution imaging schemes that allow optical imaging beyond the diffraction limit of light is revolutionizing sample analysis in the biological and physical sciences. This issue features a special focus on the topic.**

Editorial p361;
Commentary p362 and p365;
Interview p368;
Progress Article p381;
Review Article p388

**ON THE COVER**

**Photoacoustic analysis**
Deep fluorescence
Article p412; News & Views p378

**Liquid photonics**
Reconfigurable optical surfaces
Letter p403; Interview p420

**Nonlinear optics**
Airy beam generation
Letter p395; News & Views p374

**Could 'off-the-shelf' LEGO blocks be a light-weight, cost-effective solution for constructing educational experiments in photonics? Researchers in Japan think so.**
News & Views p377

**The generation of X-ray laser light from the LCLS facility in the US is an important milestone in the evolution of free electron lasers.**
News & Views p375

## LETTERS



## ARTICLES



## PRODUCT FOCUS



## INTERVIEW



## CLASSIFIEDS

See the back pages


nature publishing group

*Nature Photonics* (ISSN 1749-4885) is published monthly by Nature Publishing Group (Porters South, 4 Crinan Street, London N1 9XW, UK). Editorial Office: Chiyoda Building, 5-6th Floor, 2-37 Ichigaya Tamachi, Shinjuku-ku, Tokyo, 162-0843, Japan. Telephone: +81 (0)3 3267 8751. Fax: +81 (0)3 3267 8754. Email: naturephoton@nature.com. North American Advertising: *Nature Photonics*, 75 Varick Street, 9th Floor, New York, NY, 10013-1917, US. Telephone: +1 212 726 9200. Fax: +1 212 696 9006. European Advertising: *Nature Photonics*, Porters South, 4 Crinan Street, London N1 9XW, UK. Telephone: +44 (0)20 7833 4000. Fax: +44 (0)20 7843 4596. Asia-Pacific Advertising: *Nature Photonics*, Chiyoda Building, 5-6th Floor, 2-37 Ichigayatamachi, Shinjuku-ku, Tokyo, 162-0843, Japan. Telephone: +81 (0)3 3267 8754. Fax: +81 (0)3 3267 8746. New subscriptions/renewals/changes of address/back issues and all other customer service questions should be addressed to - North America: *Nature Photonics*, Subscriptions Department, PO Box 5054, Brentwood, TN 37024-5054, USA. Outside North America: Subscriptions Department, Brunel Road, Basingstoke, Hants. RG21 6XS, UK. Telephone: +44 (0)1256 329242; Fax: +44 (0)1256 812358: Nature Asia-Pacific, Chiyoda Building, 5-6th Floor, 2-37 Ichigayatamachi, Shinjuku-ku, Tokyo, 162-0843, Japan. Telephone +81 (0)3 3267 8751. Annual subscription rates: US/Canada US$3060, Canada add 5% GST (institutional/corporate), US$152, Canada add 5% GST (individual making personal payment); UK/Rest of World (excluding Europe and Japan) £1570 (institutional/corporate), £78 (individual making personal payment); Europe €2430 (institutional/corporate), €121 (individual making personal payment). Back issues: US/Canada $45, Canada add 5% GST; Rest of World: surface mail US$43, air mail US$45. *Nature Photonics* (ISSN 1749-4885) is published monthly by Nature Publishing Group, c/o Mercury Airfreight International Ltd, 365 Blair Road, Avenel, NJ 07001, USA. Periodicals postage is paid at Rahway NJ. Postmaster: send address changes to *Nature Photonics*, c/o Mercury Airfreight International, 365 Blair Road, Avenel, NJ 07001, USA. Reprints: *Nature Photonics* Reprints Department, Porters South, 4 Crinan Street, London N1 9XW, UK. Subscription information is available at the *Nature Photonics* homepage at http://www.nature.com/naturephotonics. Postmaster: send address changes to *Nature Photonics* Subscriptions Department, Brunel Road, Basingstoke, Hants. RG21 6XS, UK or *Nature Photonics* Subscriptions Department PO Box 5054, Brentwood, TN 37024-5054, USA.

# Beyond the diffraction limit

The emergence of imaging schemes capable of overcoming Abbe's diffraction barrier is revolutionizing optical microscopy.

In 1873, the German physicist Ernst Abbe realized that the resolution of optical imaging instruments, including telescopes and microscopes, is fundamentally limited by the diffraction of light. His finding indicated that ultimately the resolution of an imaging instrument is not constrained by the quality of the instrument, but by the wavelength of light used and the aperture of its optics. This meant that a microscope could not resolve two objects located closer than $\lambda/2NA$, where $\lambda$ is the wavelength of light and NA is the numerical aperture of the imaging lens.

This diffraction-limited phenomenon hindered the performance of optical microscopy for over a century, and was considered a fundamental, unbreakable rule. Recently, however, several new exciting approaches in imaging have emerged that can 'break' this rule under certain circumstances. It now appears that there is no fundamental limit in achieving spatial resolution; using visible light, it is possible to resolve up to a few nanometres with these approaches.

To celebrate these developments, this issue features a focus on super-resolution imaging techniques that operate beyond the diffraction limit. A collection of articles on different imaging techniques — from far-field fluorescence to plasmonics — can be found. The collection consists of a review article, a progress article, two commentaries and an interview.

In the interview on page 368, W. E. Moerner highlights some of the incredible advantages of imaging when it is not limited by diffraction[1]. Such techniques not only allow non-invasive investigation of the interior of biological cells, but also promise nano-imaging of semiconductor devices in the electronics industry. Moerner elegantly summarizes the advantages and disadvantages of the various subdiffraction-limited imaging approaches developed to date, and also discusses the future outlook of such techniques.

When reading these articles, you will find that the techniques can be classified into several groups. First, there are near- and far-field approaches: the former operate close to the sample, often collecting evanescent signals that decay rapidly but contain extra information about the sample, whereas the latter collects optical signals (typically fluorescence) at a normal working distance. Fluorescence-based imaging techniques can then be further divided into separate categories according to how they view the nature of the specimen — either as a collection of single molecular labels or as a fluorophore of continuously varying density. Techniques that involve switching of optical signals can also be categorized on how they achieve signal separation — either by targeted signal switching or stochastic single-molecule switching.

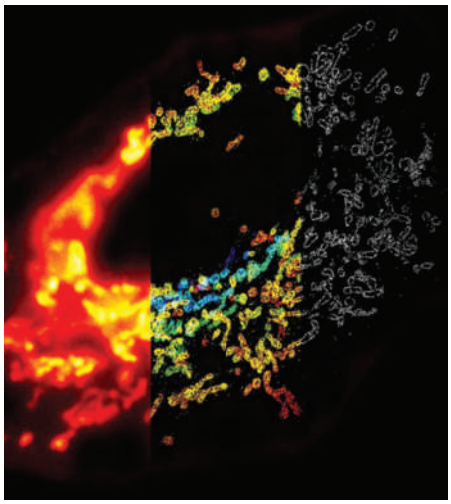

XIAOWEI ZHUANG / HARVARD UNIVERSITY

An approach that has undoubtedly caused much excitement within the far-field imaging community is stimulated emission depletion microscopy, pioneered by Stefan Hell. On page 381, Hell and colleagues review recent progress in three-dimensional imaging of transparent fluorescent objects using far-field nanoscopy[2]. They explain how two opposing lenses, combined with the switching (on and off) of fluorescence between adjacent markers, can overcome the diffraction barrier. Although the examples given are stimulated emission depletion microscopy and photoactivation localization microscopy, the authors anticipate that dual-lens schemes could be applied to other approaches and will, ultimately, become central to three-dimensional far-field optical imaging at the nanoscale.

In biology, stochastic optical reconstruction microscopy — a technique that uses single-molecule detection and photo-switchable probes to achieve high-resolution fluorescence imaging — now allows imaging of cell interiors to unprecedented levels of detail. On page 365, Xiaowei Zhuang explains how a spatial resolution of a few tens-of-nanometres can be achieved using this approach[3]. She also describes how multicolour, three-dimensional stochastic optical reconstruction microscopy can be put to good use for imaging molecular structures in cells.

On page 362, Rainer Heintzmann and Mats Gustafsson take a broader look at the problem of subdiffraction imaging and discuss what is necessary to make it possible. They explain how the use of a spatially non-uniform illumination and a sample with a nonlinear photoresponse are the only two fundamental requirements for super-resolution imaging of a spatially continuous fluorescence distribution[4].

Aside from fluorescence, surface plasmons (those that are either excited on the metallic surface or localized in a small metallic tip) also provide a method of overcoming the diffraction limit of light. The review article by Satoshi Kawata and co-workers on page 388 comments on the potential for plasmonics to improve imaging[5].

As Moerner explains in the interview, all these different approaches that image beyond the 'diffraction limit' are complementary. One thing is clear: the achievements of super-resolution imaging are narrowing the gap between optical microscopy and ultrahigh resolution imaging schemes (such as X-ray or electron microscopy), which rely on much shorter wavelengths than visible light. The arrival of super-resolution optical microscopes will make it possible to observe the world around us with a new level of clarity. This will almost certainly result in some very exciting new science, particularly within — but not limited to — the field of biology. ❐

## References


1. Won, R. *Nature Photon.* **3,** 368–369 (2009).
2. Stefan, W. H., Schmidt, R. & Egner, A. *Nature Photon.* **3,** 381–387 (2009).
3. Zhuang, X. *Nature Photon.* **3,** 365–367 (2009).
4. Heintzmann, R. & Gustafsson, M. G. L. *Nature Photon.* **3,** 362–364 (2009).
5. Kawata, S., Inouye, Y. & Verma, P. *Nature Photon.* **3,** 388–394 (2009).

# Subdiffraction resolution in continuous samples

Rainer Heintzmann and Mats G. L. Gustafsson

Super-resolution light microscopy methods either localize single molecular labels or treat the sample as a continuous object. The fundamental requirements for super-resolution in the continuum regime are spatially non-uniform illumination and a nonlinear photoresponse.

For over a century diffraction has been thought to limit the resolution of the image formed by a light microscope[1]. Only recently has it become clear that it does not in fact limit the resolution at which we can learn the structure of a specimen. There are now several methods of far-field light microscopy that have no fundamental limit to their potential spatial resolution, viewing the specimen either as a collection of single molecular labels or as a continuously varying density of fluorophore.

The location of a known object can be determined with great precision, given enough detected photons[2]. Turning localization precision into resolution requires a method of separating nearby labels (those that are too closely spaced to resolve) into images that can be localized separately. This is a well-established idea, originally investigated by using multiple labels that differ in some parameter such as emission wavelength[3–5] or fluorescence lifetime[6]; more recently, it has been studied through the important new concept of separating identical labels on the basis of their individual stochastic behaviour in time, using either photobleaching time[7] or reversible blinking[8]. This led to the breakthrough of modern techniques based on stochastic activation of fluorescence[9–11]. (See also the commentary article on page 365 of this issue[12].) Although localization-based methods[2–8] are powerful[9–11], they require a large number of raw images for each reconstruction, and may ultimately be limited by non-ideal properties of the activation labels.

The second category of super-resolution methods does not assume a single-molecule nature of the specimen, but instead treats it as a continuous density of fluorescence. The remainder of this article describes why there are only two fundamental physical requirements for achieving super-resolution in this continuum regime: spatially non-uniform illumination and a nonlinear photoresponse. To achieve theoretically unlimited resolution, the nonlinearity must be non-polynomial.

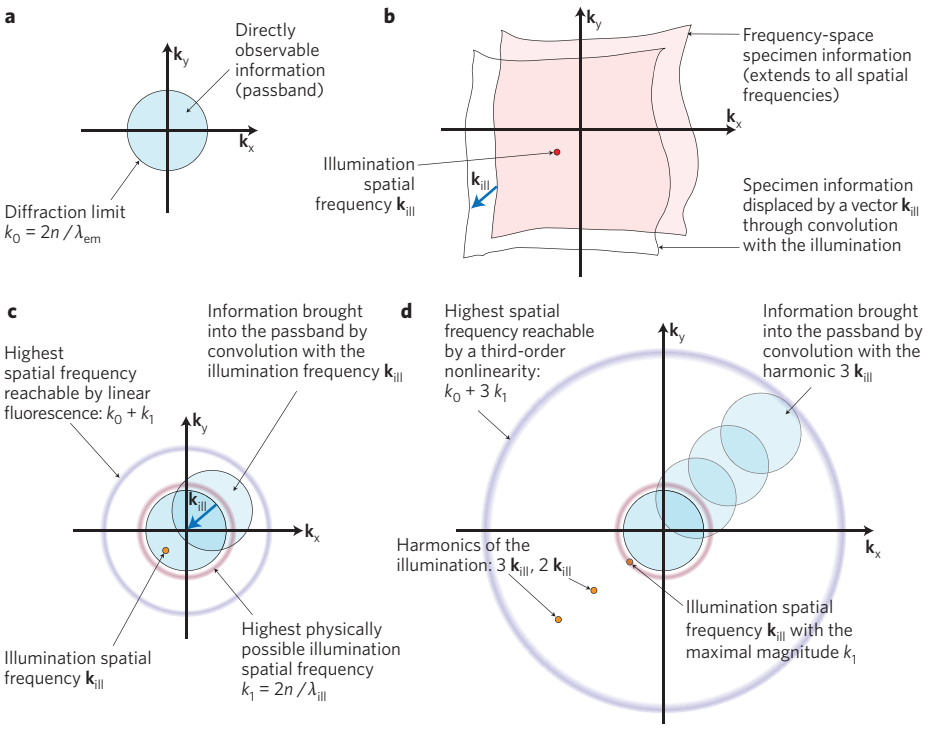


**Figure 1 |** Resolution extension by spatially non-uniform illumination and a nonlinear photoresponse. **a**, The diffraction-limited detection passband: the set of spatial frequenies in the emitting object about which the far-field light carries any information. This is a spherical region with radius $k_0 = 2n/\lambda_{em}$ in frequency space. **b**, Each frequency component $\mathbf{k}_{ill}$ of the illumination results in a copy of the specimen information being translated by the vector $\mathbf{k}_{ill}$. **c**, This translation will move specimen information into the detection passband from a new area of frequency space: a passband-shaped area centred at $-\mathbf{k}_{ill}$. The information from the part of this new area that lies outside the detection passband was previously unobservable. The resolution limit has thus been increased by an amount equal to the magnitude — the vector length — of $\mathbf{k}_{ill}$. Physical limits prevent the magnitude of $\mathbf{k}_{ill}$ from exceeding $k_1 = 2n/\lambda_{ill}$ in the context of linear fluorescence. **d**, If the emission rate per fluorophore depends nonlinearly on the illumination intensity, harmonics may be generated, which can shift correspondingly higher-resolution information into the detection passband. The highest order $m$ present in the Taylor expansion of the nonlinearity defines the highest harmonic order and thus the new resolution limit $k_0 + mk_1$. A nonlinearity with an infinite Taylor series allows, in principle, unlimited resolution.

The broadest definition of the classical diffraction limit is that the far-field light leaving a luminescent object carries information about only a finite set of spatial frequencies of the emitting object: those with magnitude below $k_0 = 2n/\lambda_{em}$ (where $\lambda_{em}$ is the emission wavelength and

$n$ is the refractive index of the sample). The only observable information about the emitting object's structure is that with spatial frequencies within a hard-edged passband of radius $k_0$. In a microscope that observes the sample from only a limited aperture half-angle $\alpha$, the cut–off spatial frequency (in the two-dimensional image plane) is reduced by a factor $\sin(\alpha)$ to $k_0' = 2n\sin(\alpha)/\lambda_{em} = 2\mathrm{NA}/\lambda_{em}$, where $\mathrm{NA} = n\sin(\alpha)$ is known as the numerical aperture of the objective.

All continuum-regime imaging techniques that transcend this limit are based on a single physical principle — frequency mixing with non-uniform illumination intensity. This 'loophole' exists because the emitting object, to which the diffraction limit applies, differs from the specimen of interest — typically a spatial distribution of fluorophore density — if the illumination is non-uniform.

With normal linear fluorescence, the local emission intensity from a specimen is the product of the fluorophore density and the local intensity of illumination light at the excitation wavelength. If the illumination intensity is uniform, the product constitutes a trivial multiplication by a constant, however a spatially non-uniform illumination intensity has non-trivial effects. By the convolution theorem, the point-wise real-space product of the specimen and the illumination intensity corresponds, in frequency space, to a convolution of their spatial frequency information[14]. The convolution is mathematically non-local, and can therefore make the observable information within the detection passband depend on spatial frequency components of the specimen that reside outside this passband. By moving it into the detection passband, information outside the passband (otherwise inaccessible) can, in principle, be observed (Fig. 1)[15,16]. This phenomenon is the underlying physical basis for the enlarged passband of confocal microscopy[17] and other point-scanning techniques (in which the non-uniform illumination intensity consists of a focused beam), structured-illumination microscopy (in which the illumination intensity typically consists of a periodic pattern; see Box 1)[15,16,18,19] and all microscopy techniques involving scan lines, spot arrays[20] or other forms of non-uniform illumination.

**Box 1 | Structured-illumination microscopy**

Structured-illumination microscopy (SIM) is a practical microscopy technique that explicitly applies the frequency-space principles outlined in this article (Fig. B1a–h). The specimen is observed under a series of periodic illumination patterns. Each pattern comprises a small number of spatial frequencies, each of which causes a specific region of frequency space to be translated into the detection passband (Fig. 1a–c). All the information is transmitted together by the microscope within its normal detection passband (Fig. B1c). By phase-shifting the pattern, the contributions from different regions can be separated (Fig. B1d,e) and computationally restored to their proper position in frequency space (Fig. B1f). The reassembled information covers an enlarged area of frequency space (Fig. B1f) and results in an extended-resolution reconstruction (Fig. B1g).

A three-dimensional version of linear SIM has produced reconstructions of otherwise unresolvable cellular structures (Fig. B1i–k)[31]. For thin specimens, SIM can be used to study the dynamics of live processes at multi-hertz rates over hundreds of time frames (Fig. B1g,h)[30].

Nonlinear SIM (NLSIM) operates through the same process, but produces higher resolution by exploiting a nonlinear photoresponse to generate harmonics of the illumination frequencies (Fig. 1d). A form of NLSIM that uses saturation of the excited state as the nonlinear response has demonstrated 50-nm resolution (Fig. B1l–o)[24], and other nonlinearities could be used in the same manner.

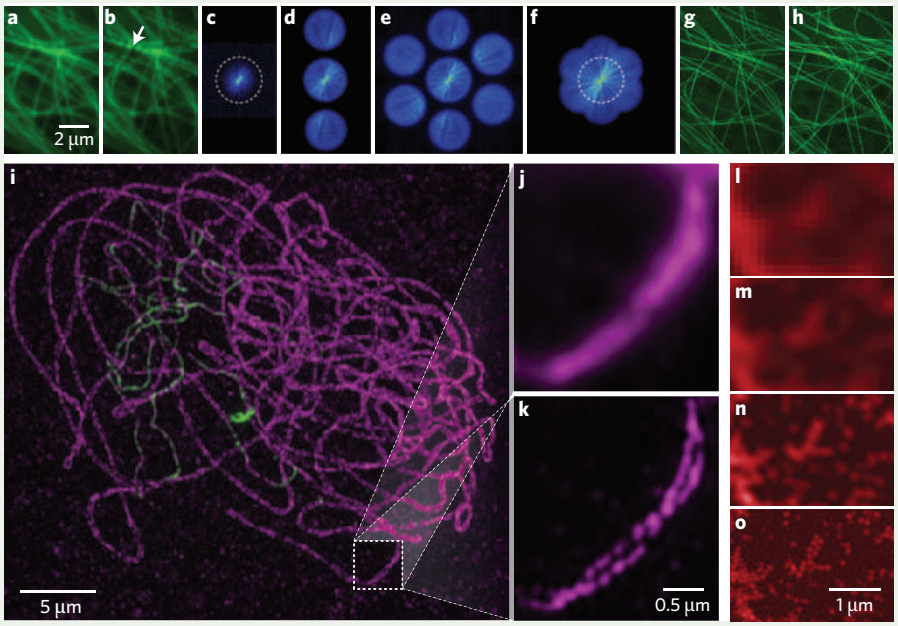


**Figure B1 |** Method and examples of SIM. **a**–**h**, The SIM procedure. **a**, A conventional total internal reflection fluorescence (TIRF) image of a living S2 cell expressing green fluorescent protein (GFP)–tubulin. **b**, The same cell illuminated by a horizontal stripe pattern, showing moiré effects (arrow). **c**, A Fourier transform of **b**, with the diffraction limit shown as a dashed circle. **d**, Three orders of information, separated based on horizontal patterns. **e**, Seven orders of information, separated based on three pattern orientations. **f**, Reassembled information orders, extending beyond the diffraction limit. **g**, The resulting real-space reconstruction. **h**, The same cell 120 s later (from a 120-frame 1-Hz video) (ref. 30). **i**–**k**, Three-dimensional SIM. Maximum-intensity projection through an entire maize cell nucleus, showing the synaptonemal complex (SC). The lateral elements of the SC form a zipper-like structure with a separation of approximately 170 nm, which is unresolvable by conventional microscopy (**j**) but is well resolved by SIM[31] (**k**). **l**–**o**, Nonlinear SIM. 50-nm fluorescent beads, as seen by conventional microscopy (**l**), conventional microscopy plus filtering (**m**), linear SIM (**n**) and by nonlinear SIM in which saturation of the exited state was exploited to produce two additional harmonics[24] (**o**). Images **a**–**h** re-rendered with permission from ref. 30. © 2009 NPG. Images **i**–**k** and **l**–**o** reproduced with permission from, respectively, ref. 31. © 2008 ELSEVIER; and ref. 24. © 2005 PNAS.

Within the context of linear fluorescence, the spatial frequency increase by which it can enlarge the effective passband is precisely equal to the highest spatial frequency present in the illumination (Fig. 1). Unfortunately, the set of spatial frequencies that can be incorporated into an illumination intensity pattern is itself limited by diffraction. The highest spatial frequency that can exist in a light-intensity distribution at an illumination wavelength (in the sample medium) of $\lambda_{ill}/n$ is $k_1 = 2n/\lambda_{ill}$, which could, for example, be produced by interference of two directly counter-propagating beams[18]. Thus, the maximum spatial frequency achievable with linear far-field fluorescence and non-uniform illumination is $k_0 + k_1 = 2n(\lambda_{em}^{-1} + \lambda_{ill}^{-1})$; approximately twofold larger than $k_0$ if the excitation and emission wavelengths are similar (Fig. 1c).

So how do techniques such as stimulated emission depletion (STED)[21,22] and saturated structured illumination microscopy (SSIM)[23,24] achieve resolution higher than $k_0 + k_1$? The answer is that they do not work within the context of linear fluorescence, within which the $k_0 + k_1$ limit is valid. All continuum-regime techniques that reach beyond this limit involve a nonlinear response of the specimen's emission rate to one or more illumination intensities. A photoresponse that is nonlinear or multilinear, combined with spatially non-uniform illumination, is the fundamental physical requirement for continuum-regime resolution beyond $2n(\lambda_{em}^{-1} + \lambda_{ill}^{-1})$.

A nonlinear photoresponse leads to higher resolution by allowing the 'effective excitation pattern' (the emission rate per fluorophore) to involve harmonics of the spatial frequencies present in the illumination intensity pattern[23–25]. Such harmonics can have higher spatial frequencies than exist in any physical light-intensity distribution, and can therefore bring correspondingly higher resolution information into the detection passband.

Consider the simplest case, in which the emission rate $R(x)$ per fluorophore is proportional to some nonlinear function $f(I)$ of a single illumination intensity $I$, where $f(I)$ can be described by a Taylor series $f(I) = a_1 I + a_2 I^2 + \ldots$, and the illumination pattern is sinusoidal at the highest possible spatial frequency $I(x) = (1+\sin(2\pi k_1 x))$. The emitting object for a specimen with fluorophore density $S(x)$ will therefore be $E(x) = S(x)R(x) = S(x)f(I(x)) = S(x)[a_1(1+\sin(2\pi k_1 x)) + a_2(1+\sin(2\pi k_1 x))^2 + \ldots]$. The $m$th term in the series is proportional to $(1+\sin(2\pi k_1 x))^m$ which, if expanded, has a leading term in the form of $\sin(2\pi(mk_1)x)$, with spatial frequency $mk_1$. Exactly as in the linear case, the real-space product corresponds to a frequency-space convolution, but one that now has $m$-times larger reach to bring high-resolution information into the detection passband. Thus, a nonlinear function of $m$th degree replaces the $k_0 + k_1$ resolution limit by $k_0 + mk_1$ (Fig. 1d). A non-polynomial nonlinearity has an infinite number of Taylor series terms and thus permits theoretically unlimited resolution. The strength of the harmonics declines rapidly with order above some threshold, leaving the practical resolution finite due to signal-to-noise concerns. However, this 'soft' limitation is qualitatively different from the mathematically rigid limits that affect linear methods.

Most typical phenomena of nonlinear optics, such as multiphoton absorption[26], have low polynomial degree and thus their potential for resolution enhancement is limited. By contrast, the general category of microscopy methods known as reversible saturable optical fluorescence transitions (RESOLFT)[27] exploits the exponential (and thus non-polynomial) functional form $a = a_0 exp(-d/d_0)$ that results when a photo-driven transition a→b with transition threshold $d_0$ is driven with a dose $d$. Several techniques in this category have been demonstrated in practice, such as STED microscopy, which uses saturation of the stimulated emission transition from the excited to the ground state[28], and saturated structured illumination microscopy (SSIM)[23,24], which exploits saturation of the transition from the ground to the excited state while using periodic illumination patterns rather that point scanning.

For continued innovation, however, it is important to understand that the set of possible nonlinearities is much larger than the RESOLFT category alone. For example, one could also imagine an engineered label comprising $m$ interacting elements having a purely $m$th order nonlinearity. Labels that are highly isolated from the surrounding medium may even allow coherent quantum effects, such as Rabi oscillations, to be exploited.

It has been argued that current super-resolution methods should be viewed in a unified way as applications of a single idea; the switching of molecules between an on and off state[29]. We have outlined here an alternative viewpoint that differs from this perspective in two ways. First, the single-molecule localization methods have a long and separate history. Although the enabling event for the modern activation-based localization methods did involve switching, these techniques represent an independent breakthrough of great impact that is not intellectually descendant from any continuum-regime concept. Second, whereas the subclass of nonlinearities that exploit on/off switching contains the currently most promising routes to super-resolution in the continuous regime, it is important to understand that a nonlinear photoresponse is the fundamental physical requirement and that the switching subclass does not encompass the entire field of possible nonlinearities. ❐

*Rainer Heintzmann is at the Randall Division of Cell and Molecular Biophysics, King's College London, London SE1 1UL, UK, and Mats G. L. Gustafsson is at the Howard Hughes Medical Institute's Janelia Farm Research Campus, Ashburn, VA 20147, USA.*
*e-mail: rainer.heintzmann@kcl.ac.uk; gustafssonm@janelia.hhmi.org*

## References

1. Abbe, E. *Arch. Mikrosk. Anat.* **9,** 413–468 (1873).
2. Francon, M. *Einfuehrung in die neueren Methoden der Lichtmikroskopie* (Wissenschaftliche Bücherei, Verlag G. Braun, Karlsruhe, 1967).
3. Burns, D. H., Callis, J. B., Christian, G. D. & Davidson, E. R. *Appl. Opt.* **24,** 154–161 (1985).
4. Bornfleth, H., Saetzler, K., Eils, R. & Cremer, C. *J. Microc.* **189,** 118–136 (1998).
5. Lacoste, T. D. *et al. Proc. Natl Acad. Sci. USA* **97,** 9461–9466 (2000).
6. Heilemann, M. *et al. Anal. Chem.* **74,** 3511–3517 (2002).
7. Gordon, M. P., Ha, T. & Selvin, P. R. *Proc. Natl Acad. Sci. USA* **101,** 6462–6465 (2004).
8. Lidke, K. A., Rieger, B., Jovin, T. M. & Heintzmann, R. *Opt. Exp.* **13,** 7052–7062 (2005).
9. Betzig, E. *et al. Science* **313,** 1642–1645 (2006).
10. Rust, M. J., Bates, M. & Zhuang, X. *Nature Meth.* **3,** 793–796 (2006).
11. Hess, S. T., Girirajan, T. P. K. & Mason, M. D. *Biophys. J.* **91,** 4258–4272 (2006).
12. Zhuang, X. *Nature Photon.* **3,** 365–367 (2009).
13. Shroff, H., Galbraith, C. G., Galbraith, J. A. & Betzig, E. *Nature Meth.* **5,** 417–423 (2008).
14. Goodman, J. *Introduction to Fourier Optics.* (Roberts, Woodbury, 2007).
15. Heintzmann, R. & Cremer, C. *Proc. SPIE* **3568,** 185–196 (1999).
16. Gustafsson, M. G. L. *J. Microsc.* **198,** 82–87 (2000).
17. M. Minsky. Microscopy Apparatus. US patent 3,013,467 (1961).
18. Gustafsson, M. G. L., Agard, D. A. & Sedat, J. W. *J. Microsc.* **195,** 10–16 (1999).
19. Shao, L. *et al. Biophys. J.* **94,** 4971–4983 (2008).
20. Petráň, M., Hadravský, M., Egger, M. D. & Galambos, R. J. *Opt. Soc. Am.* **58,** 661–664 (1968).
21. Hell, S. W. & Wichmann, J. *Opt. Lett.* **19,** 780–782 (1994).
22. Baer, S. C. Method and apparatus for improving resolution in scanned optical system. US patent 5,866,911 (1994).
23. Heintzmann, R., Jovin, T. M. & Cremer, C. *J. Opt. Soc. Am. A* **19,** 1599–1609 (2002).
24. Gustafsson, M. G. L. *Proc. Natl Acad. Sci. USA* **102,** 13081–13086 (2005).
25. Bouwhuis, G. & Spruit, J. H. M. *Appl. Opt.* **29,** 3766–3768 (1990).
26. Denk, W. *Proc. Natl Acad. Sci. USA* **91,** 6629–6633 (1994).
27. Hell, S. W. *et al.* in *The Handbook of Biological Confocal Microscopy* 3rd edn, (ed. Pawley, J.B.), (Springer, 2006).
28. Schmidt, R. *et al. Nano Lett.* doi:10.1021/nl901398t (2009).
29. Hell, S. W. *Nature Meth.* **6,** 24–32 (2009).
30. Kner, P. *et al. Nature Meth.* **6,** 339–342 (2009).
31. Gustafsson, M. G. L. *et al. Biophys. J.* **94,** 4957–4970 (2008).

# Nano-imaging with STORM

Xiaowei Zhuang

Multicolour, three-dimensional stochastic optical reconstruction microscopy now makes it possible to image cellular structures with near molecular-scale resolution.

When combined with a large repertoire of fluorescent probes and biochemically specific labelling techniques, multicolour fluorescence microscopy allows the direct visualization of molecular interactions and processes in living organisms. The diffraction-limited resolution of fluorescence microscopy, however, leaves many biological structures too small to be observed in detail. Recent years have seen the development of super-resolution imaging approaches that break the diffraction limit. These methods can be divided into two categories: (1) methods that use spatially patterned illumination to sharpen the point-spread function of the microscope, such as stimulated emission depletion (STED) microscopy (see also the Progress article on page 381 of this issue[1]) or saturated structured-illumination microscopy (SSIM) (see also the Commentary on page 362 of this issue[2]), and (2) a method based on the high-precision localization of individual fluorescent molecules, which has been referred to as stochastic optical reconstruction microscopy (STORM)[3] or (fluorescence) photoactivation localization microscopy ((F)PALM)[4,5]. Here I focus on this latter approach.

STORM, PALM and FPALM rely on the detection[6] and localization[7–9] of single fluorescent molecules. Although the image of a single fluorescent emitter has a finite size due to diffraction (roughly 200–300 nm in a lateral direction and 500–800 nm along the axial direction), the position of the emitter can be determined to a much higher precision depending on the number of photons detected[8]. This can be accomplished simply by fitting the image to find its centroid position. Fitting an image consisting of $N$ photons can be viewed as $N$ measurements of the fluorophore position, each with an uncertainty determined by the width of the image. The final precision thus equals the width of the image divided by $\sqrt{N}$. For example, the position of a single-dye molecule can be determined to accuracy as high as ~1 nm (ref. 9). This high-precision localization, however, does not directly translate into sub-diffraction image resolution, as the position of nearby emitters with overlapping images would still be difficult to determine.

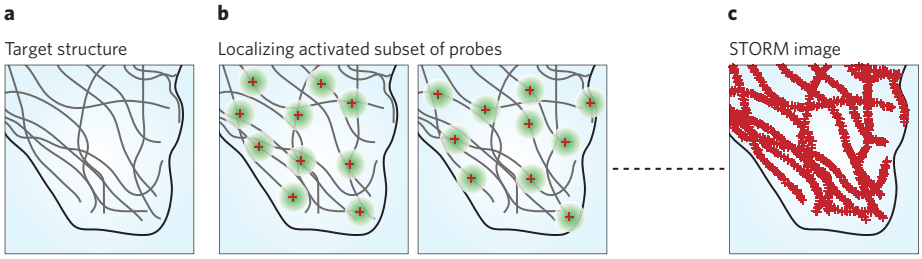


**Figure 1 |** The principle of STORM. **a**,**b**, For a densely labelled cellular structure (**a**), only a sparse set of fluorescent labels is activated at any given time such that their images (green circles, **b**) do not overlap. The snapshots, at two different times, show the activated fluorophore positions (red crosses). **c**, After enough fluorophores have been localized, a high-resolution image is constructed by plotting the measured positions. Modified with permission from ref. 30. © 2009 Annual Reviews.

A super-resolution imaging method based on the sequential localization of photo-switchable fluorescent probes has recently been invented[3–5]. These photo-switchable probes can be optically switched between a fluorescent and a dark state. Their fluorescence emission can thus be controlled over time, such that different molecules are turned on during different time windows. This additional control in the time domain allows molecules with spatially overlapping images to be separated in time, and consequently allows their positions to be precisely determined. Specifically, in the imaging process, only a subset of probes is activated to the fluorescent state at any given time (for example by exposure to light of a certain wavelength and intensity) such that the images of individual molecules do not typically overlap. By fitting these isolated images, the positions of the activated molecules can be localized with high precision. This process is then repeated to allow more molecules to be localized. Once enough localizations have been accumulated, a high-resolution image can then be constructed from the measured positions of the probes (see Fig. 1). The resolution of the final image is no longer limited by diffraction, but by the precision of each localization. This method has been variously named STORM[3], PALM[4] or FPALM[5]. For simplicity, I will use the term STORM to refer to this category of method for the remainder of the article.

STORM can be realized using a variety of photo-switchable probes, including dyes and fluorescent proteins. In its simplest form, STORM can be achieved using a simple fluorescent dye and a single-colour continuously illuminating laser. Figure 2a shows such an example, in which the microtubules in a cell are immuno-stained with Alexa Fluor 647 and imaged with a red laser (657 nm). The red laser accomplishes all three tasks required for STORM: exciting fluorescence from Alexa Fluor 647, deactivating it to the dark state and reactivating it to the fluorescent state. At equilibrium, the fluorophore spends about 0.1% of its time in the fluorescent state, allowing around 6,000 photons to be detected per switching cycle. The combination of high photon flux and low activation equilibrium affords a high image resolution. Indeed, the STORM image shows a marked improvement in resolution over the corresponding conventional fluorescence image, as can be seen in Fig. 2b,c. In the regions where microtubules are densely packed and unresolved in the conventional image, individual microtubule filaments are clearly resolved by STORM. Alexa Fluor 647 is a member of a family of photo-switchable cyanine dyes that can be reversibly cycled between a fluorescent and a dark state by exposure to light[10–12]. This family includes other red cyanine dyes suitable for STORM, such as Cy5, Cy5.5 and Cy7 (refs 3, 12, 13). STORM has also been implemented using other switchable dyes,

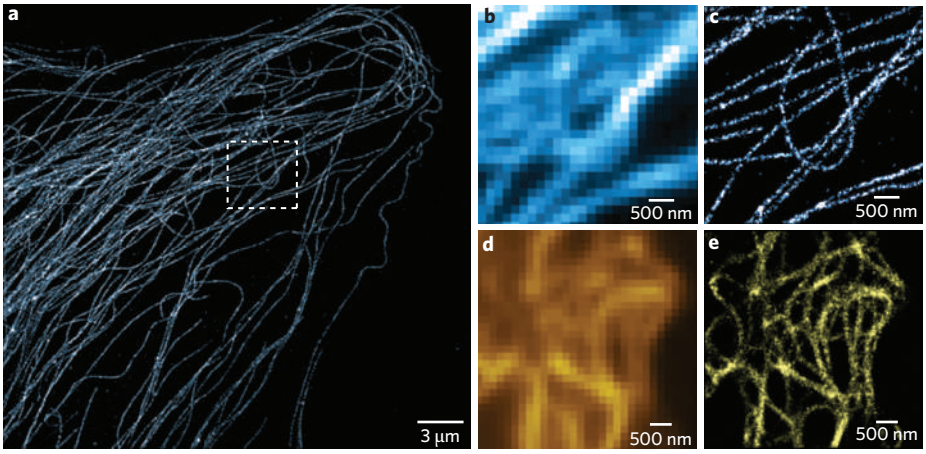


**Figure 2 |** STORM imaging of cells with photo-switchable dyes and fluorescent proteins. **a**, STORM image of microtubules in a BS-C-1 cell. The microtubules are immunostained with antibodies that are labelled with photo-switchable Alexa Fluor 647. **b**,**c**, Conventional (**b**) and STORM (**c**) images correspond to the boxed region in **a**. **d**,**e**, Conventional (**d**) and STORM (**e**) images of vimentin in a BS-C-1 cell. The vimentin filaments are labelled with a photo-switchable fluorescent protein, mEos2. A moderate aggregation of the vimentin filaments is observed, potentially caused by the fluorescent protein tags.

such as photochromic rhodamine[14], caged dyes[4] and blinking dyes[15,16].

In additional to dyes, photo-switchable fluorescent proteins can also be used for STORM imaging. Figure 2d and e shows the comparison of conventional and STORM images of mEos2-labelled vimentin in a cell, again showing substantial resolution improvement by STORM. mEos2 is a monomeric variant of the Eos fluorescent protein that can be photoactivated from a green-emitting form into a red-emitting form[17,18]. The STORM image was taken by activating mEos2 with a 405-nm laser and imaging the activated mEos2 with a 568-nm laser. Other photo-switchable fluorescent proteins, such as PA-GFP, Kaede, tdEos, KikGR, Dronpa, rsFastLime, bsDronpa, psCFP2, Dendra2, EYFP and PAmCherry, have also been demonstrated for super-resolution imaging[4,5,19–23].

One of the main advantages of fluorescence microscopy is its capacity for multicolour imaging. Co-localization analysis with multicolour imaging has been widely used to map interactions between different biological structures, but the accuracy of co-localization is inherently limited by the image resolution. Taking advantage of its high resolution, STORM provides a more precise picture of molecular interactions. Various combinations of the aforementioned photo-switchable dyes and fluorescent proteins have been used for multicolour super-resolution imaging[12,20,21,23–25]. For example, the distinct emission spectra of Cy5, Cy5.5 and Cy7 allow multicolour imaging by distinguishing their emission colours. Another interesting property of these cyanine dyes is the adjustable nature of their activation wavelength. The wavelength of light that efficiently activates these dyes can be adjusted almost at will by pairing them with an 'activator' dye. For example, when the photo-switchable 'reporter' Cy5 is paired with Cy3, Cy2 and Alexa Fluor 405, it can be selectively activated by a green, a blue and a violet laser, respectively[12]. This colour-specific activation allows a second approach for multicolour STORM: distinct probes can be differentiated by the colour of their activation light. Combinatorial pairing reporters and activators could offer even more colours. Figure 3 shows two-colour STORM images of microtubules and clathrin-coated pits, an important endocytic machinery in cells[12]. The false co-localization between clathrin-coated pits and microtubules shown in the conventional image (Fig. 3a) is now clearly resolved in the STORM image (Fig. 3b and c).

Most cellular structures have a three-dimensional (3D) architecture, and resolving these structures requires high resolution in all three dimensions. This can be accomplished by high-precision 3D localization of fluorophores. The lateral position of a molecule can be determined from the centroid of its image, and the shape of the image contains information about the axial ($z$) position of the molecule. High localization precision along the $z$ axis can be achieved by a variety of approaches. The astigmatism approach was first used to achieve 3D STORM[26]. In this approach, a cylindrical lens is introduced into the imaging path to create a different focus in the lateral ($x$ and $y$) directions, such that the image of a molecule appears elliptical. The ellipticity of the image varies with the $z$ position of the molecule, and thus can be used to derive the value of $z$ with high precision. Using this approach, we have resolved cellular structures with lateral and axial resolutions of 20 nm and 50 nm (full width at half maximum, FWHM), respectively[26]. Both the standard deviation (SD) and FWHM have been used to describe resolution in the literature. Here we define resolution in FWHM (equal to 2.2 SD for a Gaussian distribution), as it provides a better measure of the closest distance between two objects that can be resolved.

The high resolution allows STORM to resolve the 3D morphology of nanoscopic structures in cells. Figure 4 shows the example of clathrin-coated pits, which typically have a diameter of 100–200 nm (ref. 26). In a conventional image, clathrin-

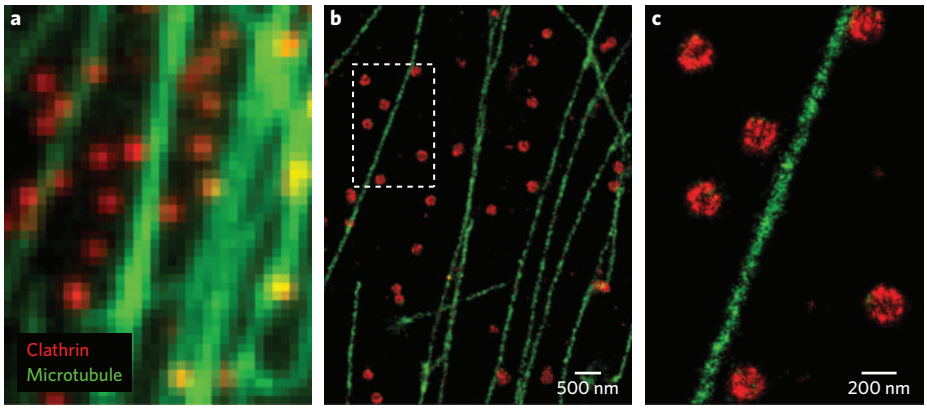


**Figure 3 |** Multicolour STORM. The microtubules and clathrin-coated pits in a BS-C-1 cell are immunostained with Cy2-Alexa 647-labelled and Cy3-Alexa 647-labelled antibodies, respectively. **a**, Conventional fluorescence image. **b**, STORM image of the same area. **c**, Magnified view of the boxed region in **b**. Parts **b** and **c** adapted with permission from ref. 12. © 2007 AAAS.

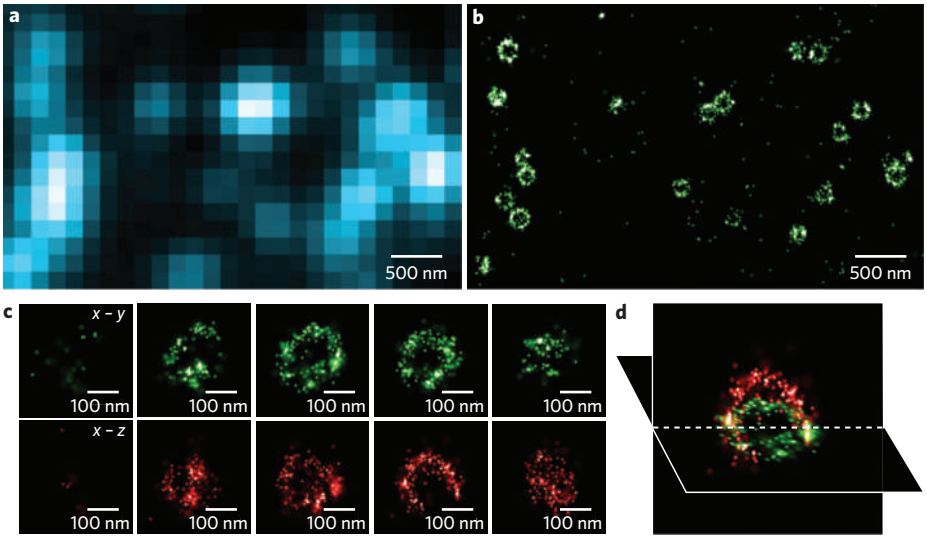


**Figure 4 |** Three-dimensional STORM. **a**, Conventional image of clathrin-coated pits in a BS-C-1 cell. Clathrin is immuno-stained with Cy3-Alexa 647-labelled antibodies. **b**, *x*–*y* cross-section of the corresponding 3D STORM image. **c**, Serial *x*–*y* and *x*–*z* cross-sections of a coated pit. **d**, An *x*–*y* and *x*–*z* cross section presented in 3D perspective. Parts **a**–**d** from ref. 26. © 2008 AAAS.

coated pits appear as diffraction-limited spots with no discernable structure (Fig. 4a). In stark contrast, the 3D STORM clearly resolves the half-spherical shell morphology of coated pits (Fig. 4b–d). STORM allows a sample several hundred nanometres in thickness to be imaged in 3D without any scanning. But as the sample gets thicker, the image of a molecule becomes more blurred, ultimately limiting the localization precision. A coarse stepping of the sample stage can be combined with high-precision 3D location for imaging thicker samples, such as a mitochondria network in an entire cell[25]. Several other approaches have also been used for 3D STORM, such as defocusing light[27], using a double-helical point-spread function[28] or using interferometry[29]. A *z* resolution as high as 10–20 nm has been reported for the latter approach[29].

Although impressive, the resolutions mentioned above do not represent the ultimate limit of STORM. Its spatial resolution is determined by the precision and density of localizations in the image. These two quantities are in turn determined by several practical factors: (i) the brightness of the probe, (ii) the residual dark-state fluorescence, (iii) the spontaneous activation rate from the dark to the fluorescent state, (iv) the labelling efficiency and (v) the label size[30]. Given sufficient probe brightness and labelling density, resolution can be almost arbitrarily high. For a bright probe, such as Alexa Fluor 647, the number of photons detected allows in principle a localization precision of a few nanometres, promising true molecular-scale resolution. At this level, the physical size of the label becomes an important factor. Ideally, one would like to couple a small and bright fluorophore directly to the molecule of interest. Several recently developed approaches allow specific attachment of small organic fluorophores to cellular proteins through genetic encoding approaches[31], providing a labelling strategy that could potentially support molecular-scale resolution.

Another important aspect of imaging is the data acquisition speed. Because of the intrinsic trade-off between time and spatial resolutions, super-resolution imaging is relatively slow. Specifically, a STORM image is constructed from localizations accumulated in a wide field over many imaging frames. The imaging speed is thus limited by the number of frames required to construct a high-resolution image. This speed-limiting mechanism is in contrast to that of STED, in which the scanning of the small focal point across the sample limits the imaging speed. Thus STORM is expected to be faster than STED when imaging a large sample area but slower than STED when imaging a small area[30]. Currently, a STORM image at the highest resolution typically requires minutes of acquisition time. At a spatial resolution of 60–70 nm, time-resolved images have been acquired with a temporal resolution of a few tens of seconds in living cells[32]. We expect the imaging speed to improve further with faster cameras, higher excitation power and probes with faster switching rates.

In summary, the STORM/PALM/FPALM approach provides a new platform for high-resolution imaging and shows great promise in the study of cellular processes at the molecular scale. Future development of the imaging technology itself, as well as new fluorescent probes and labelling methods, will continue to improve the power and versatility of this imaging approach. We can expect broad applications of super-resolution imaging in many areas of life science. ❐

*Xiaowei Zhuang is at the Department of Chemistry and Chemical Biology, and the Department of Physics, Howard Hughes Medical Institute, Harvard University, Cambridge, Massachusetts 02138, USA.*
*e-mail: zhuang@chemistry.harvard.edu*

## References

1. Hell, S. W., Schmidt, R. & Egner, A. *Nature Photon.* **3,** 381–387 (2009).
2. Heintzmann, R. & Gustafsson, M. G. L. *Nature Photon.* **3,** 362–364 (2009).
3. Rust, M. J, Bates, M. & Zhuang, X. *Nature Meth.* **3,** 793–795 (2006).
4. Betzig, E. *et al. Science* **313,** 1642–1645 (2006).
5. Hess, S. T., Girirajan, T. P. K. & Mason, M. D. *Biophys. J.* **91,** 4258–4272 (2006).
6. Moerner, W. E. & Orrit, M. *Science* **283,** 1670–1676 (1999).
7. Gelles, J., Schnapp, B. J. & Sheetz, M. P. *Nature* **331,** 450–453 (1988).
8. Thompson, R. E., Larson, D. R. & Webb, W. W. *Biophys. J.* **82,** 2775–2783 (2002).
9. Yildiz, A. *et al. Science* **300,** 2061–2065 (2003).
10. Bates, M., Blosser, T. R. & Zhuang, X. *Phys. Rev. Lett.* **94,** 108101 (2005).
11. Heilemann, M., Margeat, M., Kasper, R., Sauer, M. & Tinnefeld, P. *J. Am. Chem. Soc.* **127,** 3801–3806 (2005).
12. Bates, M., Huang, B., Dempsey, G. T. & Zhuang, X. *Science* **317**, 1749–1753 (2007).
13. Heilemann. M. *et al. Angew. Chem. Int. Ed.* **47,** 6172–6176 (2008).
14. Folling, J. *et al. Angew. Chem. Int. Ed.* **46,** 6266–6270 (2007).
15. Fölling, J. *et al. Nature Meth.* **5,** 943–945 (2008).
16. Steinhauer, C., Forthmann, C., Vogelsang, J. & Tinnefeld, P. *J. Am. Chem. Soc.* **130,** 16840–16841 (2008).
17. McKinney, S. A., Murphy, C. S., Hazelwood, K. L., Davidson, M. W. & Looger, L. L. *Nature Meth.* **6,** 131–133 (2008).
18. Wiedenmann, J. *et al. Proc. Natl Acad. Sci. USA* **101,** 15905–15910 (2004).
19. Egner, A. *et al. Biophys. J.* **93,** 3285–3290 (2007).
20. Shroff, H. *et al. Proc. Natl Acad. Sci. USA* **104,** 20308–20313 (2007).
21. Andresen, M. *et al. Nature Biotechnol.* **26,** 1035–1040 (2008).
22. Biteen, J. S. *et al. Nature Meth.* **5,** 947–949 (2008).
23. Subach, F. V. *et al. Nature Meth.* **6,** 153–159 (2009).
24. Bock, H. *et al. Appl. Phys. B* **88,** 161–165 (2007).
25. Huang, B., Jones, S. A., Brandenburg, B. & Zhuang, X. *Nature Meth.* **5,** 1047–1052 (2008).
26. Huang, B., Wang, W., Bates, M. & Zhuang, X. *Science* **319,** 810–813 (2008).
27. Juette, M. F. *et al. Nature Meth.* **5,** 527–529 (2008).
28. Pavania, S. R. P. *et al. Proc. Natl Acad. Sci. USA* **206,** 2995–2999 (2009).
29. Shtengel, G. *et al. Proc. Natl Acad. Sci. USA* **106,** 3125–3130 (2009).
30. Huang, B., Bates, M. & Zhuang, X. *Annu. Rev. Biochem.* **78,** 993–1016 (2009).
31. Fernandez-Suarez, M. & Ting, A. Y. *Nature Rev. Mol. Cell. Biol.* **9,** 929–943 (2008).
32. Shroff, H., Galbraith, C. G., Galbraith, J. A. & Betzig, E. *Nature Meth.* **5,** 417–423 (2008).

## Acknowledgements

This work is supported in part by the National Institutes of Health and Howard Hughes Medical Institute. I thank B. Huang and G. Dempsey for taking the images shown in Fig. 2.

# Eyes on super-resolution

Advanced imaging techniques have evolved to see beyond the diffraction limit. W. E. Moerner spoke to *Nature Photonics* about the techniques involved.

**What is super-resolution imaging?**

Super-resolution in microscopy occurs when it becomes possible to exceed the standard diffraction limit. This is given by the Abbe diffraction criterion of $\lambda/(2NA)$, where $\lambda$ is the wavelength of light and NA is the numerical aperture of the lens. In other words, the diffraction limit normally means that points in the image spaced by less than this amount cannot be distinguished. Super-resolution, therefore, refers to the distinguishing of points spaced by less than $\lambda/(2NA)$. For visible light, the diffraction limit is roughly 200 nm.

**What are the current techniques for achieving super-resolution in the near field?**

For near-field optics, super-resolution has been achieved by confining the electric field of light (for example, by using a tapered optical fibre coated with a metal or by scanning with a sharp metal tip close to the sample of interest). More generally, a variety of metallic plasmonic nano-antennas have the ability to concentrate light into a volume much smaller than that derived from the diffraction limit. If these nano-antennas are brought close to a sample of interest (say within about 10 nm), the localized optical field can probe the sample, producing an optical signal. The signal can be fluorescence, Raman scattering or another type of optical signal.

**How about in the far field?**

There are several methods of achieving super-resolution in the far-field, and these can be classified into two groups. The first group relies on optical patterning of the excitation and a nonlinear response of the material that directly reduces the size of the point-spread function of the microscope. Early examples of this method include the pioneering 4π microscopy and the stimulated emission depletion (STED) microscopy of Stefan Hell. The latter relies on a method of depleting the emission of molecules in a ring around the focal spot. Ways of achieving this include stimulated emission, triplet-state shelving and *cis–trans* isomerization, and more generally reversible saturable optical fluorescence transitions (RESOLFT). More recent examples include nonlinear structured-illumination microscopy (SIM) and isoSTED.

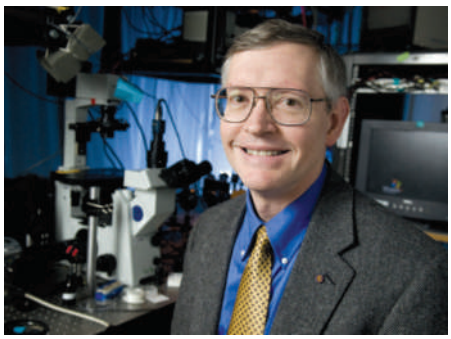

L. A. CICERO / STANFORD NEWS SERVICE

W. E. Moerner is a professor at Stanford University in the USA.

The second group includes methods based on single-molecule imaging and superlocalization combined with active control of the concentration of emitting molecules by either photoactivation or photoswitching. This includes photoactivation localization microscopy (PALM), stochastic optical reconstruction microscopy (STORM), fluorescence photoactivation localization microscopy (F-PALM), point accumulation for imaging in nanoscale topography (PAINT), ground-state depletion microscopy followed by individual molecule return (GSDIM), and several other related acronyms. I prefer to call these methods by the general term 'single-molecule active control microscopy', or SMACM. All of these techniques require the ability to image single molecules and analyse the resulting point-spread function to extract the position of the molecule with a spatial precision that is better than the diffraction limit. To keep single emitters from overlapping, only a sparse subset are allowed to emit at any one time, which is the 'active control' requirement achieved by photoactivation, photoswitching, shelving in dark states, dequenching and other methods. Labels of the emitter position in the subset are derived before a new subset is created and the process is repeated. The final image is a superposition of the locations of all the identified single molecules. Fundamentally, the molecule positions must be closer than the diffraction limit to qualify for super-resolution. Some new three-dimensional versions of these methods can now be found, based on astigmatism (Huang), dual-plane imaging (Ober) and interferometric PALM (i-PALM), as well as the double-helix point-spread function method (DH-PALM) that we reported.

**How are such imaging techniques being used?**

Near-field methods can be used to image nanoscale features on a surface; for instance, on a cell membrane or an integrated circuit chip. Far-field methods have been used for imaging many nanoscale objects, such as organelles in cells, protein superstructures in bacteria, or the three-dimensional positions of single molecules in polymers. Essentially any structure that can be labelled can, in principle, be imaged. Leica Microsystems now sells an STED microscope with a resolution of 80 nm. At present, the far-field methods are those chosen for imaging structures below a surface, such as inside a cell. Although a commercial STED microscope is now available, the SMACM schemes have been implemented in many laboratories due to the simplicity of the concept. The near-field methods do not require fluorescence, so they are more promising for imaging non-emissive materials.

**What resolutions have been achieved?**

For near-field methods, resolutions in the range of a few nanometres to 15 nm have been achieved depending on tip sharpness and the confining field strength. The far-field SMACM methods routinely achieve a resolution of approximately 20–30 nm, with special cases achieving resolutions as precise as 1 nm. The STED resolution varies over a large range, from a commercial resolution of around 80 nm to an experimentally achieved resolution of around 20 nm. Recently, Stefan Hell reported resolutions down to several nanometres when imaging the nitrogen-vacancy centres of diamond.

**What are the limitations of these super-resolution techniques?**

This is a complex issue. My general point of view is that all these methods

are complementary, each with its own advantages and disadvantages. I will try to outline some of the key points here. Near-field imaging techniques place very few requirements on the optical properties of the object, but are restricted to surfaces with small areas in the region within ~10 nm of the tip or nano-antenna. Moreover, precise positioning of the tip or nano-antenna is imperative. For far-field imaging techniques, the advantages of STED/RESOLFT are that they provide high-speed, video-standard imaging (demonstrated recently) and that they are direct methods that can reduce the point-spread function in one step. However, they require fluorophores that can be cycled between bright and dark states many times without photobleaching. Furthermore, they involve a complex optical design enabling two spots to be overlapped properly in space and time. SMACM approaches, on the other hand, have a simple wide-field optical set-up with no tightly focused spots. Each emitter needs to be used only once in principle, but detecting more photons gives better localization precision. Nevertheless, they need photoactivatable/photoswitchable fluorophores or accessible bright/dark states. Single-molecule imaging sensitivity is also required, as is the time for repeated activation/imaging cycles; thus, a quasi-static structure is needed to generate the image.

**How can such techniques be improved further?**

In the SMACM methods, imaging speed can be increased by using higher laser power. In all far-field methods, the process of super-resolution relies on the photophysical properties of the emitter, such as energy levels, state transition probabilities and photostability. This means that with the design and synthesis of new emitters or mutational generation of new photoswitchable fluorescent proteins, the optical properties (and therefore the super-resolution) imaging can be improved. In the case of STED/RESOLFT, simple, reliable methods for optical alignment of complex components would be helpful. The commercial design solves this problem with an automatic push-button alignment capability. Ultimately, the challenge is that a long-term investment in fluorogen development is required for the design and optimization of photoswitchable/photoactivatable emitters, or emitters to survive many cycles into and out of dark states.

**What is the future outlook for the field?**

The outlook is truly exciting. As more and more molecules and methods for super-resolution imaging are developed, the power of optical microscopy to observe complex nanoscale systems non-invasively will increase. I find it particularly exciting that the ability of single molecules to act as nanoscale light sources inside materials is now being used to achieve super-resolution imaging. In most cases, these methods do not require complex sectioning or freezing (as electron or X-ray methods do), so the actual structures in living systems, and structures that undergo time-dependent changes, can be observed. The gap between X-ray/electron microscopy and optical microscopy is narrowing rapidly.

INTERVIEW BY RACHEL WON

DATA STORAGE

## A new dimension

*Nature* **459,** 410–413 (2009)

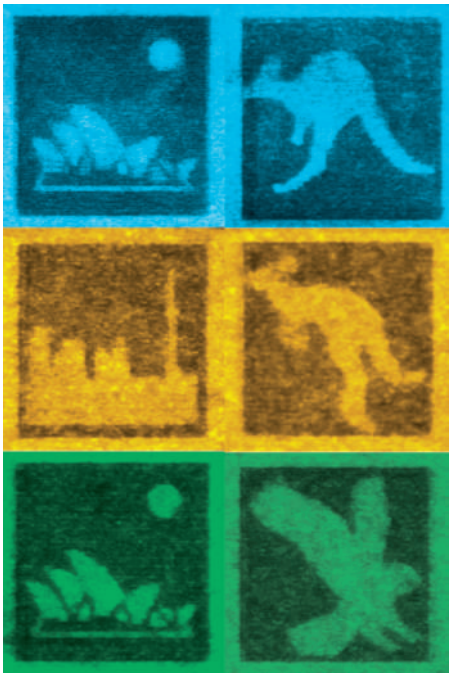



Optical data storage has entered a new dimension. Or two, to be precise. Scientists have devised a five-dimensional optical recording technique that could increase the storage capacity of disks by several orders of magnitude.

The name of the game is multiplexing, a technique that makes it possible to increase the density of information that can be stored in a given recording volume. Today's CDs and DVDs store information in just two or three spatial dimensions and the best double-sided double-layer DVDs can hold around 17 GB. Multiplexing uses one or more extra dimension to store multiple individually addressable patterns within the same volume. Peter Zijlstra and co-workers use wavelength and the polarization of light as the extra two dimensions.

Key to their breakthrough is the choice of a suitable recording medium. It turns out that gold nanorods immersed in a polymer layer are perfect: they exhibit a surface plasmon resonance that is extremely sensitive to wavelength and polarization, and they undergo photothermal reshaping mediated by this resonance, which provides axial selectivity. In tests using three layers of nanorods, Zijlstra *et al.* extrapolate to a capacity of 1.6 TB in a DVD-sized area. With more nanorod layers, this could be boosted to around 10 TB.

METAMATERIALS

## Roll up, roll up

*Phys. Rev. Lett.* **102,** 163903 (2009)

You may have heard of self-assembly, but have you heard of 'self-rolling'? Physicists in Germany have proposed a new type of metamaterial that consists of semiconductor and metal layers that roll up into dimensions small enough that it can operate at visible wavelengths. The holy grail of metamaterials research is to create a structure that can be used for superlensing or cloaking in the visible. For this to work, the metamaterial's constituent building blocks must be around 100 nm or smaller in size. Conventional techniques — direct laser writing and atomic layer deposition, for instance — can create nanometre-scale features, but usually not with three-dimensional curvature. This is where the self-rolling comes in.

Schwaiger *et al.* have designed a metamaterial made of alternating layers of strained indium gallium arsenide, gallium arsenide and silver, all grown on a flat substrate. When released from the substrate by selective etching, the layers roll up into a microtube in order to minimize their strain energy. The walls of the tubes form a superlattice; by tuning the thickness of each layer, one can tune the material's plasma frequency over a broad range in the visible and near-infrared and in theory create a hyperlens that magnifies visible light.

OPTOMECHANICAL SYSTEMS

## Light matters

*Phys. Rev. A* **79,** 053810 (2009)

Matter affects light and light affects matter. Experimentalists often rely on optical fields to trap and cool atoms. They also use light to manipulate macroscopic objects such as micromechanical mirrors. Until now, the models used to describe the way light interacts with microscopic objects such as atoms and macroscopic objects such as mirrors have been completely different. In their latest publication, André Xuereb and colleagues present a new scattering theory for optomechanical systems that is able to describe the behaviour of both scenarios using a single, unified framework.

Atoms are assumed to be very weakly scattering objects that essentially do not affect incoming light beams. Massive moving mirrors, on the other hand, are taken to strongly influence the radiation field. Xuereb *et al.* elegantly marry the two extremes by generalizing the so-called transfer matrix method, a technique that is used to solve problems in statistical mechanics and that relates forward- and backward-travelling waves on either side of an optical element. The model includes quantum fluctuations related to the quantized nature of an electromagnetic field, and can predict the motion of arbitrary combinations of atoms and mirrors that interact via an optical field. The authors say their model can easily be extended to more complex systems.

OPTICAL SWITCHING

## Core confinement

*Phys. Rev. Lett.* **102,** 203902 (2009)

All-optical switching allows one light beam to control the propagation of another, typically via nonlinear interactions with atoms. Unfortunately, the efficiency of the switching is often hampered by the fact that

SINGLE-PHOTON SOURCES

## Diamond's hidden secrets

*Appl. Phys. Lett.* **94,** 203107 (2009)

Diamonds are not just a girl's best friend. Researchers in Australia are looking to diamond to create room-temperature single-photon sources that can be used for ultrasecure quantum communication.

There are over 500 known defect centres in diamond, but to date only three have been identified as single-photon emitters. Furthermore, the emission rates of these three are limited to about 300 kHz owing to the existence of metastable states that reduce the efficiency of the system. For diamond nanotechnology to prove practical, more efficient defect centres with true two-level energy structures similar to those offered by quantum dots must be found.

Simpson *et al.* have uncovered a new defect centre that emits stable single photons at a rate of 1.6 MHz at room temperature. To create the defect centre, they applied a microwave plasma-enhanced chemical vapour deposition technique to a 1 μm × 1 μm silica substrate that had been seeded with diamond granules up to 2 μm in size. Photon statistics measurements confirm that no photon bunching occurs (in contrast to all other diamond-related defects studied so far). This new defect is the only single-photon source to exhibit stable megahertz emission at room temperature, making it an excellent contender for quantum key distribution applications.

light beams in nonlinear media interact very weakly at low light levels. Michal Bajcsy and colleagues have designed a more efficient all-optical switch that simultaneously confines cold atoms and light beams inside a hollow-core photonic crystal fibre. They show that a beam of just a few hundred photons is sufficient to control the transmission of a weak probe beam.

Waveguides such as optical fibres offer a way to increase both the interaction length of two light beams and the optical intensity involved. The challenge that researchers face is to ensure that the optical nonlinearity is sufficiently large. As optical nonlinearities are enhanced near atomic resonances, Bajcsy *et al.* have chosen to use an atomic vapour to access the optical nonlinearity that occurs in gas atoms at resonance. A laser-cooled cloud of rubidium atoms is trapped inside the hollow-core photonic crystal fibre by a dipole trapping beam. Additional probe, coupling and switch optical fields are then used to control the atomic state and induce electromagnetically induced transparency. Under these conditions, the properties of slowly propagating photons can be manipulated by tiny energies corresponding to a hundred or so photons per pulse.

DISPLAYS

## Getting flexible

*Nature Mater.* **8,** 494–499 (2009)

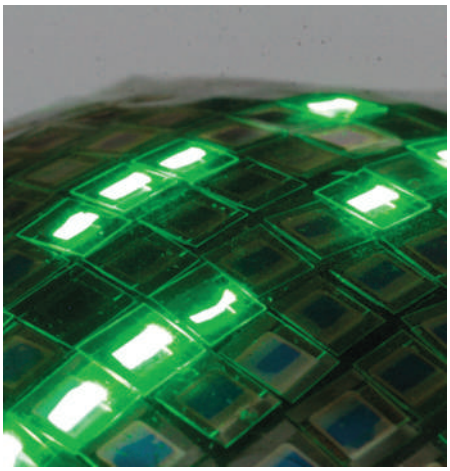



It is very clear that advances in display technology are changing our lives. The challenge now is to make optical displays that are cheap, easy to manufacture and flexible in size and shape so that they are no longer confined to two-dimensional formats. Tsuyoshi Sekitani and colleagues in Japan have fabricated a stretchable organic display that can be folded in two, crumpled up and stretched to more than twice its original size.

At the heart of the technology is an elastic conducting material that consists of single-walled nanotubes (SWNTs) uniformly dispersed throughout a fluorinated rubber matrix. An ionic liquid and jet-milling technique is used to intersperse SWNT bundles throughout the rubber such that they form robust networks with electronic conductivities of more than 100 Siemens $cm^{-1}$. The authors integrated this elastic conducting material with organic transistors and organic LEDs to produce a rubbery active-matrix organic LED display. The prototypes, which have active areas of $10 \times 10$ $cm^2$ and resolutions of 256 monochrome pixels, can be stretched over a hemisphere without suffering any damage. Crucially, the SWNT/rubber composite can be produced using widely available printing technology, which will reduce costs. Ultimately, the technology could lead to 'artificial skin' that bends to the contours of the human body and displays medical data.

NANOPHOTONICS

## Splitting water

*Nano Lett.* doi:10.1021/nl900772q (2009)

Hydrogen could be the fuel of the future. It offers one of the highest energy densities per unit mass — 140 MJ $kg^{-1}$ — and burns cleanly with oxygen to form water. But its success as an energy source depends on our ability to efficiently generate hydrogen from renewable energy sources such as solar-powered water splitting. And to achieve efficient water splitting, we need the right kind of photoelectrodes.

Xunyu Yang and colleagues at the University of California studied the effectiveness of nitrogen-doped zinc oxide nanowire arrays as anodes in photoelectrochemical (PEC) cells. Electrodes that incorporate nanorods, nanotubes or nanocrystals are of particular interest because they offer high surface areas, short diffusion lengths and low reflectivity. Yang *et al.* used a hydrothermal method to prepare dense, vertically aligned ZnO nanowires, and doped them with up to 4% nitrogen using an annealing process in ammonia (the nitrogen substitutes itself at oxygen sites). On illumination with a power density of 100 mW $cm^{-2}$, water splitting was observed with both doped and undoped nanowire anodes. However, doping yielded an order-of-magnitude increase in the photocurrent density with a photon-to-hydrogen conversion efficiency of 0.15% at an applied voltage of +0.5 V. These results suggest that nitrogen-doped ZnO nanowire arrays could be a promising design for future PEC cells.

ASTROBIOLOGY

## Signs of life

*Proc. Natl Acad. Sci. USA* **106,** 7816–7821 (2009)

NASA / ESA

It is an interesting fact that the amino acids we see in living organisms are left-handed, whereas most sugars are right-handed. The fact that biological molecules exhibit a certain handedness — homochirality — is considered a useful signature to search for extraterrestrial life. In fact, amino acids found in meteorites that have struck Earth are predominantly left-handed too. With this in mind, a team of astrobiologists has shown that circular polarization spectroscopy can remotely detect light scattered off photosynthetic microbes and is a feasible probing technique in the search for signs of extraterrestrial life.

Photosynthetic bacteria evolved early in Earth's history, between two and three billion years ago. As such, photosynthesis could well be a plausibly commonplace and statistically dominant process on extrasolar planets. William Sparks and colleagues selected two different strains of chlorophyll-based marine bacteria to test their analysis technique. The strong electronic absorption bands that are characteristic of photosynthetic molecules have different absorption coefficients for left- and right-circularly polarized light, offering researchers a way to distinguish between different chiralities. Using a polarimeter, the authors acquired both transmission and scattered light reflection polarization spectra, sucessfully detecting circular polarization in both types of microbe. The experiments confirm that the polarization properties of microorganisms can be probed from afar, but it remains to be seen whether the same biosignatures exist in more complex organisms.

PHOTOVOLTAIC TECHNOLOGY

# Relay dye boosts efficiency

Resonant energy-relay between two dye species allows photovoltaic harvesting of photons across a wider spectral range. This technique has been exploited to boost the efficiency of dye-sensitized solar cells by 26%.

Daniel J. Farrell and Nicholas J. Ekins-Daukes

At present, most commercial photovoltaic devices are made from inorganic semiconductors, such as silicon, and operate with efficiencies of around 10–20%. Any significant increases in efficiency, achieved at low cost, would clearly accelerate the acceptance of solar energy as a mainstream renewable energy source. Organic solar cells represent an important opportunity to reduce the manufacturing cost of photovoltaic panels, if their efficiency can be improved.

On page 406 of this issue, Hardin *et al.* report an increase in the range of photon energies that can be efficiently harvested by organic solar cells[1]. The key to the improvement is a relay dye that absorbs energy at green wavelengths and transfers it by Förster resonant energy transfer (FRET) to a conventional sensitizer dye that absorbs at red wavelengths. The cell shows an improvement in conversion efficiency of almost a third, compared with a cell without the relay dye.

The main difficulty in improving the efficiency of photovoltaic energy conversion is the spectral bandwidth of sunlight. In conventional inorganic solar cells, the use of suitable bandgap materials allows absorption from the near-infrared to the ultraviolet. In contrast, dye-sensitized solar cells rely on molecular transitions where panchromatic absorption is much harder to achieve.

Conventional dye-sensitized solar cells are composed of dye molecules that are anchored to a nanoporous titania film. After absorption of photons in the dye, an electron is transferred from the dye into the titania film and then to an electrical circuit, where it delivers energy to a load (Fig. 1a). The electron is subsequently returned to the ground state of the dye via a liquid electrolyte that fills the pores in the nanoporous titania film. Much effort has been devoted to developing molecular dyes capable of absorbing the visible, and some of the near-infrared, components of the solar spectrum[2,3]. With the appropriate choice of dye, wavelengths of 400–700 nm can be absorbed,

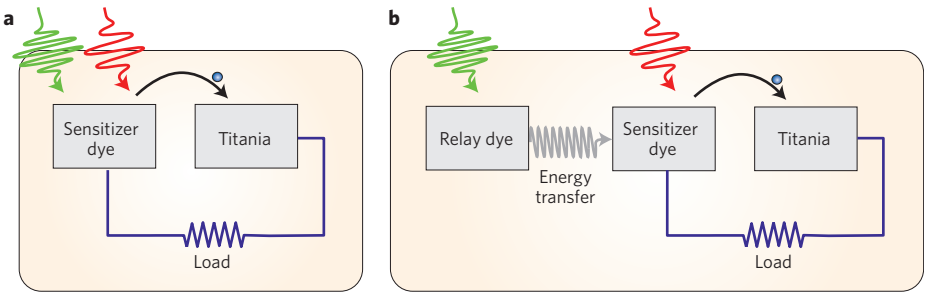


**Figure 1 |** Schematic operating principles for a conventional dye-sensitized solar cell where a single dye must absorb a broad range of wavelengths (**a**), and an energy-relay dye-assisted solar cell where the absorption of sunlight light is shared between two molecular species (**b**).

resulting in power-conversion efficiencies of up to 11.3% (ref. 4).

One way to relieve the difficulties of achieving panchromatic absorption with a single dye is co-sensitization with multiple dye species[5]. This approach, however, is limited (as with any surface) by the fact that different dye species compete for a finite number of anchor points on the titania film surface, where electrons transfer from the dye to the electrical circuit. Thus, although the spectral range for absorption can be easily increased by co-sensitization, increasing the overall efficiency is much more difficult.

Hardin *et al.* demonstrate an alternative approach to co-sensitization that extends the spectral range of absorption while preserving the overall optical density of the dye-sensitized solar cell. They achieve this by adding a second dye — the relay — which relies on FRET to transfer the excited state from the relay dye to the sensitizer dye (Fig. 1b), into the electrolyte of a dye-sensitized solar cell. The relay dye does not compete for the anchor points on the titania surface and, in addition, absorbs photons of a different wavelength.

Hardin *et al.* fabricated cells using a phthalocyanine sensitizer, chloroform electrolyte solvent and a perylene-based relay dye (PTCDI). In this schema, the sensitizer dye absorbs light with a wavelength of 600–700 nm, and the relay dye in the range of 500–600 nm. Overall, a 26% increase in conversion efficiency was found for the cell containing the relay dye (compared with a control cell where no dye was present). It was shown that under appropriate conditions, FRET can become the dominant relaxation process for the relay dye, overcoming the rapid quenching that one might expect from the presence of the electrolyte.

The use of energy-relay dyes enables the broad solar spectrum to be absorbed by multiple dyes, thereby easing the design constraints for the dye. However, efficient FRET-coupling requires that the relay dye absorbs photons at a higher energy than that of the sensitizer dye. As a result, this technique can be used to improve the short-wavelength photovoltaic response of the cell, but cannot be used to extend the range into the near infrared. In principle, however, the absorption wavelength of the sensitizer dye can be moved further into the infra-red, allowing the relay dye to absorb a greater fraction of the visible spectrum.

Another constraint is that the dye must be soluble in the electrolyte, which places limitations on the electrolyte's composition. In Hardin's study, this results in an overall reduction of the solar-cell efficiency. Despite this, an increased power-conversion efficiency using the relay dye is observed when compared with a

control cell (the same electrolyte but with no relay dye present). To achieve optimum performance from high concentrations of relay dyes, the electrolyte requires some optimization.

The work of Hardin *et al.* highlights the need for a detailed understanding of the electrolyte and associated additives in both the conventional dye-sensitized solar cell and the new energy-relay approach, which itself adds the additional constraint of high dye solubility. The concept of the energy-relay dye now opens a new field for developing innovative, matched combinations of dyes that span the solar spectrum. ❐

*Daniel J. Farrell and Nicholas J. Ekins-Daukes are at the Department of Physics & The Grantham Institute for Climate Change, Imperial College London, Prince Consort Road, London, SW7 2AZ, UK.*
*e-mail: daniel.farrell@imperial.ac.uk; n.ekins-daukes@imperial.ac.uk*

## References

1. Hardin, B. E. *et al. Nature Photon.* **3,** 406–411 (2009).
2. Bessho, T. *et al. J. Am. Chem. Soc.* **131,** 5930–5934 (2009).
3. Islam, A. *et al. Chem. Lett.* **34,** 344–345 (2005).
4. Gao, F. *et al. J. Am. Chem. Soc.* **130,** 10720–10728 (2008).
5. Cid, J. *et al. Angew. Chem. Int. Ed.* **46,** 8358–8362 (2007).

NONLINEAR OPTICS

# Engineering Airy beams

The demonstration of Airy beam generation and all-optical control by quasi-phase matched nonlinear crystals looks set to help these unique beams realize their exciting potential in applications.

Valdas Pasiskevicius

In 1979, Berry and Balazs predicted a new set of solutions to the Schrödinger equation in the form of so-called Airy wave packets. Such wave packets have some unique and fascinating properties; namely, that such a wave propagates without changing its shape and follows a parabolic trajectory in free space (implying apparent acceleration even without the presence of an acting force)[1].

The leap from these quantum mechanical predictions to an experimental observation in the world of optics was reported almost 20 years later in 2007 by a group of researchers at CREOL, University of Central Florida[2]. The researchers succeeded in generating one-dimensional and two-dimensional truncated Airy beams by transmitting a Gaussian beam from an argon ion continuous-wave laser through a spatial phase modulator and subsequently applying an optical Fourier transformation onto the modulated beam.

Owing to their non-diffracting character (see Fig. 1), Airy beams are of great interest for many applications, such as microscopy, microfluidics, optical interconnects and optical manipulation of objects such as cells.

Until now, Airy beams have only been generated using linear diffractive elements. However, on page 395 of this issue[3], researchers from Tel-Aviv University, Israel describe a totally different approach based on nonlinear optics, which has several benefits. Tal Ellenbogen and co-workers show that a three-wave mixing process in a quasi-phase matched structure can be used to create Airy beams, opening the door to generation at new wavelengths and all-optical control of their trajectories.

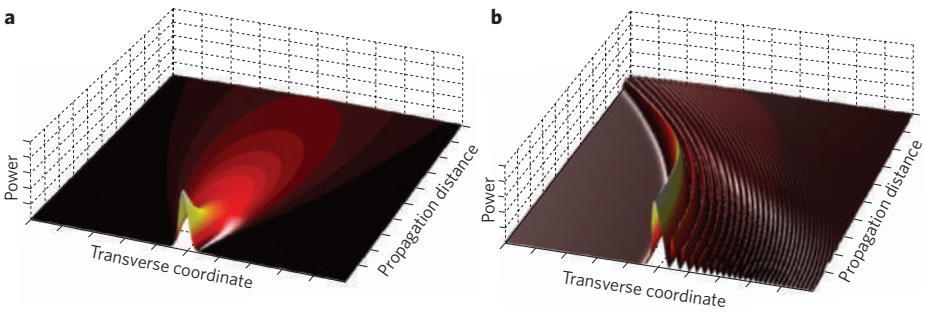


**Figure 1 |** Comparison of the power distribution in propagating Gaussian and Airy beams. Power distributions of a Gaussian beam (**a**) and an Airy beam (**b**). The width of the Gaussian beam corresponds to the width of the main peak in the Airy beam.

When performing nonlinear optics and nonlinear device design, quasi-phase matching offers two irresistible benefits. First, the dependence of the nonlinear conversion efficiency on the input wavelength is removed, so both of these crucial characteristics can become independent design parameters. The second unique benefit is that quasi-phase matching introduces an additional degree of freedom for designing the spatial distribution of the nonlinearity within the interaction area. This in turn gives control over the spatial distribution of the relative phases of the interacting waves and thus allows interactions that otherwise would be impossible within bulk nonlinear crystals. Some examples include multiple quasi-phase matched nonlinear interactions in two-dimensional nonlinear photonic crystals[4], counter-propagating interactions in structures with sub-micrometre periodicity[5], and the generation of structured beams in specially designed quasi-phase matched nonlinear crystals[6].

Inspection of the plane-wave decomposition of the Airy wave packet solution[1] indicates that introduction of an appropriate cubic phase modulation in the transverse plane of an initially collimated Gaussian beam can be used to generate one- or two-dimensional Airy beams. The significance of the current work by Ellenbogen *et al.* stems from the fact that they have experimentally demonstrated an efficient scheme for doing this based on quasi-phase matching in an engineered nonlinear crystal[3]. This represents a new path for generating Airy beams in contrast to previously reported methods that are based on linear optics.

To realize the nonlinear generation, Ellenbogen *et al.* designed and fabricated a quasi-phase matched structure in stoichiometric lithium tantalite nonlinear crystals using electric-field poling. The poling process allowed local control of the

sign of the quadratic coefficient, resulting in a periodic ferroelectric domain pattern in the crystals along the direction of beam propagation (see Fig. 2). This enabled second-harmonic generation of a Gaussian beam from a Nd:YLF laser. In one transverse direction, the periodic domain pattern was modulated by a cubic phase factor. A second-harmonic wave, generated from a nominally Gaussian beam that propagates in such a structure, will contain a transversally varying phase delay corresponding to the cubic phase factor. After subsequent optical Fourier transform, a second-harmonic one-dimensional Airy beam can be produced. This was indeed successfully demonstrated in the team's experiment — they reported that a second-harmonic Airy beam with a 42 W peak power was generated for a 3.6 kW pump peak power.

It is important to point out that this is more than just another way of producing Airy beams. The work demonstrates the potential of nonlinear optics and quasi-phase matching techniques to extend Airy beam generation into new wavelength regimes, as well as offering a new way of controlling and manipulating their fields. More specifically, Ellenbogen and co-workers experimentally demonstrate that the parabolic trajectory and the acceleration direction of the beams can be all-optically controlled by finely adjusting the phase mismatch in the nonlinear interactions. By using appropriately designed quasi-phase matched structures, Airy beams can, in principle, be generated at any wavelength within the transparency region of the nonlinear crystal, or at multiple wavelengths in a cascaded quasi-phase matched structure. Another advantage over conventional techniques is that the nonlinear optical generation method enables the generation of Airy beams with high peak and average powers via parametric amplification.

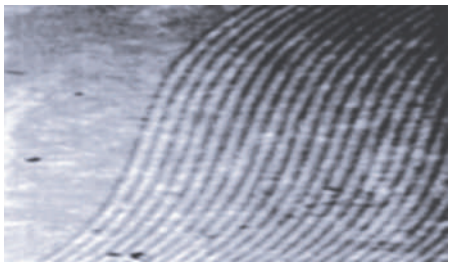

**Figure 2 |** Microscope photograph of the nonlinear crystals. Periodic ferroelectric domain pattern in the crystals along the beam propagation direction that is used to generate Airy beams.

One important parameter for any nonlinear generation process is the conversion efficiency. Although it varies with the peak power and the crystal length, it also depends on the quality of the quasi-phase matched structure. The conversion efficiency reported by Ellenbogen and co-workers amounts to 90% of that expected in a perfect, single-periodicity quasi-phase matched structure of the same length. This result is very encouraging, signifying good control over the spatial pattern of the ferroelectric domains. However, this high efficiency will probably be difficult to achieve for shorter wavelengths when the required quasi-phase matching period is reduced, or for longer crystals where phase errors accumulate along the interaction length.

It is also worth mentioning that two-dimensional Airy beams have been generated with spatial phase modulators[2]. At present, this could be hard to achieve directly from quasi-phase matched structures because three-dimensional patterning of the nonlinear coefficient is required and this is difficult to realize owing to the predominantly planar morphology of the ferroelectric domain walls. However, considering the planar geometry used in most microfluidic structures and photonic crystals, it might be more beneficial from the applications standpoint to embed the nonlinear Airy beam generator within a planar waveguide, thus restricting diffraction in one transversal direction while generating a non-diffracting accelerating Airy pattern in the other non-guiding direction. Despite these limitations, the achievement by Ellenbogen and co-workers represents a significant step towards generating and manipulating high-power Airy beams. ❐

*Valdas Pasiskevicius is at the Royal Institute of Technology, KTH, Roslagstullsbacken 21, 10691 Stockholm, Sweden.*
*e-mail: vp@laserphysics.kth.se*

## References

1. Berry, M. V. & Balazs, N. L. *Am. J. Phys.* **47,** 264–267 (1979).
2. Siviloglou, G. A., Broky, J., Dogariu, A. & Christodoulides, D. N. *Phys. Rev. Lett.* **99,** 213901 (2007).
3. Ellenbogen, T., Voloch-Bloch, N., Ganany-Padowicz, A. & Arie, A. *Nature Photon.* **3,** 395-398 (2009).
4. Broderick, N. G. R., Ross, G. W., Offerhaus, H. L., Richardson, D. J. & Hanna, D. C. *Phys. Rev. Lett.* **84,** 4345–4348 (2000).
5. Canalias, C. & Pasiskevicius, V. *Nature Photon.* **1,** 459–462 (2007).
6. Kurtz, J. R., Schober, A. M., Hum, D. S., Saltzman, A. J. & Fejer, M. M. *IEEE J. Sel. Top. Quantum Electron.* **8,** 660–664 (2002).

FREE ELECTRON LASERS

# First light from hard X-ray laser

The demonstration of lasing at 1.5 Å at the LCLS facility in the US marks an important landmark for free electron lasers.

Brian McNeil

In April, scientists at the SLAC National Accelerator Laboratory in Menlo Park, California announced that their recently completed free-electron laser (FEL) facility had achieved lasing at a wavelength of 1.5 Å ($1.5 \times 10^{-10}$ m). The news is important because their Linac (linear-accelerator-based) Coherent Light Source[1] (LCLS) is the first FEL operating in the hard X-ray regime. This is a landmark event in the history of light-source science, which will open up vast new areas for scientific exploration. Before the LCLS, the shortest wavelength record was held by the Free-Electron-LASer in Hamburg (FLASH) facility with 65 Å operation[2].

The short, ultra-bright pulses that the LCLS generates will allow unprecedented imaging of molecular and atomic processes. In September 2009, scientists will begin using these pulses in their experiments and, being first on the scene, they will undoubtedly reap many scientific rewards. Other FEL sources with similar wavelength specifications to the LCLS are currently being built and will be coming online over the next few years, notably the Japanese SPring-8 Compact SASE Source[3] (2010) and the European XFEL project[4] (2014). The hard X-ray FEL has come of age.

A free-electron laser is not like other lasers. It works by forcing a beam of electrons, travelling at nearly the speed of light, to oscillate in a long periodic lattice of (usually) permanent magnets called a 'wiggler'. The oscillating electrons emit

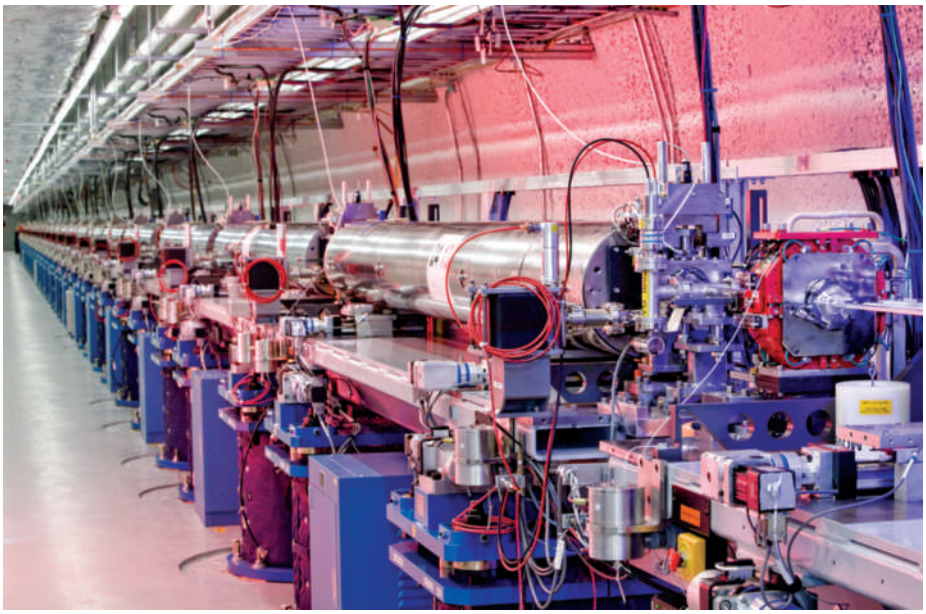

BRAD PLUMMER

**Figure 1 |** The LCLS undulator magnets create intense X-ray laser light by wiggling a pulse of electrons travelling near the speed of light. Courtesy of SLAC National Accelerator Laboratory

light that co-propagates with them on their journey along the wiggler. The faster the electrons travel, the shorter the wavelength of light emitted — the wavelength is proportional to the inverse square of the electron beam energy (~14 GeV in the LCLS). Using relatively short wigglers, this method has been applied in light-sources such as the European Synchrotron Radiation Facility to generate incoherent or 'spontaneous' radiation. In an FEL, however, the light and the electrons are allowed to co-propagate and interact in a wiggler over a much longer distance. In the LCLS, the wiggler length is just over 130 m.

In the wiggler, the electrons interact with each other via the co-propagating light that they emit. This 'collective' positive feedback interaction causes them to bunch together at the wavelength of the light. When bunched, the light emitted by each electron adds coherently to that emitted by the others, greatly increasing the power generated. In the LCLS, the electrons initially interact with the noisy spontaneous light, which is then amplified. This process has been called self-amplified spontaneous emission[5] (SASE). Eventually, the feedback process saturates as the electrons' energy becomes dispersed and they begin to lose their wavelength-scale bunching. One FEL scientist likened this process to a politician giving a speech and bringing the microphone too close to the audio speakers. The initial incoherent noise through the speaker (like the noise on the electron beam) gets amplified through the microphone (the light–electron interaction in the wiggler), raising the noise level, which is again picked up by the microphone, until the process runs away exponentially, eventually saturating the amplifier with a loud screeching tone (FEL power saturation).

The trick to achieving a successful SASE FEL interaction is to generate an electron beam of sufficient quality to allow it to bunch at the light wavelength (too much initial energy spread in the electrons, for example, washes out any bunching), and then to propagate the beam in as straight a line as possible through the wiggler to maintain a sustained coupling with the co-propagating light (no more than ~5 μm deviation over the ~130 m of wiggler in the LCLS). That is what the LCLS team did so spectacularly in April, allowing them to generate bursts of X-rays of unprecedented brightness. We in the light-source community collectively take our hats off to them for that achievement. Having spoken with some of the LCLS team, I think they amazed themselves at how quickly and successfully they got their machine working. This certainly bodes well in the build-up towards the first experiments in late summer for the reliability and stability of the source.

So why is this achievement so exciting? The number of useful photons for a user — the peak brightness — from an FEL operating at the LCLS target wavelength of 1.5Å should be at least eight orders of magnitude greater than is currently available from other sources. Clearly, where you get a change by a factor of $10^8$ in any field of science, particularly from a light-source, amazing new science will come within our grasp. This source will shine a giant searchlight into a dark landscape of atomic and molecular science where previously we stumbled with a candle.

With short wavelength (~1.5 Å), high power (multi-gigawatt) and short pulses (<100 fs), the X-rays from the LCLS will have the spatiotemporal resolution of molecular and some atomic processes — we will be able to 'see' how they work. As a result, the LCLS should yield new results for the analysis of all kinds of material placed in its path — be it elemental, inorganic, organic or biological. Not only that, the LCLS pulses will also be able to capture and image the delicate ephemeral processes of life. Using 'conventional' synchrotron light sources for X-ray imaging, many delicate samples are destroyed before sufficient information to form an image is gathered. However, the LCLS pulses will be sufficiently short and have enough photons to capture an image of the sample before its destruction. I think we can anticipate some beautiful and probably unexpected results.

The raw power of the LCLS at these short wavelengths will also prove important in the study of states of matter unfamiliar to us, such as warm dense matter, which occurs in cool dense stars, the cores of large planets and in the imploding fuel pellets of an internal confinement fusion reactor — a state of matter that is a half-way between solid and plasma.

Looking forward, one issue inherent to the SASE process that we would like to try to improve is the less-than-perfect temporal coherence of the X-ray pulses. As the initial source that is amplified by the FEL is the spontaneous emission from the electrons — essentially a noise signal — this means that after amplification, the temporal and spectral output is also rather noisy (ref. 5 and references therein). If a seed field with good coherence and of sufficient power to dominate the initial noise signal were available for injection into the FEL, then this would be a dream — the coherence properties of the seed would essentially be retained during FEL amplification. Although such seeds are available for longer wavelengths (≥10 nm), no such seed inputs currently exist for angstrom-scale wavelengths. Some more complex schemes involving the generation of harmonics from a beam seeded at the fundamental wavelength have been proposed and demonstrated at longer wavelengths[6],

but it appears problematic to achieve good coherence beyond 10 Å.

Also of interest is reducing the pulse durations into the attosecond regime (1 attosecond = $10^{-18}$ s), because this is the timescale at which things occur in atoms — in the Bohr model of the hydrogen atom it takes an electron about 150 attoseconds to orbit the nucleus. With the ability to probe the electronic processes within atoms at these timescales, to see how electron clouds reorganize themselves during molecular bond making and breaking, we could begin to unravel how all matter functions at this fundamental level. This regime may be approached at the LCLS using the so-called 'low-charge' regime of operation, which may generate pulses of ~1–2 fs at the longer wavelength of ~15 Å. However, there are a bucket-full of other ideas (ref. 7 and references therein) that may improve upon this and need to be investigated further for possible inclusion in future designs.

So far, both operational short-wavelength SASE FEL facilities — FLASH, and now LCLS — have piggy-backed on systems originally designed for particle physics applications, and both appear to function spectacularly. However, two new facilities are now being built from scratch — the Japanese SCSS and the European XFEL. It has taken since the early 1980s to develop these from the first ideas predicting how they would work. Current theory in the quantum regime of the FEL (ref. 8 and references therein) is beginning to point towards the possibility of extending FEL operation into the gamma-ray, giving access to the scale and energies of nuclear physics. Free-electron laser physics has a long way to run yet.

The LCLS result has created a real buzz within the FEL community. It is really encouraging to see a team of scientists being given the resources to show what can be done with a FEL. The LCLS team dared to suggest some years ago that they would like to put into practice the theoretical models for SASE FELs developed in the early eighties and build a hard X-ray FEL. Because they had an existing facility that they were able to adapt at SLAC, namely about 1 km of its 3-km-long linear accelerator originally built for particle physics research, they were first off the starting blocks in the race towards the hard X-ray. Now that they have achieved their goal they will undoubtedly gain many scientific and technological rewards that will follow when their high-brightness X-ray pulses are put to work. ❐

*Brian McNeil is in the Department of Physics, University of Strathclyde, Glasgow, G4 0N.*
*e-mail: b.w.j.mcneil@strath.ac.uk*

## References

1. http://home.slac.stanford.edu/pressreleases/2009/20090421-fact-sheet.htm
2. Tiedtke, K. *et al. New J. Phys.* **11,** 023029 (2009).
3. Tanaka, T. & Shintake, T. (eds) *SCSS X-FEL Conceptual Design Report* (RIKEN Harima Institute, 2005).
4. Altarelli, M. *et al.* (eds) *XFEL: The European X-Ray Free-Electron Laser, Technical Design Report* (DESY Hamburg, 2006).
5. Bonifacio, R., De Salvo, L., Pierini, P., Piovella, N. & Pellegrini, C. *Phys. Rev. Lett.* **73,** 70–73 (1994).
6. Doyuran, A. *et al. Phys. Rev. Spec. Top. AB* **7,** 050701 (2004).
7. Thompson, N. R. & McNeil, B. W. J. *Phys. Rev. Lett.* **100,** 203901 (2008).
8. Bonifacio, R., Piovella, N., Robb, G. R. M. & Serbeto, A. *Phys. Rev. A* **79,** 015801 (2009).

OPTICAL COMPONENTS

# LEGO lightens photonics

Researchers in Japan have shown that it is possible to use standard 'off-the-shelf' plastic toy parts to construct low-cost and light-weight optical components.

David Pile

It turns out that LEGO, the famous toy building bricks loved by children worldwide, may now have a promising future in the world of photonics. Japanese researchers have used standard LEGO parts to build sophisticated optical equipment, including spectrometers, Fourier image processors and tilt-or-tip optical mounts.

Junichi Takahara from Osaka University, who has been working on the idea for several years, told *Nature Photonics* that he is now preparing visual manuals for the LEGO schemes for uploading to a website shortly. His hope is that scientists and teachers will use his blueprints of portable and cheap optical experiments to inspire the minds of future generations of photonics researchers.

Takahara's interest in the idea can be traced back some ten years to when he was eagerly setting up a presentation for high-school students during an open campus day at Osaka University. The preparation included an optical experiment, and Takahara had to carry heavy optical mounts and an iron base plate from his laboratory to another building across campus. He realized then that there was a need for light-weight and compact optical components, and with his colleagues (Kazuhiro Manseki, Hiroshi Kawabata, Yasuchika Hasegawa, Tsuyoshi Konishi and Yasuo Kanematsu) became inspired to construct optical mounts and light sources from LEGO bricks as a useful learning tool. "For educational purposes, components that are low in cost and light weight compared with conventional iron-based optical mount systems are essential," Takahara told *Nature Photonics*. "By using LEGO bricks, science teachers can transport and perform optical experiments in any place easily, and it is affordable."

It is not the first time that scientists have considered using LEGO to construct optical mounts and equipment. Over 10 years ago an Italian group built a variety of impressive optical systems from LEGO[1,2]. However, their schemes require additional customized parts or additional processing of original LEGO bricks — they drilled or cut bricks and used glue to introduce customized extra non-LEGO parts, such as rods and springs. According to Takahara, his intention was to use off-the-shelf parts. "We don't want to use customized parts, so that the designs are accessible to everyone. You can obtain LEGO bricks all over the world and can even buy single blocks from the internet. Every LEGO part is uniquely numbered and listed in a database."

Two years ago, Takahara and his colleagues reported a set of optical parts, as well as transparent luminous blocks, that suit use as a light source[3]. Since then, his group has expanded and improved their designs so that they are more compact, use fewer bricks and offer new functionality such as tilt and rotation. Their latest designs were disclosed in April at the Laser Expo 2009, Yokohama, Japan.

Optical experiments developed by the team have so far been relatively simple, yet visually engaging, and are aimed at high-school and undergraduate students; for example, the team has a design for a LEGO spectrometer that takes a beam of white light from an LED

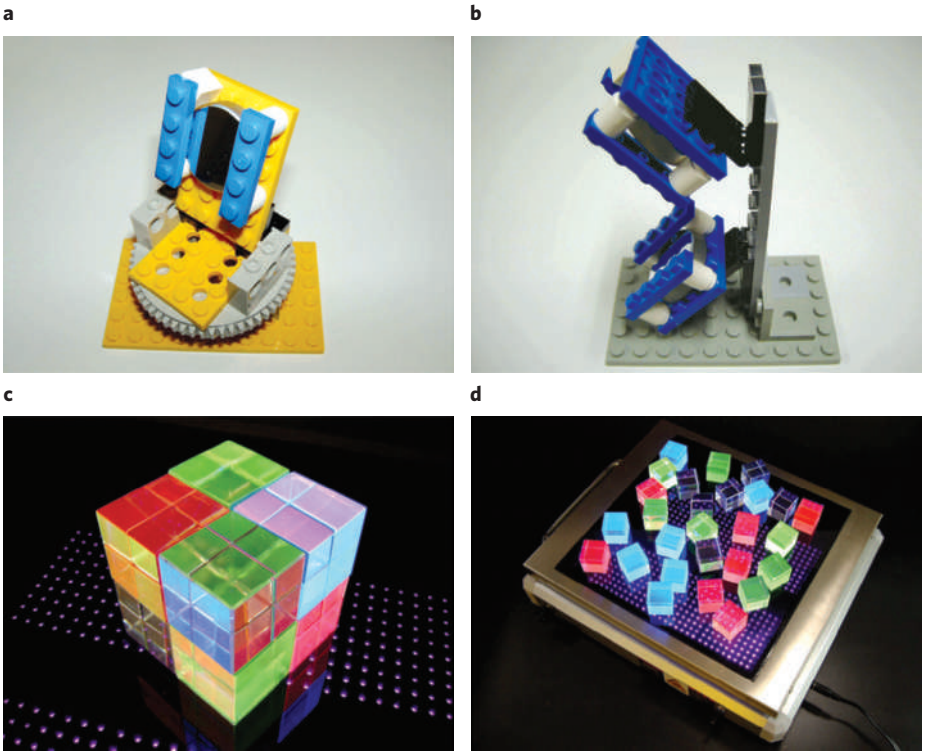


JUNICHI TAKAHARA/OSAKA UNIVERSITY

**Figure 1 |** Light-weight and low cost toys for science and education. **a**,**b**, Tilt-and-top optical mounts built from standard (unmodified) LEGO parts. **c**,**d**, Transparent luminous blocks excited by near-UV LEDs.

and, using a grating, disperses the rainbow of colours onto a screen. They have also developed a simple demonstration of image processing by Fourier optics. An input image is filtered through a high-pass filter, resulting in edge enhancement. However, the team is working towards realization of more advanced equipment, such as interferometers. "The main difficulty using only LEGO bricks is horizontal adjustment," explained Takahara. "We can move the bricks horizontally, but we need complicated structures. That is why the Italian group employed additional parts. However, we think we can overcome this."

The Japanese team has also developed a set of luminous transparent resin bricks that contain fluorescent organic molecules. The blocks are transparent but emit visible light at wavelengths of approximately 615 nm (red), 547 nm (green) or 420 nm (blue) when excited by near-UV LEDs.

"It is very important that the molecules have a very high quantum efficiency of more than 90%. That way we only need a small amount (0.1–1.0% by weight) of molecules, resulting in retaining the transparency of the resin after doping," said Takahara. "In addition, the molecules used are not toxic; this is important for educational toys". Both the LEGO and luminous block systems are lightweight and easily portable, says Takahara. "I recently gave a lecture in Yokohama and was able to bring both systems by myself from Osaka in my bag," he commented. "Not surprisingly, many people are thinking that the luminous bricks are a good design toy for adults, not for children — they want it for themselves".

Junichi Takahara can be contacted for more information and updates by e-mail (takahara@ee.es.osaka-u.ac.jp). ❐

*David Pile is at Nature Photonics, Chiyoda Building, 2–37 Ichigayatamachi, Shinjuku-ku, Tokyo 162–0843, Japan.*
*e-mail: d.pile@natureasia.com*

## References

1. Bell, J. *Opt. Laser Eur.* 32–34 (October 1997)
2. Quercioli, F., Tiribilli, B., Mannoni, A. & Acciai, S. *Appl. Opt.* **37**, 3408–3416 (1998).
3. Takahara, J., Manseki, K. & Konishi, T. *Oyo Buturi* **76**, 34–38 (2007).

PHOTOACOUSTIC TOMOGRAPHY

# Sounding out fluorescent proteins

Researchers from Munich and Boston have shown that multispectral photoacoustic tomography can image fluorescent proteins buried deep in highly scattering living organisms.

Peter Burgholzer, Hubert Grün and Alois Sonnleitner

Is it possible to listen to light? Yes, it is — and it's called photoacoustics. In 1880, Alexander Graham Bell discovered that pulsed light striking a solid substrate can produce a sound wave, a phenomenon called the photoacoustic effect[1]. It is only relatively recently that practical imaging methods based on this effect have been developed and reported[2]. Today, photoacoustic tomography (PAT), which is also referred to as optoacoustic tomography, is attracting intense interest for cross-sectional or three-dimensional imaging.

On page 412 of this issue[3], Razansky *et al.* experimentally demonstrate the ability to image gene expression using PAT in highly scattering models and living organisms at depths beyond the capabilities of traditional light microscopy. Through genetic manipulation, fluorescent proteins are attached to target molecules of interest within *Drosophila* pupa and adult zebrafish. Subsequent whole-body imaging of these organisms allows visualization of tissue-specific expressions of proteins for morphological and functional observations. The application of the technique to two biologically important but optically diffuse model organisms shows great promise for understanding the complexity of live organisms as required for next-generation system biology.

So how exactly does photoacoustic imaging work? In summary, short laser pulses are fired at a sample (Fig. 1) and the absorbed energy causes local heating. This heating causes thermoelastic expansion and the generation of broadband elastic pressure waves (ultrasound) which can be detected outside the sample, for example by a piezoelectric device.

A map or 'image' of the photogenerated pressure distribution in the sample can be made by collecting the ultrasound at many different locations and processing it using a suitable algorithm, for example a filtered back-projection algorithm or a time-reversal algorithm. Only if the laser pulse is short enough will thermal expansion cause a pressure rise proportional to the locally absorbed energy density[4]. Any photons, either unscattered or scattered, contribute to the absorbed energy as long as the photon excitation relaxes by thermal means. Therefore PAT visualizes the product of the optical absorption distribution and the local light fluence.

Using a Nd:YAG laser and an optical parametric oscillator, it is possible to use light pulses from the infrared to the visible regime with a repetition rate from 10 Hz up to 100 Hz. Some high-speed PAT systems can even go up to 1,000 Hz. Pulse duration in the nanosecond range allows a theoretical resolution of several micrometres in tissue (sound velocity similar to water at about 1,500 m $s^{-1}$). For biomedical applications the light energy should not exceed 20 mJ $cm^{-2}$.

What is the advantage of photoacoustic imaging over other, purely optical imaging methods? In biological tissues, traditional optical imaging suffers from scattering. The mean free path between two scattering events is of the order of just 0.1 mm (ref. 5). Another important depth limit is of the order of 1 mm, where the (quasi)diffuse regime starts. Here, owing to many scattering events, the photons have (almost) lost their memory of their original incidence direction. None of the available optical imaging modalities (including confocal microscopy, two-photon microscopy and optical coherence tomography) can provide high-resolution imaging in this regime. By contrast, photoacoustic imaging, where ultrasonic waves transport the information about the local absorbed energy to the surface of the sample, can operate in this (quasi)diffuse regime, because ultrasonic scattering in biological tissues is two to three orders of magnitude less than optical scattering[2].

Using a fixed laser wavelength that provides high optical contrast for excitation will lead to morphological information on the sample, for example on the structure of blood vessels. Inspired by other medical imaging technologies, PAT is now being developed into a multispectral imaging method by acquiring images excited with different wavelengths. From such a set of data, additional functional information such as the oxygen saturation in the blood vessels can be calculated, based on the unequal absorption of oxygenated or deoxygenated blood at different excitation wavelengths[6]. A recent development in multispectral imaging has been molecular imaging using molecules that are strong optical absorbers at the specific wavelengths used[7]. However, few intracellular molecules are known to provide such specific absorption, and absorbing molecules have so far had to be applied exogeneously[5].

Fluorescent proteins are widely used in cell biology and in the study of transgenic animals, because they can be genetically targeted to a specific molecule of interest. On excitation with a laser beam of a suitable wavelength, such proteins emit fluorescence which can be detected, thus identifying the molecule of interest. But it is their steep change in absorbance as compared with the background tissue absorption that provides contrast and hence makes them an ideal reporter molecule for PAT.

The attraction of photoacoustic imaging of fluorescent proteins is that it overcomes the limitations of conventional fluorescence microscopy and allows imaging of gene expression in much deeper tissue regions. Razansky *et al.* report that multispectral PAT can achieve a penetration of several millimetres (or, potentially, centimetres) with a resolution in the range of 20–100 μm, which remains constant as a function of depth and depends only on the ultrasonic detector characteristics[3]. An additional influence on resolution arises from frequency-dependent acoustic attenuation in tissue. Also, the stronger damping of higher frequencies limits the bandwidth of the photoacoustic signal and therefore may reduce the resolution in deeper tissue regions.

A challenge for future work is based on the fact that PAT visualizes the product of the local optical absorption and the light fluence. Razansky *et al.* have assumed that the light fluence changes by less than 5%, basing this on calculations using the light diffusion equation. Light transport modelling may provide more specific information on fluence changes[8], leading to improved results.

It will be interesting to see how the technique operates on biologically relevant timescales of seconds rather than minutes. In general, higher spatial resolution also requires improved time resolution to observe processes in sufficient detail. The use of detector arrays, as described for example by Yin[9], is one approach that can reduce measurement time significantly. Nonetheless, Razansky *et al.* have made an important step in providing high-resolution whole-body imaging of fluorescent proteins produced in the cells of genetically manipulated organisms. ❐

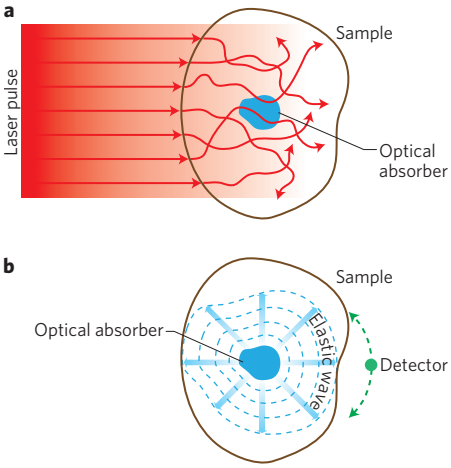


**Figure 1 |** Photoacoustic imaging. **a**, Propagation of light in tissue. Traditional optical imaging methods suffer from scattering in biological tissues. **b**, Propagation of ultrasound in tissue. Using laser pulses to generate elastic pressure waves (ultrasound) allows high-resolution optical information to be obtained. Ultrasonic scattering is two to three orders of magnitude weaker than optical scattering.

*Peter Burgholzer and Hubert Grün are at the RECENDT GmbH (Research Center for Non-destructive Testing), Hafenstr. 47–51, 4020 Linz, Austria. Alois Sonnleitner is at the Upper Austrian Research GmbH, Department for Biomedical-Nanotechnology, Scharitzerstr. 6–8, 4020 Linz, Austria.*
*e-mail: peter.burgholzer@recendt.at*

## References

1. Bell, A. G. *Am. J. Sci.* **20,** 305–324 (1880).
2. Xu, M. H. & Wang, L. V. *Rev. Scient. Instr.* **77,** 041101 (2006).
3. Razansky, D. *et al. Nature Photon.* **3,** 412–417 (2009).
4. Gusev, V. E. & Karabutov, A. A. *Laser Optoacoustics* (AIP-Press New York, 1993).
5. Wang, L. V. *Med. Phys.* **35,** 5758–5767 (2008).
6. Li, M. *et al. Proc. IEEE* **96,** 481–489 (2008).
7. Li, L., Zemp, R. J., Lungu, G., Stoica, G. & Wang, L. V. *J. Biomed. Opt.* **12,** 020504 (2007).
8. Cox, B. T., Arridge, S. R., Kostli, K. P. & Beard, P. C. *Appl. Opt.* **45,** 1866–1875 (2006).
9. Yin, B. *et al. Phys. Med. Biol.* **49,** 1339–1346 (2004).

LIGHT-EMITTING NANOCRYSTALS

# An end to blinking

Light-emitting semiconductor nanocrystals are potentially useful for tasks such as single-molecule biological imaging and the creation of single-photon sources and low-threshold lasers, but so far they have always had a serious drawback. When optically pumped, even by continuous-wave light, they blink. This erratic switching on and off of their photoluminescence causes problems because it not only makes them harder to image but also leads to unpredictable fluctuations in the number of photons emitted and in their emission time.

It now seems that there could be an end to such woes. Xiaoyong Wang and co-workers from the University of Rochester, Eastman Kodak, Cornell University and the Naval Research Laboratory have succeeded in fabricating composite nanocrystals that, they say, can suppress the blinking completely on timescales of many minutes (*Nature* doi:10.1038/nature08072). Their nanocrystals consist of an alloyed core of CdZnSe surrounded by a shell of ZnSe.

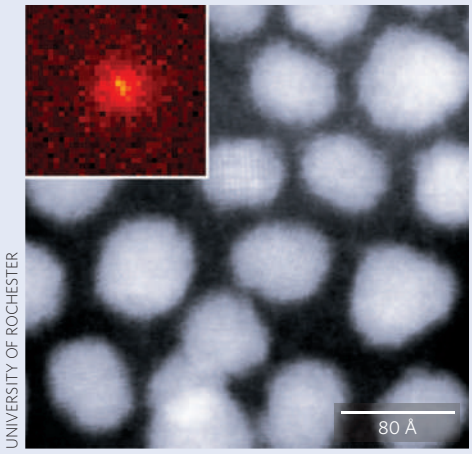


UNIVERSITY OF ROCHESTER

When pumped with green (532-nm) light the nanocrystals emit red (~620-nm) light which is steady and stable in intensity.

For many years scientists have been trying to discover what causes the blinking and to prevent it. Although a complete picture is still not clear, the general consensus is that the blinking is caused by the presence of extra electrical charges in a nanocrystal. This greatly increases its non-radiative (Auger) decay rate, thus allowing an excited nanocrystal to shed its excess energy in ways other than emitting light.

In contrast, it seems that the formulation of the nanocrystals produced by Wang *et al*. leads them to emit light through a transition involving a trion (a charged exciton) for which competing non-radiative Auger decay process are greatly weakened.

OLIVER GRAYDON

nature photonics

FOCUS | PROGRESS ARTICLE

PUBLISHED ONLINE: 29 JUNE 2009 | DOI: 10.1038/NPHOTON.2009.112

# Diffraction-unlimited three-dimensional optical nanoscopy with opposing lenses

Stefan W. Hell*, Roman Schmidt and Alexander Egner

**The resolution of far-field optical microscopy stagnated for a century, but a quest began in the 1990s leading to nanoscale imaging of transparent fluorescent objects in three dimensions. Important elements in this pursuit were the synthesis of the aperture of two opposing lenses and the modulation or switching of the fluorescence of adjacent markers. The first element provided nearly isotropic three-dimensional resolution by improving the axial resolution by three- to sevenfold, and the second enabled the diffraction barrier to be overcome. Here, we review recent progress in the synergistic combination of these two elements which non-invasively provide an isotropic diffraction-unlimited three-dimensional resolution in transparent objects.**

Despite the enormous resolution afforded by electron and scanning probe microscopy, far-field optical microscopy has maintained its key role in a number of areas, particularly in the life sciences. The reason is a series of key advantages of imaging with propagating fields of light, such as the non-invasive access to the interior of (living) cells, and the sensitive detection of macromolecules by fluorescence tagging. In fact, far-field fluorescence microscopy would be almost ideal for non-invasively investigating the three-dimensional (3D) interior of transparent objects in biology and material sciences if it could discern details that are substantially smaller than half the wavelength of light, $\lambda$. However, until not very long ago, realizing nanometre-scale resolution with conventional lenses and focused visible light seemed to be impossible because of diffraction[1,2].

The limiting role of diffraction stems from the fact that the full-width half-maximum (FWHM) of the intensity point-spread function (PSF) $h(\mathbf{r}) = h(\rho,z)$ — that is, the spatial light intensity pattern in the focal region of an objective lens — extends over at least $\Delta\rho \approx \lambda/(2n\sin\alpha) > 180$ nm in the focal plane and $\Delta z \approx \lambda/(n\sin^2\alpha) > 450$ nm along the optic axis, with $\alpha$ denoting the semiaperture angle of the lens and $n$ denoting the refractive index of the medium. In the PSF, $\mathbf{r}$ is the position vector in the sample space, and $\rho$, $z$ are its coordinates in a cylindrical coordinate system. Features that are closer together than these dimensions can yield a (fluorescence) signal at the same time, so the individual signals cannot be discerned. Likewise, imaging a point object from the focal region of the lens to a camera is governed by a similar PSF, $h_{em}(\mathbf{r})$, which blurs the spatial coordinate of the object. Therefore, until the advent of the first concrete concepts for breaking the diffraction resolution barrier in the early 1990s, it had been widely accepted that optical imaging at the nanoscale would not be viable with freely propagating light waves. The only pathway seemed to be offered by near-field optical microscopy, confining the light–specimen interaction with a nanosized tip[3–5] (see also the review article on page 388 of this issue[6]). However, tip-confined non-propagating light waves may not image the interior of transparent objects and hence they are largely limited to imaging surfaces. Because this technique also relies on collecting and amplifying non-propagating waves, similar practical limitations currently also apply for imaging with a metamaterial lens of negative refractive index[7]. Meanwhile, the early concepts of diffraction-unlimited far-field optical microscopy[8–10] have been validated[11,12], expanded[13–15] and applied[16]. Moreover, they have been recently complemented with other powerful techniques[17–20] that have greatly extended the range of implementation and application of diffraction-unlimited far-field optical nanoscopy.

## Aperture increase and signal switching

Several advancements have contributed to attaining the current record values of far-field optical 3D resolution of < 50 nm. Yet when analysing their basic physical principles, two unrelated elements come into sight, which, harnessed in various optical arrangements, have provided major leaps in 3D far-field optical resolution: increasing the solid aperture angle of the microscope by the coherent use of two opposing lenses[10,21–26]; and the breaking of the diffraction barrier by switching or modulating the signalling (fluorescence) ability of markers that are closer than the diffraction limit to enable their separate registration[8,9,13,17–19,27].

The microscope's total aperture is increased by counter aligning two large angle lenses and coherently adding the spherical wavefront caps of the excitation light at the sample, or of the emitted fluorescence light at a common detector[21,22]. With lenses featuring a semiaperture angle $\alpha$ greater than about 65°, this approach virtually mimics the use of a nearly full solid angle of $4\pi$ and concomitantly removes the asymmetry along the optic axis in focal spot formation, which is the actual reason for the poorer resolution along the optic axis ($\Delta z > 2.5\ \Delta\rho$) in single-lens imaging. The coherent synthesis of the spherical wavefront caps of opposing lenses is the essence of scanning 4Pi microscopy, where either the excitation photons interfere at the sample (4Pi type A) and/or each emitted fluorescence photon interferes with itself at the detector (4Pi type B and C), after having simultaneously passed through both lenses[22,28]. As a result, the axial FWHM of $h(\mathbf{r})$ or $h_{em}(\mathbf{r})$ is reduced by three- to fourfold over the typical axial FWHM obtainable with a single high-angle lens, and the main maximum is more spherical. Sharpening both $h(\mathbf{r})$ and $h_{em}(\mathbf{r})$, as in 4Pi type C, improves the axial resolution up to about 70–100 nm (refs 22,28,29). The related concept, I$^5$M (refs 23,25,30), and its extension I$^5$S (ref. 26), which adds laterally structured illumination, also coherently collect fluorescence photons through both lenses thus attaining a similar or even 1.5-fold better 3D resolution in parallelized camera-based imaging. The significantly improved axial and hence nearly isotropic 3D resolution obtained through the spherical wavefront synthesis drastically improved the 3D imaging of cells, albeit within the limits set by diffraction.

By enabling sequential detection of adjacent 'identical' fluorescent features irrespective of their distance, the diffraction limit can be overcome fundamentally[8,9,13,17–19,27,31]. This can be done by modulating or switching the signalling ability of these features. The

Max Planck Institute for Biophysical Chemistry, Department of NanoBiophotonics, 37070 Göttingen, Germany. *e-mail: hell@nanoscopy.de

switching of a marker's ability to fluoresce, or to signal in general, implies a manifest transfer of the fluorophore from a signalling (fluorescent) 'on' state, A, to a non-signalling (non-fluorescent) 'off' state, B, or vice versa, such that only one of the states is noticeably occupied[13,27]. One way of realizing (fluorescence) switching is to prohibit one of the two states, say A. This is possible by subjecting the fluorophore to a light intensity that causes a saturated optical transition from A to B, depleting A. If the fluorophore happens to end up in A for some reason, it is so rapidly transferred to B that its dwell time in A is negligible. If the depletion of A is predominant and not contended by adverse optical transitions, the probability that the fluorophore is in the state A simply scales with $\exp(-I/I_s)$ (refs 12,27). $I$ denotes the applied light intensity and $I_s$ is a fluorophore-characteristic (saturation) intensity that depends on the lifetime of the two states.

For example, exposing the fluorophore to an intensity of $I >> I_s$ induces stimulated emission from the fluorescent state to the ground state and effectively prohibits the fluorescent state. Hence the fluorophore is essentially confined to its ground state, which is equivalent to switching the fluorophore off[8]. It is instantly switched on again when the stimulating beam is interrupted. Conversely, a saturated excitation depleting the ground state switches fluorescence on to its maximum level, and back off again if the beam is interrupted[14,15]. Mechanisms that demand less intense beams and lower $I_s$ include the switching of the fluorophore between (meta) stable fluorescence-active and fluorescence-inactive states[13,31], such as the transfer between the fluorescent singlet and the metastable dark triplet state[9] (flip of an electron spin), or between conformational (*cis–trans*) fluorescent and non-fluorescent states in organic fluorophores and photoactivatable fluorescent proteins[13,17–19,31] (position flip of fluorophore atoms). Other options for switching the signalling ability of the fluorophore are changes in binding states, including that of diffusible fluorophores[32].

As all these mechanisms have been used for overcoming the diffraction barrier, one can classify the various nanoscopy methods according to the switching or fluorescence modulation mechanism used[27]. However, upon analysing the way in which the switching is implemented and the position of the fluorophores registered, they fall into two distinct categories: in the targeted mode, the coordinates at which the fluorophore is switched (to A or B) is defined at any point in time; whereas in the stochastic category, individual fluorophores are switched randomly in space[27]. The archetypes of the first category are stimulated emission depletion (STED) and ground state depletion (GSD) microscopy, whereas that of the latter is the concept called (fluorescence) photoactivation localization microscopy (PALM[17,33] or FPALM[19,34]) or stochastic optical reconstruction microscopy (STORM)[18,35] (see also the commentary article on page 365 of this issue)[36]. The related concept PALMIRA[20] switches single molecules stochastically both in space and in time.

## Resolving by targeted signal switching

In the targeted (STED-like) mode, defining where the fluorophore is in A or B is accomplished by forcing the fluorophores to reside in one of the two states, say in B, by applying an intensity $I(\mathbf{r})$, and therefore prohibiting the other state (A), say in proportion to $\exp[-I(r)/I_s]$. Importantly, $I(\mathbf{r})$ is structured such that it features at least a single deep minimum, ideally a zero, at one or more predefined coordinates, $\mathbf{p}_i$, in space: $I(\mathbf{p}_i) = 0$. Because the resolution is to be increased in three dimensions, the zero is bordered by a doughnut-shaped intensity maximum $I_m^{\rho} := \max[I(\rho,0)]$ in the focal plane, and two peaks $I_m^{z} := \max[I(0,z)]$ along the optic axis. By adjusting $I_m^{\rho}$, $I_m^{z} >> I_s$, the fluorophore can remain in A exclusively at $\mathbf{p}_i$, and its immediate proximity in which $H(\mathbf{r}) := \exp[-I(\mathbf{r})/I_s]$ is non-negligible. In this high-intensity approximation, $H(\mathbf{r})$ does not depend on $h(\mathbf{r})$ and assumes the role of the (fluorophore-state-dependent) effective PSF of the imaging modality. Close to the zero, we can approximate $I(\mathbf{r})$ quadratically by writing $I(\mathbf{r}) \approx (2\pi n/\lambda)^2[I_m^{\rho}(\beta^{\rho}\rho)^2 + I_m^{z}(\beta^{z}z)^2]$ with geometric parameters $\beta^{\rho}$ and $\beta^{z}$ quantifying the steepness of the well[37] in the radial and axial direction, respectively. Typically, $\beta^{\rho} \approx 0.5$ for a high-angle lens doughnut and $\beta^{z} = 1$ for a flat standing wave. As a measure of the lateral and axial resolution, the FWHM of $H(\mathbf{r})$ is derived as

$$\Delta\rho, \Delta z \approx \frac{\lambda}{\pi n \beta^{\rho,z}} \sqrt{\frac{\ln 2}{I_m^{\rho,z} / I_s}} \qquad (1)$$

From $I_m^{\rho}$, $I_m^{z} >> I_s$ it follows that $\Delta\rho$, $\Delta z << \lambda/(2n\sin\alpha)$. In this scheme, detectable features or molecules that are further apart than $\Delta\rho$ or $\Delta z$ are forced to differ by their state, which makes them separable for the time period in which this state gradient is maintained in space. Translating the zero through the sample sequentially brings them to the detectable state (say A), which allows an image of resolution $\Delta\rho$ or $\Delta z$ to be set up. In contrast, those fluorophores lying within $\Delta\rho$ or $\Delta z$ can emit their signal at the same time. Therefore, the total signal pertinent to a given coordinate pixel can be tuned through $\Delta\rho$ and $\Delta z$. More importantly, by varying $I_m^{\rho}$ and $I_m^{z}$ between 0 and $\infty$, one can theoretically tune the resolution of $\Delta\rho$ and $\Delta z$ between the diffraction limit and the molecular scale.

Concretely, in STED microscopy[8,11], the diffraction-limited focal spot formed by the beam of light exciting the fluorophores is overlapped with a 'holey' focal intensity distribution $I_{STED}(\mathbf{r})$ with $\lambda$ at the red edge of the emission spectrum of the fluorophore, so as to render stimulated emission as the predominant event in comparison to undesired excitation by $I_{STED}(\mathbf{r})$ or spontaneous emission. At coordinates where $I_{STED}(\mathbf{r}) >> I_s$, the fluorophore spends virtually no time in the excited state (A) and hence effectively remains off (in B), even if it is subject to the stream of photons provided by the excitation beam. The spatial region in which the fluorophore can be active, that is, effectively reside in A, is given by equation (1). Note that because $I_m^{\rho}$, $I_m^{z} >> I_s$ is assumed here, the unity in the square root of the denominator encountered in other versions of this equation[27,37] can safely be ignored.

## Separating objects by stochastic single molecule switching

In the stochastic (PALM-STORM-like) switching and read-out mode[17–20,33–35,38–41], individual fluorophores that are initially in a dark state B turn up in a bright state A at unknown coordinates $\mathbf{p}_i$. The state A is such that it is able to place $m >> 1$ detected photons (for example, through repeated excitation A↔A*) on a camera, mapping out $h_{em}(\mathbf{r})$. This scheme does not require an $I(\mathbf{r})$ featuring a zero, but a state A that yields $m >> 1$ detected photons. By considering the local fluorophore concentration in the adjustment of the excitation intensity so that only one molecule is in state A within range $\lambda/(2n\sin\alpha)$, the unknown coordinate $\mathbf{p}_i$ is then calculated ('localized') from the centroid of $h_{em}(\mathbf{r})$ with subdiffraction precision $\Delta\rho \approx \lambda/(2n\sin\alpha\sqrt{m})$ in the focal plane[17–19]. Finally, the fluorophore is switched off again from A→B, so that an adjacent molecule can be read out using the same cycle B→A→B. If the molecule is read out only once, the initial and the final dark state B need not be identical; the final state B can be a 'bleached' state. The image is assembled mathematically by localizing a representative number of molecules. We note that switching between two states using a saturated optical transition is an optically nonlinear phenomenon. The molecular switching and onset of $m$ photons emitted and detected from the same molecule is also a highly nonlinear (of $m$th order) phenomenon.

In any case, the two switching-based imaging modalities are complementary[27]. Imaging in the targeted mode can be very fast, because the molecular coordinate $\mathbf{p}_i$ is known and a few photons are enough to indicate the presence of an object at the known coordinate. In addition, the average number of jointly detectable

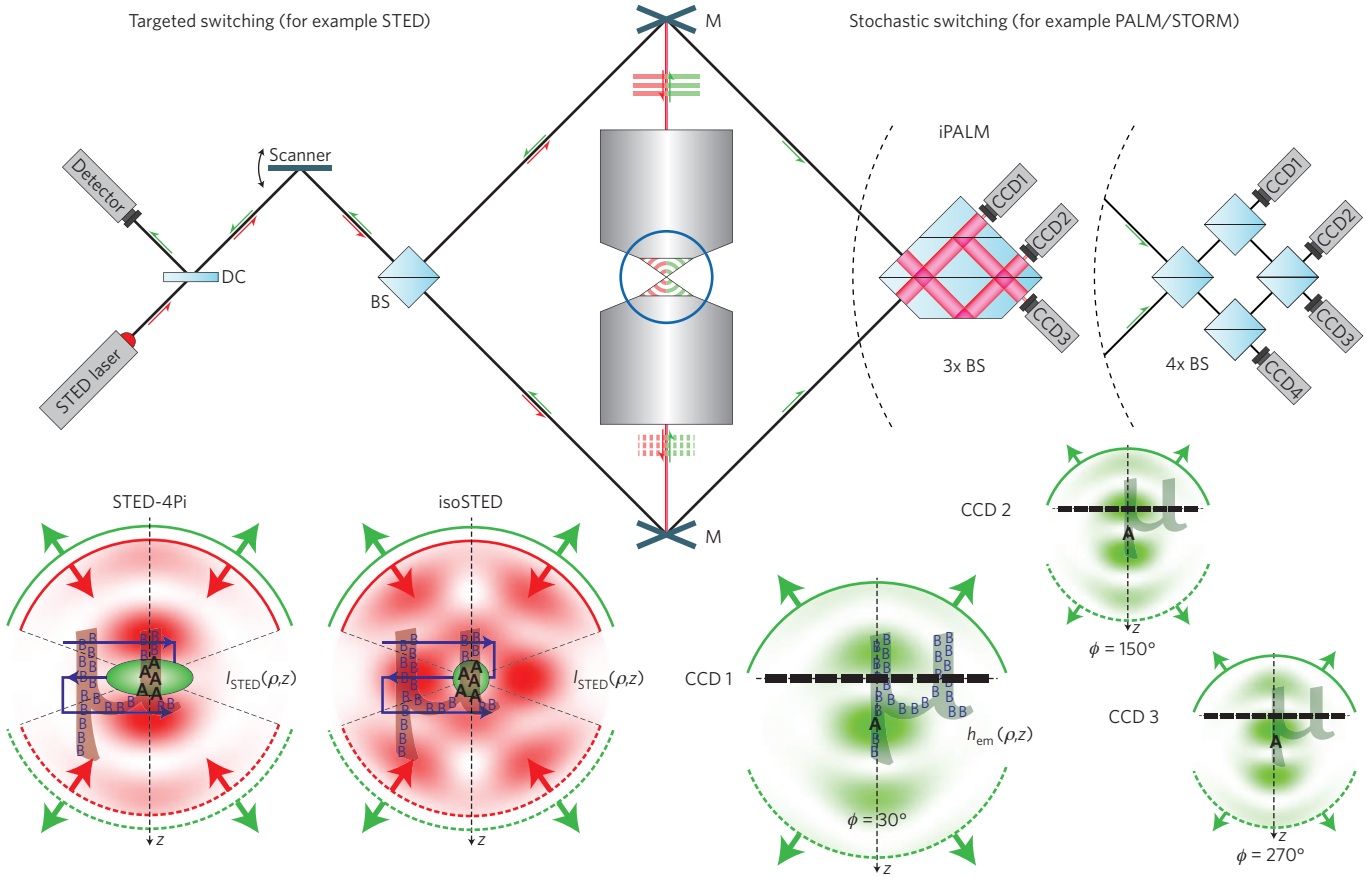


**Figure 1 | Maximizing 3D resolution in far-field fluorescence nanoscopy by expanding the illumination and/or the detection aperture of the microscope with opposing lenses.** The common focal region of the opposing lenses (blue circle) is sketched in the lower-left and lower-right panels for both imaging modalities. Left: targeted switching modality exemplified by STED microscopy implemented with a beam scanner. The STED laser beam is split into coherent parts so that they interfere destructively at the focal region rendering an $I_{STED}(\mathbf{r})$ with a central zero. The PSF describes the region in which the fluorophore is allowed to reside in the fluorescence 'on' state A, with FWHM $\Delta\rho$ and $\Delta z$ as given by equation (1). Fluorophores outside this (green) region are forced by $I_{STED}(\mathbf{r})$ to reside in the dark state B. The concept can be extended to other switching mechanisms between two states. Nanoscopy images are gained by scanning the (green) region through the transparent object (here a 'μ') in 3D. Right: In the stochastic fluorophore switching modality, such as PALM or STORM, molecules are switched on and off individually, and the $m >> 1$ photons emitted from the on-state A are used for 3D localization. Interferometric PALM (iPALM) or single-molecule switching (SMS) combine the two spherical wavefront caps pertinent to fluorescence emission with a set of splitters (three in iPALM), re-dividing them such that partial wavefronts with distinct equidistant phase differences (for example, $\phi$ =30°, 150°, 270° in iPALM) are created. An emitting fluorophore produces three different intensity patterns on the cameras, CCD1, CCD2, and CCD3, placed after each splitter outlet. These patterns represent magnified lateral $(x,y)$ cross-sections of a 4Pi detection PSF at the corresponding $\phi$, as indicated in the panels beneath the scheme. Owing to the strong dependence of their central and total brightness on the $z$ coordinate, these $xy$ patterns localize the emitter (in state A) with improved sensitivity in $z$, but at the same time allow the localization in the $xy$ plane. The triple-splitter used in iPALM is an elegant implemention of the minimum number of splitters required for this detection scheme, which can also be implemented using four cascaded splitters and four camera detection areas (top right). Differences between the targeted and the stochastic modalities are that the first (for example, isoSTED) usually uses focused beams for excitation or fluorescence activation, whereas the latter (for example, iPALM) conveniently illuminates the sample in the wide field. DC, dichroic mirror; BS, beam splitter; M, mirror.

fluorophores can be adjusted by varying $\Delta\rho$ and $\Delta z$. A strength of the stochastic mode is that a spatially structured $I(\mathbf{r})$ is not required and each fluorophore has to undergo only a single cycle of B→A→B to contribute to the image[27]. In contrast, the targeted mode requires optically induced multiple cycling, which is often challenged by molecular degradation. However, irrespective of the particular strengths and weaknesses of each modality, using just a single lens always implies that a large spectrum of the solid aperture angle is not covered. Therefore, coherently using opposing lenses automatically provides an improved axial and more isotropic 3D resolution in both the targeted[10,12,42] and the stochastic switching approach[43,44] (Fig.1). For all these reasons, in the most recent efforts to maximize the 3D resolution of STED[45] and PALM[44], coherently using opposing lenses has (re-)assumed an important role.

## Targeted switching using opposing lenses

In a targeted mode, such as STED microscopy, counter-propagating spherical wavefronts can concretely be used to create an $I(\mathbf{r}) = I_{STED}(\mathbf{r})$ featuring a local minimum with an axial FWHM that is slightly larger than $\lambda/(4n)$ (refs 10,12,42). The minimum has a larger intensity gradient, $\beta^z$, than can be created by destructive interference using a single wavefront cap, owing to the faster change of the relative phase in the interference of counterpropagating beams. For this reason, an early implementation of STED with opposing lenses, called STED-4Pi microscopy[10,12], enabled $\Delta z = 35$–$55$ nm, and hence made nanoscale imaging of bacteria cell membranes and microtubuli in fixed cells possible[42]. However, as $\beta^\rho << \beta^z$, STED-4Pi microscopy did not really improve the resolution in the focal plane. Therefore, the most recent dual-lens implementation of STED, called isoSTED micros-

NATURE PHOTONICS DOI: 10.1038/NPHOTON.2009.112

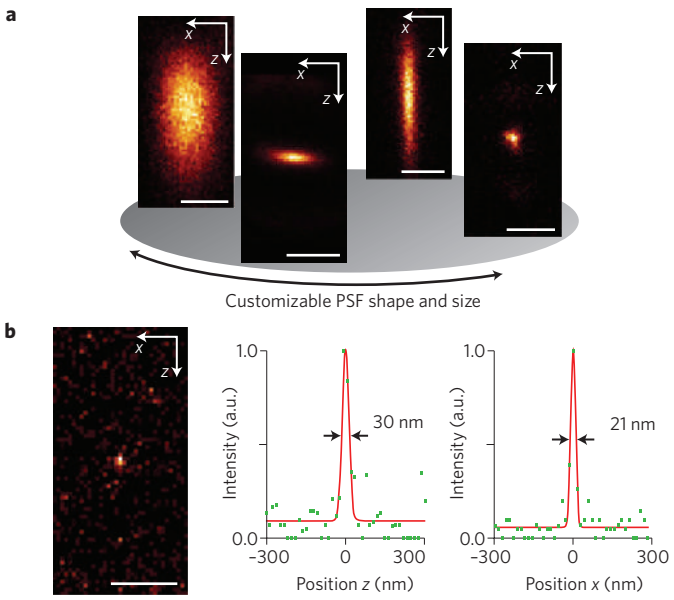


**Figure 2 | PSF shaping in a targeted fluorophore switching modality.** **a**, By using the proper switching intensity distribution $I_{STED}(\mathbf{r})$, the PSF $H(\mathbf{r})$ of the imaging system — given by the subdiffraction region in which the fluorophore can reside in an emitting state — can be tailored to optimize signal and imaging speed. Panels compare PSFs of (from left to right) the standard confocal, an oblate STED-4Pi PSF, a prolate STED-PSF produced by a toroidal $I_{STED}$ with a doughnut-shaped cross-section in the focal plane, and a spherically shaped isoSTED-PSF. **b**, Currently, PSF dimensions of down to $\Delta z = 30$ nm axial and $\Delta\rho = 21$ nm lateral FWHM indicate that the effective PSF volume can be squeezed by at least three orders of magnitude with respect to its confocal counterpart. All PSFs were probed with fluorescent beads in the same setup: bead diameter ~40 nm (**a**), <20nm (**b**) (Crimson fluorescent microspheres, Invitrogen, Carlsbad, California, USA), excitation at 635 nm and STED at 775 nm using synchronized 20 MHz pulses, lens semiaperture angle $\alpha = 74°$, refractive index $n = 1.52$. Scale bars: 250 nm. Panels 1, 2 and 4 in **a** are reproduced with permission from ref. 48. © 2009 ACS. Part of **b** is reproduced with permission from ref. 49. © 2009 ACS.

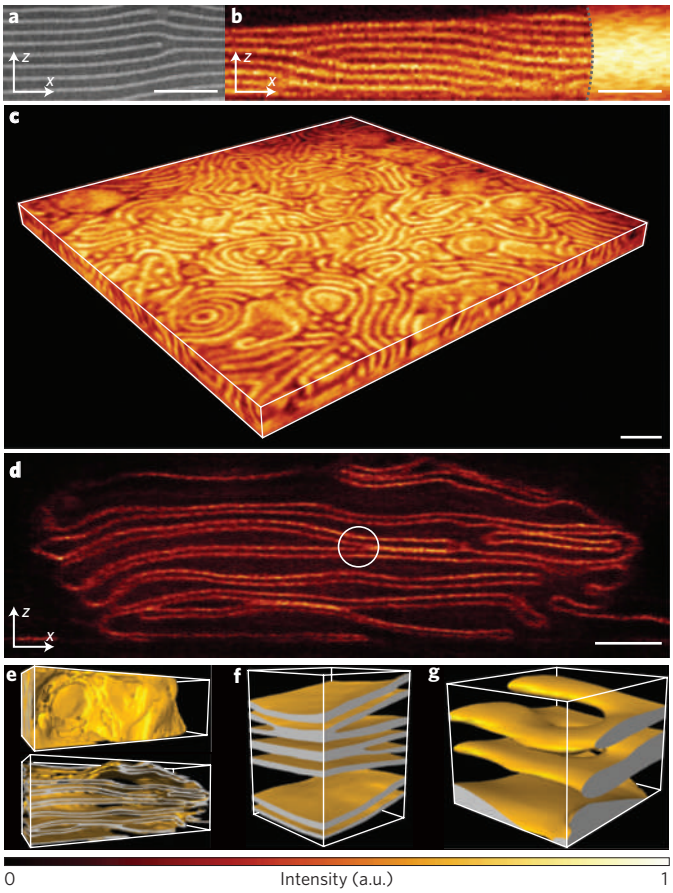


**Figure 3 | STED microscopy provides *in situ* access to 3D morphological information of nanostructured block copolymers.** **a**, TEM image confirming the lamellar morphology of a polystyrene-block-poly(2-vinylpyridine) polymer. **b**, Whereas the confocal reference (right) provides no details, scanning with an oblate STED-4Pi-PSF (left) faithfully reveals the observed nanostructure. **c**, More isotropic morphologies, such as the bicontinuous structure shown, are revealed by means of a spherical isoSTED PSF. **d**, Cross-sectional image of a mesoporous morphology induced by selectively swelling the vinyl-pyridine phase, subsequent to quaternization. The unzipped layers lining the pores (circled) are on average over half the size of the intact ones. **e**, Perspective views of the corresponding binarized data stack. **f**, Close-up of a selected area showing unzipping of the swollen domains, which line the pores. **g**, Visualization of a helicoidal screw dislocation. Scale bars: 500 nm (**a**–**c**) and 1 μm (**d**). Images **a**, **b** and **d**–**g** are reproduced with permission ref. 48. © 2009 ACS.

copy[45], operates with focal intensity distributions $I_{STED}(\mathbf{r})$ featuring a spherical hole at the centre, thus enabling 'diffraction-unlimited' isotropic resolution in three dimensions, with $\Delta\rho = \Delta z \to 0$ (Fig. 1).

In 4Pi microscopy of type B and C[22,28] and in I$^5$M[25,26], the coherent detection of the spherical wavefronts of photon emission results in an approximately fourfold faster change in phase difference in the photon self-interference at a common detector, when the emitter is changing its position along the optic axis. As a result, the axial FWHM of the main maximum of the detection PSF $h_{em}(\mathbf{r})$ decreases by approximately fourfold. When localizing the axial position of individual emitters, the narrower main maxima produced with a 4Pi system improve the axial localization by the same factor[46]. However, when the fluorophores fall into the adjacent interference minima, they are not detected. One remedy is to scan the narrower 4Pi PSF along the $z$ axis while keeping the phase difference constant[47]. Another elegant solution is to measure the phase difference directly by phase-shift interferometry, as in the method called interferometric single-molecule switching[43], or interferometric PALM (iPALM)[44] (Fig. 1).

A unique benefit of a targeted mode such as STED is that it allows shaping of the PSF $H(\mathbf{r})$ through the parameters $\beta^{\rho}I_m^{\rho}$ and $\beta^{z}I_m^{z}$, whereby almost arbitrary combinations of $\Delta\rho$ and $\Delta z$ can be attained. The overview in Fig. 2a compares the effective PSF $H(\mathbf{r})$ of a standard confocal fluorescence microscope with those PSFs that have so far been rendered by STED: the oblate PSF of a STED-4Pi scheme[12] that also applies coherent dual-lens illumination to avoid axial sidelobes, the prolate PSF of a single-lens confocalized STED microscope using a cylindrical doughnut $I_{STED}(\mathbf{r})$ (ref. 16), and the isotropic PSF generated with a dual-lens isoSTED scheme[45], recorded with the same setup and a fixed set of lenses ($\alpha = 74°$), fluorophores and wavelengths. The PSF exemplified in Fig. 2b displays an axial FWHM of $\Delta z = 30$ nm and $\Delta\rho = 21$ nm in the lateral direction. The reduction in PSF extent from the confocal reference to isoSTED by 10-fold in the focal plane and 15-fold along the $z$-axis highlights the recent progress in improving 3D resolution all-optically — that is, just by exploiting suitable optical transitions between molecular states. Although a volume larger than the confocal PSF is exposed to excitation photons, the dye is only able to reside in the excited state in the volume of the isoSTED PSF, represented by $H(\mathbf{r})$, which is 1,500 times smaller than that of the confocal PSF; in the remaining part, its ability to fluoresce is turned off by the STED beam. We

note that the resolution in an image can be further augmented by deconvolution, which also benefits from the doubled number of detected photons.

This engineering of the PSF shape enables the adaptation of $\Delta\rho$ and $\Delta z$ and, hence, of the resolution and signal strength to the structure being imaged[48]. This is exemplified by fluorescence images (Fig. 3) of the self-assembled nanopattern formed by a di-block copolymer, in which one of the polymer phases is selectively labelled with an organic fluorophore. Imaging such nanostructures in three dimensions, for example the morphology shown in Fig. 3a, usually involves invasive forms of electron or scanning probe microscopy. In contrast, the oblate PSF of the refined STED-4Pi arrangement renders the lamellar nanostructure non-invasively (Fig. 3b). Block copolymer patterns without directional preferences (Fig. 3c) are best imaged with an isotropic PSF, here of $\Delta\rho$, $\Delta z$ < 50 nm. The technique facilitates the 3D *in situ* imaging of copolymer structures that would be difficult to image by established techniques. The massive gain in detail over confocal imaging proves that isoSTED and STED-4Pi nanoscopy are powerful non-invasive methodologies for 3D imaging of polymers at the nanoscale[48].

The emerging importance of dual-lens fluorescence nanoscopy for the life sciences is exemplified in Fig. 4. All we know about the inner architecture of mitochondria, the powerhouses of the cell, is from electron microscopy, which in the 1970s revealed them as tubules of 200–400 nm diameter, formed by an inner and an outer membrane[2]. By virtue of its isotropic 3D resolution of < 50 nm, isoSTED microscopy has recently mapped out the distribution of the protein Tom20 residing in the outer mitochondrial membrane[45,49], clearly delineating its 'hollow' tubular shape (Fig. 4c). The Tom complexes represent the sites where cellular proteins enter the mitochondria. Until recently[49], electron microscopy has also been required to image the highly convoluted inner membrane that harbours the $F_1F_0$ATPase molecules pivotal to energy generation and folds into so-called cristae[2]. By scanning an ~30-nm-diameter isoSTED PSF directly through the equatorial plane of a mitochondrion in a whole fixed cell and recording immuno-labelled $F_1F_0$ATPase, the cristae were disclosed noninvasively (Fig. 4d,e) (ref. 49). The optical visualization of these central structural elements of mitochondria highlights the emerging ability of far-field fluorescence nanoscopy, and STED microscopy in particular, to image the substructure of organelles and eventually their 3D dynamics in living cells.

## Stochastic switching with opposing lens detection: iPALM

In interferometric single-molecule switching or iPALM[44], axial super-resolution is gained by recombining the fluorescence wavefronts by a set of preferably three to four splitters re-dividing the two emission wavefronts, such that partial wavefronts with fixed but different equidistant phase differences, $\phi$, are created. The interference patterns rendered by individual emitters on a camera are mathematically represented by magnified lateral cross-sections of 4Pi-detection PSFs[22], which are calculated by adding the spherical fluorescence wave fields considering the specific $\phi$ (ref. 43). They exhibit maxima and minima that are narrower and steeper by approximately fourfold compared with the main maximum of a single lens, and improve the localization in the $z$ axis accordingly. The use of three to four detection PSFs with different but fixed $\phi$ elegantly avoids ambiguities and blind spots (produced by the minima at a given $\phi$) and reduces the calculation of the $z$ position to the calculation of the ratio of the signal of the three to four detection channels.

This scheme works well along a $z$-slice thickness of $\sim\lambda/2n$ on the $z$ axis. The cross-sections of the 4Pi PSF recorded on the cameras are summed to localize the emitter laterally or analysed for a refined 3D localization. The doubling of the number $m$ of detected photons augments the localization precision ideally by $\sqrt{2}$-fold in all directions[43,44]. By localizing the same single source with $m \approx 1{,}200$ photons, iPALM experiments showed the possibility of attaining a resolving power of <22 nm and <9 nm (FWHM) in the focal plane and along the optic axis, respectively. A clear advantage of improving the PALM/STORM 3D resolution with dual lenses over the earlier single-lens approaches, which rely on introducing asymmetries in the detection PSF, is that the lateral PSF width is not widened; the 4Pi detection PSF has virtually the same lateral cross-section as that of a single-lens epifluorescence microscope[22]. Hence, the localization in the focal plane is not compromised and the number of active (state A) molecules per area or volume need not be reduced.

The potential of iPALM to visualize biomolecules in three dimensions at nanometric resolution is exemplified in Fig. 5, which shows

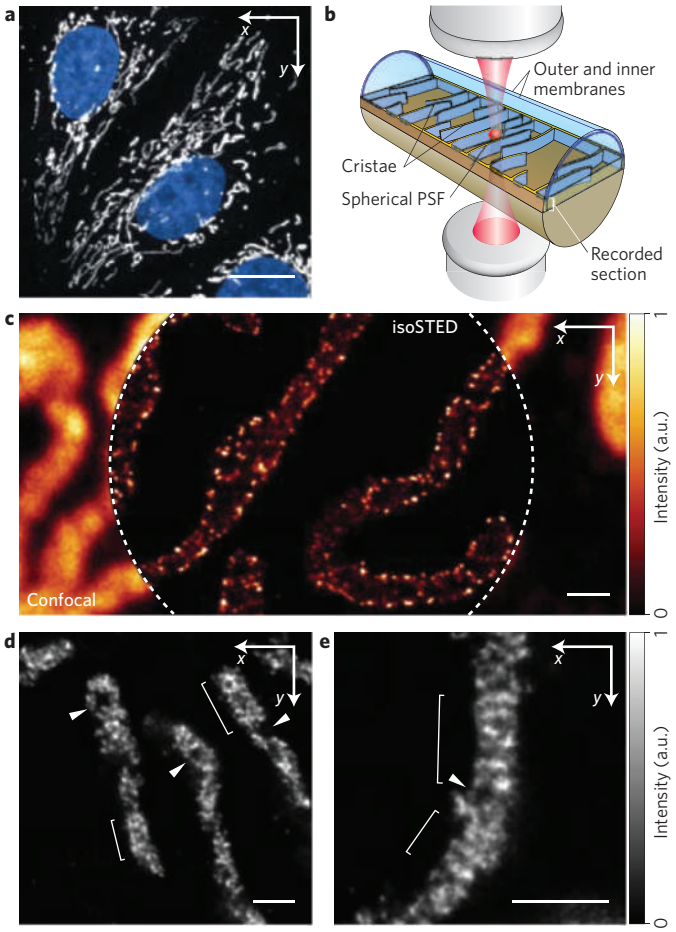


**Figure 4 | Noninvasive 3D far-field fluorescence nanoscopy of the interior of mitochondria within integral cells. a**, Confocal microscopy overview of a mammalian (PtK2) cell outlining the mitochondrial network (grey) and the nucleus (blue). **b**, Sketch of isoSTED nanoscope optically dissecting the interior of a mitochondrion with a nanospherical effective PSF. **c**, isoSTED nanoscopy resolves and correctly identifies Tom20 (translocase of the outer mitochondrial membrane) protein complexes at the outer mitochondrial membrane, whereas confocal microscopy fails to provide any positional information. The complexes represent the sites where cellular proteins enter the mitochondria. **d**,**e**, isoSTED images recorded at the mitochondrial equatorial plane reveal immunolabelled $F_1F_0$ATPase proteins of the inner mitochondrial membrane and the cristae as essential structural elements of this organelle. The brackets indicate regions in which the cristae are perpendicularly oriented to the organelle axis, whereas the arrowheads point to inner mitochondrial regions devoid of cristae. Scale bars: 10 μm (**a**) and 500 nm (**c**–**e**). Images **d**,**e** are reproduced with permission from ref. 49. © 2009 ACS.

NATURE PHOTONICS DOI: 10.1038/NPHOTON.2009.112

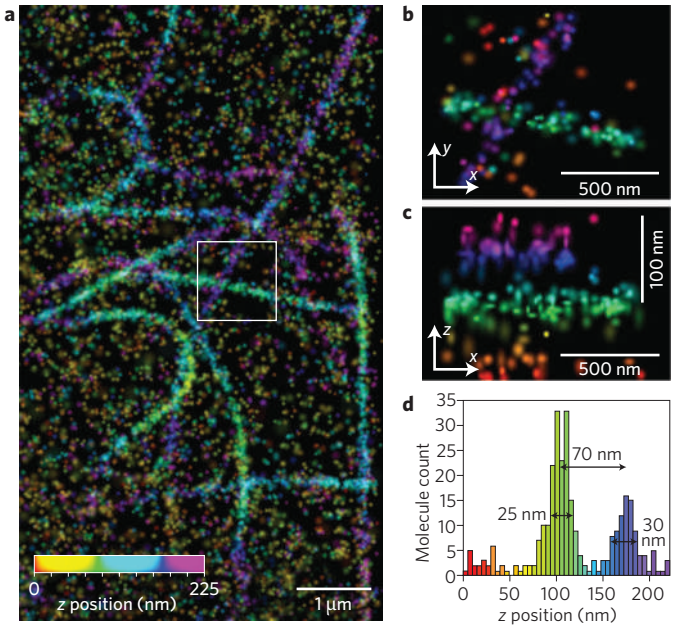


**Figure 5 | 3D fluorescence nanoscopy with interferometric PALM.** Microtubules in a mammalian (PtK1) cell expressing human $\alpha$-tubulin fused to a monomeric variant of the photoactivatable fluorescent protein KikGR. The visualization of the obtained axial resolution is enhanced by colour coding the image data depending on the position of the registered fluorophores in the *z* direction. **a**, Large area overview. **b**, **c**, Magnified view of the area bound by the white box as *xy* (**b**) and *xz* (**c**) projections (*z* scale is magnified ×5). **d**, Histogram of *z* positions of individually switched molecules in the boxed region. Each microtubule has a measured FWHM of 30 nm, which is in accordance with the expectations from electron microscopy (25 nm plus label). Microtubules only 70 nm apart along the *z* axis are separated by a pronounced dip, thus proving the resolving power provided by coherently detecting the fluorescence of individually switched fluorophores through opposing lenses. Reproduced with permission from ref. 44. © 2009 PNAS.

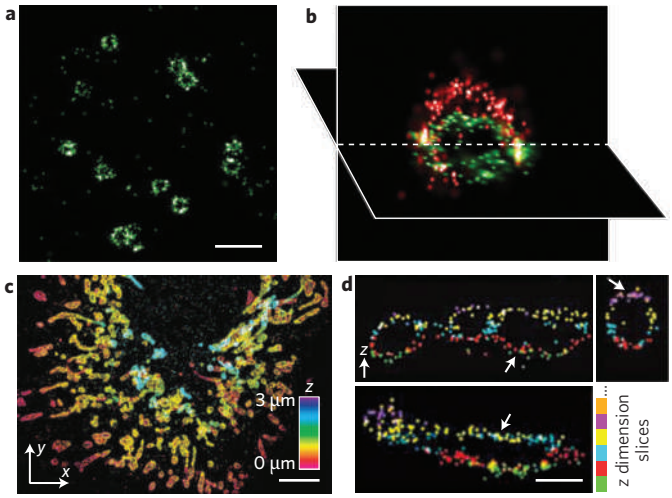


**Figure 6 | 3D far-field fluorescence nanoscopy by STORM within mammalian (BS-C-1) cells. a**, An *xy* image cross-section (50 nm thick in *z*) of clathrin in a region of a cell, showing the ring-like structure of the periphery of the clathrin-coated pits at the plasma membrane. **b**, An *xy* and *xz* cross-section presented in 3D perspective, showing the half-spherical cage-like structure of a clathrin pit. **c**, 3D image of the mitochondrial network, immuno-stained against the protein Tom20. The colour code indicates the position along the *z* axis according to the colour scale bar. **d**, Vertical cross-sections of several regions in panel **c**, colour-coded by the *z* coordinate of the *xy* slices at which they were recorded. Arrows indicate horizontal segments of mitochondria appearing in adjacent slices along the *z* axis; localizations from different slices are coloured differently. Scale bars: 500 nm (**a**), 5 µm (**c**), 750 nm (**d**). Panels from refs. 51,52. Images **a**,**b** and **c**,**d** are reproduced with permission from, respectively, ref. 51. © 2009 AAAS; and ref. 52. © 2009 NPG.

that microtubules at an axial distance of ~70 nm are readily discerned[44]. The method iPALM has also been able to resolve the dorsal and ventral plasma membranes and to visualize the arrangement of integrin receptors within the endoplasmic reticulum[44], which have so far required electron microscopy. Although current implementations are limited to resolving structures thinner than $\sim\lambda/2n$, this restriction should be alleviated in the future. As a targeted modality in which the probing volume given by $\Delta\rho$ and $\Delta z$ can be directed to any part of the sample, isoSTED microscopy does not entail conceptual restrictions with regard to sample thickness. However, practical limitations of both targeted and stochastic approaches are posed by the free working distance of the lenses of ~200 µm and the (spherical) aberrations induced by the sample. Modern developments in active and adaptive optics should help advance both 3D nanoscopy methods using opposing lenses.

## Comparison with other 3D nanoscopy schemes and outlook

We note that increasing the 3D far-field optical nanoscopy resolution is possible with single-lens schemes as well as with dual lenses, both in STED microscopy[11,50] and in PALM/STORM[34,39,51,52]. This stems from the fact that the resolution of both concepts is not limited by diffraction in any direction, but mainly determined by the $I/I_s$, or $m$ implemented. For example, in STORM a remarkable lateral and axial resolution combination of 20–30 nm and 50–60 nm, respectively, has been demonstrated by encoding the *z* axis through astigmatism[51,52]. STORM 3D recordings (Fig. 6) of the clathrin-coated pits at the plasma membrane of a mammalian cell impressively revealed their spherical cage-like structure. Likewise, 3D STORM images of the mitochondrial network, immuno-stained against the protein Tom20 in a mammalian cell, rendered the hollow structure of mitochondria. Defocus has also been effectively used for axial localization[35]. Similarly impressive resolution in the lateral and axial direction together with a larger depth of field has been shown by implementing a double-helix PSF[39].

Clearly, these advances in single-lens 3D diffraction-unlimited nanoscopy remain highly important, because adding a second lens also adds complexity to the system. Furthermore, using opposing lenses will be possible only for transparent objects that are typically thinner than 200 µm and accessible from two sides, such that the refractive index of the immersion system is adequately matched to that of the sample. Nonetheless, when applying the same $I/I_s$ or detecting the same $m$, having two opposing lenses always improves the 3D resolution further and concomitantly renders an isotropic nanoscale resolution at the highest possible level. It should be noted that irrespective of the brightness of the fluorescence marker or the specific set-up used, in single-molecule switching schemes such as PALM and STORM, combining the aperture of two opposing lenses for detection is expected to bring about a resolution gain of 1.4-fold in the focal plane and sixfold in the axial direction[43].

The exploitation of opposing lenses will also benefit from the ample experience gained in the last two decades with 4Pi microscopy and I$^5$M or I$^5$S. The application of these methods has shown that the benefits brought about by using two opposing lenses outweigh the additional complexity in many cases[24–26,28], a notion that is corroborated by the progress reported herein. In fact, compact

beam-scanning 4Pi microscopes with small modifications allow coherent dual-lens fluorescence excitation and collection, both in a point-scanning and in a widefield fashion, and have been commercially available since 2004 (ref. 29). Finally we note that, as isoSTED and iPALM are just representatives of two complementary nanoscopy modalities relying on fluorescence switching, one can expect other molecular switching mechanisms to benefit in much the same way from the coherent use of opposing lenses. For all these reasons, we expect dual-lens schemes to become central to 3D far-field optical imaging at the nanoscale in the near future.

## References


1. Born, M. & Wolf, E. *Principles of Optics* 7th edn (Cambridge University Press, 2002).
2. Alberts, B. *et al. Molecular Biology of the Cell* 4th edn (Garland Science, 2002).
3. Pohl, D. W., Denk, W. & Lanz, M. Optical stethoscopy: Image recording with resolution λ/20. *Appl. Phys. Lett.* **44,** 651–653 (1984).
4. Lewis, A., Isaacson, M., Harootunian, A. & Murray, A. Development of a 500 A resolution light microscope. *Ultramicroscopy* **13,** 227–231 (1984).
5. Novotny, L. & Hecht, B. *Principles of nano-optics* (Cambridge University Press, 2006).
6. Inouye, Y., Verma, P. & Kawata, S. Plasmonics for near-field nano-imaging and superlensing. *Nature Photon.* **3,** 388–394 (2009).
7. Pendry, J. B. Negative refraction makes a perfect lens. *Phys. Rev. Lett.* **85,** 3966–3969 (2000).
8. Hell, S. W. & Wichmann, J. Breaking the diffraction resolution limit by stimulated emission: stimulated emission depletion fluorescence microscopy. *Opt. Lett.* **19,** 780–782 (1994).
9. Hell, S. W. & Kroug, M. Ground-state depletion fluorescence microscopy, a concept for breaking the diffraction resolution limit. *Appl. Phys. B* **60,** 495–497 (1995).
10. Hell, S. W. in *Topics in Fluorescence Spectroscopy* Vol. 5 (ed. J. R. Lakowicz) 361–422 (Plenum Press, 1997).
11. Klar, T. A., Jakobs, S., Dyba, M., Egner, A. & Hell, S. W. Fluorescence microscopy with diffraction resolution limit broken by stimulated emission. *Proc. Natl Acad. Sci. USA* **97,** 8206–8210 (2000).
12. Dyba, M. & Hell, S. W. Focal spots of size λ/23 open up far-field fluorescence microscopy at 33 nm axial resolution. *Phys. Rev. Lett.* **88,** 163901 (2002).
13. Hell, S. W. Toward fluorescence nanoscopy. *Nature Biotechnol.* **21,** 1347–1355 (2003).
14. Heintzmann, R., Jovin, T. M. & Cremer, C. Saturated patterned excitation microscopy — A concept for optical resolution improvement. *J. Opt. Soc. Am. A* **19,** 1599–1609 (2002).
15. Gustafsson, M. G. L. Nonlinear structured-illumination microscopy: Wide-field fluorescence imaging with theoretically unlimited resolution. *Proc. Natl Acad. Sci. USA* **102,** 13081–13086 (2005).
16. Willig, K. I., Rizzoli, S. O., Westphal, V., Jahn, R. & Hell, S. W. STED-microscopy reveals that synaptotagmin remains clustered after synaptic vesicle exocytosis. *Nature* **440,** 935–939 (2006).
17. Betzig, E. *et al.* Imaging intracellular fluorescent proteins at nanometer resolution. *Science* **313,** 1642–1645 (2006).
18. Rust, M. J., Bates, M. & Zhuang, X. Sub-diffraction-limit imaging by stochastic optical reconstruction microscopy (STORM). *Nature Meth.* **3,** 793–796 (2006).
19. Hess, S. T., Girirajan, T. P. K. & Mason, M. D. Ultra-high resolution imaging by fluorescence photoactivation localization microscopy. *Biophys. J.* **91,** 4258–4272 (2006).
20. Egner, A. *et al.* Fluorescence nanoscopy in whole cells by asnychronous localization of photoswitching emitters. *Biophys. J.* **93,** 3285–3290 (2007).
21. Hell, S. W. Double-scanning confocal microscope. European patent 0491289 (1990/1992).
22. Hell, S. & Stelzer, E. H. K. Properties of a 4Pi-confocal fluorescence microscope. *J. Opt. Soc. Am. A* **9,** 2159–2166 (1992).
23. Gustafsson, M. G. L., Agard, D. A. & Sedat, J. W. Sevenfold improvement of axial resolution in 3D widefield microscopy using two objective lenses. *Proc. SPIE* **2412,** 147–156 (1995).
24. Hell, S. W., Schrader, M. & van der Voort, H. T. M. Far-field fluorescence microscopy with three-dimensional resolution in the 100 nm range. *J. Microsc.* **185,** 1–5 (1997).
25. Gustafsson, M. G. L., Agard, D. A. & Sedat, J. W. $I^5M$: 3D widefield light microscopy with better than 100 nm axial resolution. *J. Microsc.* **195,** 10–16 (1999).
26. Shao, L. *et al.* I5S: Wide-field light microscopy with 100 nm scale resolution in three dimensions. *Biophys. J.* **94,** 4971–4983 (2008).
27. Hell, S. W. Far-field optical nanoscopy. *Science* **316,** 1153–1158 (2007).
28. Gugel, H. *et al.* Cooperative 4Pi excitation and detection yields 7-fold sharper optical sections in live cell microscopy. *Biophys. J.* **87,** 4146–4152 (2004).
29. Bewersdorf, J., Bennett, B. T. & Knight, K. L. H2AX chromatin structures and their response to DNA damage revealed by 4Pi microscopy. *Proc. Natl Acad. Sci. USA* **103,** 18137–18142 (2006).
30. Gustafsson, M. G. L. & Clarke, J. Scanning force microscope springs optimized for optical-beam deflection and with tips made by controlled fracture. *J. Appl. Phys.* **76,** 172–181 (1994).
31. Hofmann, M., Eggeling, C., Jakobs, S. & Hell, S. W. Breaking the diffraction barrier in fluorescence microscopy at low light intensities by using reversibly photoswitchable proteins. *Proc. Natl Acad. Sci. USA* **102,** 17565–17569 (2005).
32. Sharonov, A. & Hochstrasser, R. M. Wide-field subdiffraction imaging by accumulated binding of diffusing probes. *Proc. Natl Acad. Sci. USA* **103,** 18911–18916 (2006).
33. Shroff, H. *et al.* Dual-color superresolution imaging of genetically expressed probes within individual adhesion complexes. *Proc. Natl Acad. Sci. USA* **104,** 20308–20313 (2007).
34. Juette, M. F. *et al.* Three-dimensional sub-100 nm resolution fluorescence microscopy of thick samples. *Nature Meth.* **5,** 527–529 (2008).
35. Bates, M., Huang, B., Dempsey, G. P. & Zhuang, X. Multicolor super-resolution imaging with photo-switchable fluorescent probes. *Science* **317,** 1749–1753 (2007).
36. Zhuang, X. Nano-imaging with STORM. *Nature Photon.* **3,** 365–367 (2009).
37. Rittweger, E., Wildanger, D. & Hell, S. W. Far-field fluorescence nanoscopy of diamond color centers by ground state depletion. *Europhys. Lett.* **86,** 14001–14006 (2009).
38. Biteen, J. S. *et al.* Super-resolution imaging in live caulobacter crescentus cells using photoswitchable EYFP. *Nature Meth.* **5,** 947–949 (2008).
39. Pavani, S. R. P. *et al.* Three-dimensional, single-molecule fluorescence imaging beyond the diffraction limit by using a double-helix point spread function. *Proc. Natl Acad. Sci. USA* **106,** 2995–2999 (2009).
40. van de Linde, S., Kasper, R., Heilemann, M. & Sauer, M. Photoswitching microscopy with standard fluorophores. *Appl. Phys. B* **93,** 725–731 (2008).
41. Heilemann, M. *et al.* Subdiffraction-resolution fluorescence imaging with conventional fluorescent probes. *Angew. Chem. Int. Ed.* **47,** 6172–6176 (2008).
42. Dyba, M., Jakobs, S. & Hell, S. W. Immunofluorescence stimulated emission depletion microscopy. *Nature Biotechnol.* **21,** 1303–1304 (2003).
43. Middendorff, C.v., Egner, A., Geisler, C., Hell, S. W. & Schönle, A. Isotropic 3D nanoscopy based on single emitter switching. *Opt. Express* **16,** 20774–20788 (2008).
44. Shtengel, G. *et al.* Interferometric fluorescent super-resolution microscopy resolves 3D cellular ultrastructure. *Proc. Natl Acad. Sci. USA* **106,** 3125–3130 (2009).
45. Schmidt, R. *et al.* Spherical nanosized focal spot unravels the interior of cells. *Nature Meth.* **5,** 539–544 (2008).
46. Lemmer, P. *et al.* SPDM — Light microscopy with single molecule resolution at the nanoscale. *Appl. Phys. B* **93,** 1–12 (2008).
47. Egner, A., Schrader, M. & Hell, S. W. Refractive index mismatch induced intensity and phase variations in fluorescence confocal, multiphoton and 4Pi-microscopy. *Opt. Commun.* **153,** 211–217 (1998).
48. Ullal, C. K., Schmidt, R., Hell, S. W. & Egner, A. Block copolymer nanostructures mapped by far-field optics. *Nano Lett.* **9,** 2497–2500 (2009).
49. Schmidt, R. *et al.* Mitochondrial cristae revealed with focused light. *Nano Lett.* **9,** 2508–2510 (2009).
50. Harke, B., Ullal, C. K., Keller, J. & Hell, S. W. Three-dimensional nanoscopy of colloidal crystals. *Nano Lett.* **8,** 1309–1313 (2008).
51. Huang, B., Wang, W., Bates, M. & Zhuang, X. Three-dimensional super-resolution imaging by stochastic optical reconstruction microscopy. *Science* **319,** 810–813 (2008).
52. Huang, B., Jones, S. A., Brandenburg, B. & Zhuang, X. Whole-cell 3D STORM reveals interactions between cellular structures with nanometer-scale resolution. *Nature Meth.* **5,** 1047–1052 (2008).


## Acknowledgements

Substantial contributions to the isoSTED imaging applications reviewed in this paper are from Chaitanya Ullal (block co-polymers), as well as Christian Wurm and Stefan Jakobs (mitochondria). We also thank Andreas Schönle, Claas v. Middendorf, and Jan Keller for helpful discussions and Jaydev Jethwa for critical reading. This work was supported by grants of the Deutsche Forschungsgemeinschaft to A.E. and S.W.H (SFB 755).

## Additional information

Details accompany the full-text HTML version of the paper at www.nature.com/naturephotonics. Reprints and permission information is available online at http://npg.nature.com/reprintsandpermissions/. Correspondence and requests for materials should be addressed to S.W.H.

REVIEW ARTICLE | FOCUS
PUBLISHED ONLINE: 29 JUNE 2009 | DOI: 10.1038/NPHOTON.2009.111
nature photonics

# Plasmonics for near-field nano-imaging and superlensing

Satoshi Kawata[1,2], Yasushi Inouye[3] and Prabhat Verma[1,3]

**Diffraction of light prevents optical microscopes from having spatial resolution beyond a value comparable to the wavelength of the probing light. This essentially means that visible light cannot image nanomaterials. Here we review the mechanism for going beyond this diffraction limit and discuss how manipulation of light by means of surface plasmons propagating along the metal surface can help to achieve this. The interesting behaviour of light under the influence of plasmons not only allows superlensing, in which perfect imaging is possible through a flat thin metal film, but can also provide nano-imaging of practical samples by using a localized surface plasmon mode at the tip of a metallic nanoprobe. We also discuss the current research status and some intriguing future possibilities.**

Scientists have long dreamt of an optical microscope that can be used to see a sample in nanometre resolution. Because light propagates through water and air, an optical microscope can be used to see, *in vivo*, the details of living matter and other materials in their unperturbed natural condition. In addition, an optical microscope provides colour images that contain much richer information than other microscopes in which only monochrome images are produced. In particular, the visible and mid-infrared region of light covers the energies corresponding to the electronic transitions in atoms and to molecular vibrations, allowing optical microscopes to provide information related to the intrinsic properties of the sample. But the resolution attainable with an optical microscope is limited to about 0.5 μm because of the diffraction of light[1–3]. Therefore, it becomes almost impossible to image a sample at the nanoscale through an optical microscope.

Breaking through this limit, an optical microscope was proposed in which a nano-sized metallic probe tip scans the sample surface to form an image with a resolution much better than the diffraction limit[4]. The mechanism is based on the excitation of localized modes of surface plasmon polaritons (SPP) at the metallic tip, which generates a nano-sized spot of light at the apex of the nano-tip. By using this tiny light-spot as the light source of an optical microscope, extremely high spatial resolution can be obtained. The fundamental idea of exciting SPP to obtain images beyond the diffraction limit of light has been used in other studies as well. For example, the perfect lens or superlens proposed by Pendry also images a sample in nanoscopic resolution by exciting SPP at its resonance frequency[5,6]. Here we review the mechanism of optical nano-imaging based on the excitation of SPP to provide spatial resolution beyond the diffraction limit. We discuss a variety of metallic nanostructures as probes and look at their applications.

## Super-resolution imaging by slow light

According to Abbe's diffraction theory, the minimum separation $\Delta x$ of two points that can be resolved in an image constructed through a lens based on Rayleigh's criterion is given by

$$\Delta x = \frac{0.61\lambda}{n \sin\theta} \qquad (1)$$

where $\lambda$ is the wavelength of light, $n$ is the refractive index of the medium, and $2\theta$ is the angular aperture of the lens on the object side[7]. Here, the angular aperture and the refractive index are both physically limited. Thus the wavelength $\lambda$ is the only parameter that can be manipulated to obtain a desired value of the spatial resolution. To obtain super-resolution, we need to shorten the wavelength. But at the same time, to stay in the visible or infrared region in order to image the intrinsic properties of a sample as shown by its electronic or vibrational energies, we must not change the frequency or the energy of the light.

The wavelength of light is inversely proportional to the angular frequency, $\omega$, as $\lambda = 2\pi c/\omega$, where $c$ is the speed of light. If one can reduce the speed of light while keeping the frequency constant, the wavelength of light can be shortened and hence a higher resolution obtained in an image. Classically, this has been done by filling the space between the lens and sample surface with some high-refractive-index material such as immersion oil. This method improves the resolution within the limits of available refractive indices (less than 2). In some cases, it is possible to increase the refractive index further, but then it is difficult to keep the medium transparent in the visible regime. For substantial improvement in spatial resolution, we need a different method for reducing the speed of light.

There exists a form of slow light on the surface of a metal that travels along the surface as an evanescent wave associated with the collective oscillations of free electrons. In quantum form, this is called the surface plasmon polariton, and we can take advantage of this for high-resolution imaging. Figure 1a shows a typical plot for the dispersion curves of SPP and light. The dispersion for the light shows a linear relationship between frequency (energy) and wavenumber (momentum) whereas the dispersion for the SPP shows a curve. As the frequency approaches the resonance of SPP, the SPP dispersion curve moves away from the light line with a gentle slope. That means that the wavelength of SPP is shortened and the speed decreases. The light line and the SPP line never cross each other, and hence there is a phase mismatch for all values of the frequency. This prevents any coupling between propagating light and SPP[8–12]. Note that above the plasmon frequencies, the metal becomes dielectric, and for lower frequencies in the terahertz region, plasmonic effects disappear. But if the light is slow, as is the case for evanescent light near the surface of a metal, the dispersion for light has a different angle, as illustrated in Fig. 1a, and hence it crosses the SPP line at a certain frequency. This essentially means that there can be a coupling between the evanescent light and SPP at this particular frequency, resulting in resonant excitation of SPP.

The use of SPP on a gold thin film for subwavelength imaging was demonstrated by Smolyaninov *et al.*, who used a 502-nm line of an argon-ion laser to excite the SPP[8]. The authors put a small droplet of glycerin on a gold film, the parabolic boundary of which worked

[1]Department of Applied Physics, Osaka University, Suita 565-0871, Osaka, Japan. [2]RIKEN, Wako, Saitama 351-0198, Japan. [3]Graduate School of Frontier Biosciences, Osaka University, Suita 565-0871, Osaka, Japan. e-mail: kawata@ap.eng.osaka-u.ac.jp; verma@ap.eng.osaka-u.ac.jp

as a magnifying mirror in two dimensions (2D). A sample was set on the gold film under the glycerin droplet, and a magnified image formed by the glycerin droplet was observed through an ordinary microscope, as illustrated in Fig. 1b. Periodic nanohole arrays are ideal test samples in this demonstration, because when they are illuminated by laser light, they produce propagating surface waves, explaining the anomalous transmission of such an array at optical frequencies. The authors therefore selected a suitably designed periodic nanohole array as the sample. The SPP wavelength of gold excited by light at 502 nm corresponds to ~70 nm, resulting in resolution enhancement by a factor of ~7. This demonstration can be considered as a kind of plasmon microscope in 2D. Near-field light cannot be detected in the far field, so such a microscope must include a mechanism that can convert the near field into far field. Roughness, protrusion or periodic corrugation on the metal surface can do this job by coupling SPP out to the far field[9–12].

## Superlens as an extreme case

In the extreme case, as the angular frequency $\omega$ approaches the resonance frequency $\omega_{sp}$, the wavenumber $k_{sp}$ associated with SPP goes to infinity, which means the speed goes down to zero. This is the case of the superlens[5] which permits perfect imaging through a metal film (made from a noble metal such as gold or silver) without any blurring. In ref. 5, and in several other articles[13–17], the superlens phenomenon is primarily explained through negative refraction, but an analogous way to understand it is to consider the slowing of light at metallic surfaces.

Imaging through a superlens essentially requires both the object and the image to be within the near-field range. Therefore, it becomes impossible to read the image through a conventional optical system with a lens or a mirror. Instead, Zhang and his group recorded the near-field image on photoresist and read it by atomic force microscopy (AFM)[17]. Figure 2 explains their experiment and results. An object in the form of the word 'NANO' was imaged on a photoresist through a 35-nm-thick silver film that acted as the superlens. A resolution of about 65 nm was obtained. A superlens with magnifying function was later proposed by several authors[18–21] independently, with either a cylindrical geometry for the silver film or a tapered arrangement of silver nanorods.

A superlens has some practical limits in obtaining high resolution. In addition to questions of structural quality such as surface roughness and purity of material against oxidization and/or sulphurization, the absorption of plasmons in metal is an essential limitation. The imaginary part of the dielectric constant of a metal is not negligible, and plasmon resonance typically decays with a half-life of a few picoseconds or less. This causes loss of information and hence blurring of the image.

## Metallic tip for nano-imaging

Although a superlens can provide an image of nanostructure well beyond the diffraction limit, a large, flat metallic surface restricts the geometry of the sample for practical imaging. If the metal structure can be made much smaller than the wavelength of propagating light, one can scan such a nanostructure along the sample surface as a probe, similar to the other scanning probe microscopes[22], and image a sample with high resolution geometry. The SPP of a metallic nanoparticle is strongly localized and hence the dispersion relation is different from the one shown in Fig. 1. Unlike the SPP of a large metallic structure, the localized modes of SPP in a small metallic structure can couple with the propagating photons, which essentially means slowing down of the light or reduction in the effective wavelength close to the metallic nanostructure. The advantage of this system is that, owing to the small size of the metallic structure, there is no propagation of SPP, and hence losses related to the retardation of SPP do not exist. Any microscopy involving this confined light field will therefore have a spatial

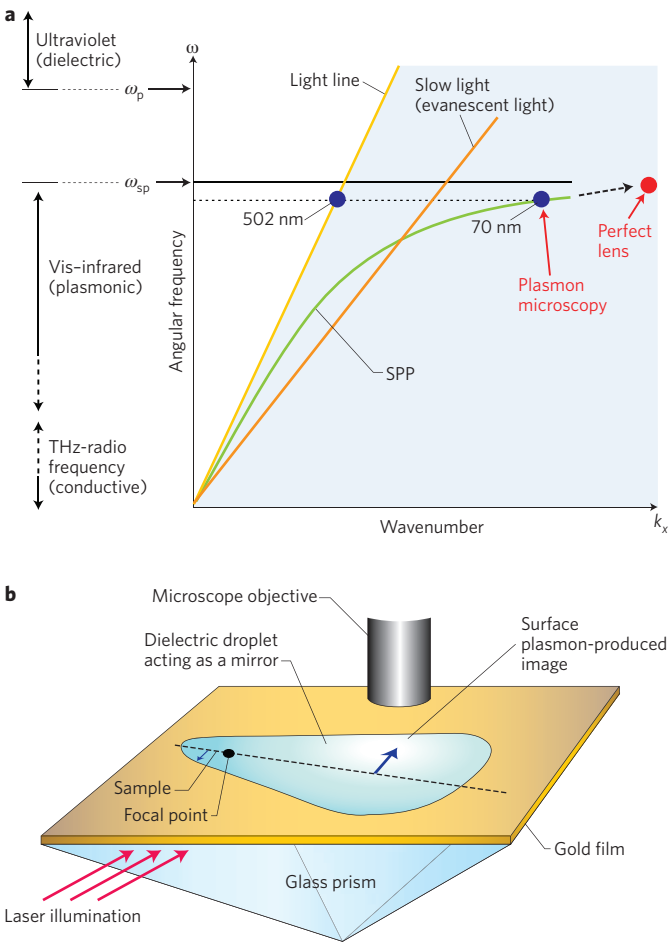


**Figure 1 | Slow light on metal surface. a**, Dispersion relation of propagating light, evanescent light and SPP. The blue circles show that propagating light with a wavelength of 502 nm can excite SPP with a wavelength of 70 nm in the plasmon microscopy demonstrated in ref. 8. The red circle indicates the ideal case of a perfect lens. **b**, Geometry of 2D plasmon microscopy. The structure on the metal surface is magnified by the parabolic boundary of a dielectric droplet that works as a mirror, and the image is detected through an ordinary objective lens. Reproduced with permission from ref. 8. © 2005 OSA.

resolution comparable to the size of the confined field, which is the same as the size of the metallic nanostructure. The metallic structure could be a nanosphere, a nanorod, a nanocone or other shape[23–25].

Figure 3 shows some examples of metallic nanoscale tips used as the probe in this imaging technique. A numerical simulation (Fig. 3a) shows the confinement of light at the apex of a tip. The tip can be scanned over a sample, as in Fig. 3b, to construct an image. Several methods for preparing metallic nano-tips have been proposed, as illustrated in Fig. 3c–e: for example, an AFM cantilever tip could be coated with a thin silver film[26], a silver or gold nanoparticle could be attached to the end of a pointed optical fibre[27,28] or a silver wire could be electrochemically etched after milling with a focused ion beam[29].

This concept was first demonstrated by Kawata's group through an apertureless near-field scanning optical microscope (NSOM) in 1994, where a metallic scanning tunnelling microscope (STM) tip, illuminated with evanescent light, was scanned over the sample[4]. Boccara and his group[30] reported the same concept in 1995 for infrared imaging, using a bent conical tungsten tip as an apertureless NSOM probe. During the same period, Wickramasinghe's group reported apertureless NSOM with a non-metallic silicon tip[31], where

NATURE PHOTONICS DOI: 10.1038/NPHOTON.2009.111

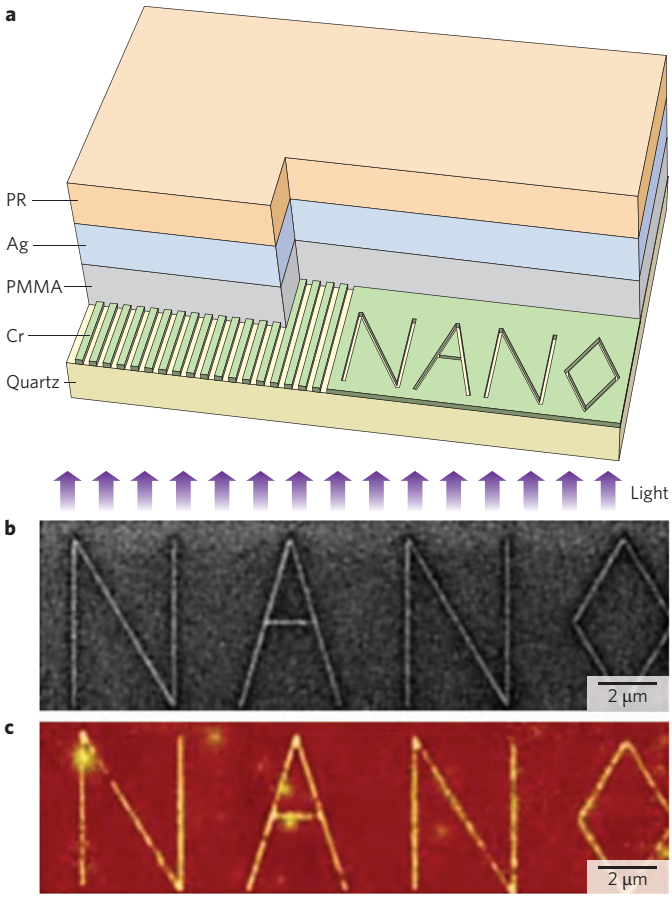


**Figure 2 | Experimental demonstration of subwavelength imaging through a thin silver layer. a**, An illustration of experimental demonstration of subwavelength imaging through a superlens. The sample, inscribed in the form of the word 'NANO' in chromium film, is separated by a thin layer of polymethyl methacrylate (PMMA) from a 35-nm-thick silver film acting as a superlens. The image is recorded on a photoresist in the form of topographic modulation. **b**, A focused ion beam (FIB) image of the inscribed object. **c**, AFM image of the topographic modulation corresponding to the near-field image obtained from the superlens. Images in **a**, **b** and **c** are reproduced with permission from ref. 17. © 2005 AAAS.

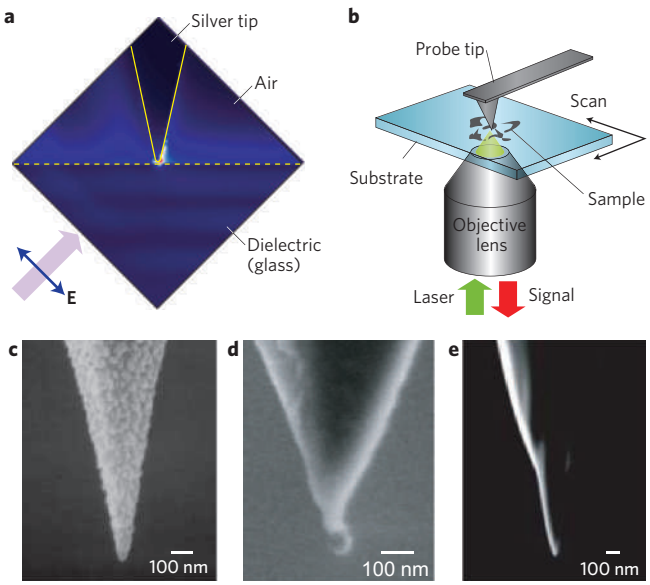


**Figure 3 | Commonly used metallic nanoprobes. a**, Numerical calculation of light distribution at the apex of a metallic nano-tip shows an enhancement of ~100 times[41]. **b**, A typical set-up for apertureless NSOM, where a nano-tip is illuminated through a thin sample and the signal is collected by the same objective lens that illuminates the tip. Image is obtained by scanning the sample stage. **c**–**e**, Scanning electron microscope images of some commonly used metallic nano-tips. **c**, Cantilever coated with silver thin film by evaporation. **d**, Gold nanoparticle attached to pointed optical fibre. **e**, Electrochemically etched silver wire. Images in **c**, **d** and **e** reproduced with permission from, respectively, ref. 26. © 2001 Elsevier; ref. 28. © 2006 APS; and ref. 29. © 2003 APS.

there were no involvements of plasmons. Rather, interferometric detection was used to measure the local refractive index for imaging. Knoll and Keilmann used interferometry for infrared imaging[32], and there have been several other reports[33] on similar research. In the infrared region, because the dispersion curve of SPP for metal approaches the light line (Fig. 1), SPP-assisted light enhancement is not expected.

In an interesting proposal for a NSOM probe, a tip was prepared by coating a metal thin film over a small protrusion on an otherwise flat surface, producing a localized field at the protrusion to sense the local dielectric constant of a sample[34]. In another study, a microscope was invented in which a gold nanoparticle trapped and controlled by a laser beam was used as an imaging probe[35]. By scanning such a trapped gold particle over the sample surface, an image of fluorescent DNA entangles was demonstrated.

In the early stage of near-field microscopy, apertured tips were used to confine the light by passing it through a tiny hole at the apex of the tip. Although this kind of NSOM has certain advantages, such as a reduction of far-field background or the potential to characterize a plasmonic device, it always suffers from comparatively low resolution that is governed by the size of the aperture.

## Enhancement of confined light

In addition to high resolution, plasmonic nano-imaging is advantageous in terms of optical throughput. The field intensity near the metallic nanostructure is highly enhanced owing to the resonance of localized SPP. The enhancement factor strongly depends on the shape and the size of the metallic nanostructure. Figure 4a illustrates some of the nanostructures commonly used for this purpose. An easy way to understand the light–metal interaction for a nanostructure is to consider the separation of free charge carriers under the influence of the external electric field associated with the propagating light. This separation creates an additional field that oscillates with the same frequency as the external field. As a result, an extremely localized and enhanced light field is created close to the metal structure, as illustrated in Fig. 4a.

As plasmons tend to radiate at curvature, a spherical shape turns out not to be the best shape for enhancement. On the other hand, the formation of standing waves of SPP in a structure with appropriate geometry provides strong resonances and hence supports stronger enhancement[36,37]. In that sense, a rod with optimized aspect ratio seems to be the best deal. Both ends of a rod can have a strongly confined field, usually known as the 'hot spot'. The other interesting structures are triangles and cones, which, owing to their sharp edges, produce strong concentration of free charge carriers at the apex, resulting in a higher field enhancement near the apex. Both triangular[38–40] and conical[41] nanostructures have been shown to produce enormous field enhancement. Many groups have also theoretically calculated the field enhancement for different shapes of metallic nanoprobes. Figure 4b shows one such numerical simulation result for a nanorod that is 150 nm long and has a diameter of 20 nm. The light source is considered as a dipole (indicated by the double-headed arrow) 10 nm from one end of the nanorod, and a hot spot is

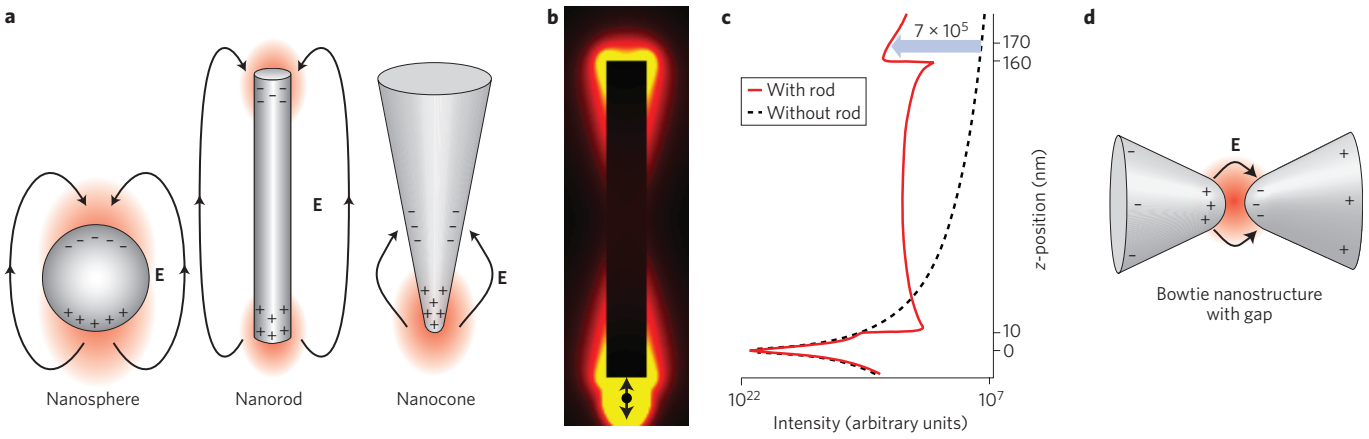


**Figure 4 | Light field enhancement at metallic nanostructures. a**, Illustration of some commonly used metallic nanostructures showing field enhancement. **b**, Simulation results showing the intensity distribution of the resonance mode of SPP along the cross-section of a 150-nm-long silver nanorod. **c**, The dashed line shows the natural decay of light intensity in the absence of the nanorod, and the red curve shows the intensity in the presence of the rod. A field enhancement of $7 \times 10^5$ can be realized. **d**, A bowtie-shaped nanostructure, which can have strong field enhancement within the nanogap.

observed at the other end. The colour distribution in Fig. 4b shows the light intensity distribution along the rod, and the red solid and black dashed curves in Fig. 4c show the intensity profiles along the length in the presence and absence of the rod, respectively. A comparison of the two curves reveals that the intensity enhancement at the end of the rod is a factor of about $10^6$. Several researchers have made use of such a hot spot at the end of a nanorod to demonstrate considerable enhancement in Raman scattering[42–44].

When the SPP of one metallic nanostructure interacts with the SPP of another close by, the field enhancement at the nanogap between the two nanostructures can be many times larger[45,46]. This is illustrated in Fig. 4d, where field enhancement between two conical nanostructures arranged in the form of a bowtie[47–50] is depicted. Several research groups have studied enhancement at the nanogap between two metallic nanostructures for different kind of structures, including the plasmonic enhancement in surface-enhanced resonance spectroscopy (SERS)[51–57], where hot spots between nanostructures play an important part.

## Tip-enhanced Raman and CARS imaging

As Raman spectroscopy provides information about molecular and lattice vibrations, one can observe the target directly without any need for staining or dye. Rich information is available from the vibrational modes, but owing to the second-order optical process involved in Raman scattering, the probability of the Raman process (typical cross-section $10^{-30}$ cm$^2$) is much smaller than that of infrared absorption (typical cross-section $10^{-20}$ cm$^2$) or fluorescence (typical cross-section $10^{-16}$ cm$^2$). Field enhancement can therefore make a useful contribution to Raman scattering, which has made SERS an important research topic, although SERS does not improve the spatial resolution. But if SERS is activated by a nanosized metallic structure instead of a large, rough metallic surface, one can achieve high resolution as well. The technique based on this phenomenon is called tip-enhanced Raman spectroscopy (TERS), where Raman scattering is combined with the NSOM technique. Between 1999 and 2000, three groups independently demonstrated the application of TERS[51,58,59]. Since then, plenty of nanomaterials have been investigated with TERS, examples being single-walled carbon nanotubes (SWNTs), fullerenes ($C_{60}$), DNA and strained silicon[29,60–68]. All these reports considered different kind of physical, chemical or even mechanical properties of samples at the nanoscale and pointed towards several interesting applications of TERS. Here we will review some of the well-known applications of plasmonic enhancement.

One of the common challenges in TERS is to achieve high spatial resolution. As an example of linear Raman scattering at high spatial resolution, we discuss the TERS imaging of SWNT reported in 2003 by Novotny's group[29]. The authors scanned a monodispersed SWNT sample at G′ Raman mode (2,615 cm$^{-1}$) to obtain a TERS image, which is shown in Fig. 5a. The spatial resolution of this image, as estimated from the line profile across the nanotubes (indicated by white dashed line), was 25 nm, which is about 25 times smaller than the wavelength of the excitation light ($\lambda$ = 633 nm), showing extremely high spatial resolution. In later years, the same group showed even better spatial resolution, at about 35 times smaller than the probing wavelength[68].

Nonlinearity gives intrinsic confinement of photons in any nonlinear spectroscopy. Consequently, the spatial resolution of nanoimaging can be improved by combining the NSOM with nonlinear optical phenomenon. This was demonstrated by combining tip enhancement with coherent anti-Stokes Raman scattering (CARS)[61]. The sample was prepared by casting a network structure of double-stranded DNA consisting of adenine and thymine base pairs and a high-resolution tip-enhanced CARS (TE-CARS) image was obtained (Fig. 5b). The spatial resolution, as estimated from the line profile along the dotted line, was about 15 nm, which is about 60 times smaller than the probing wavelength ($\lambda$ = 880 nm). This spatial resolution is almost a factor of 2 better than linear TERS. Apart from the resolution, the researchers also demonstrated, by imaging the diameter distribution in a bundle of SWNTs[69], that TERS imaging can reveal the distribution of intrinsic properties of a sample by means of coded colours.

## Fluorescence imaging

Fluorescence microscopy also benefits from the confinement and enhancement of the light at the tip apex. In the early days of near-field optical imaging, Xie's group demonstrated a near-field two-photon excited fluorescence image by using a gold nano-tip and a mode-locked Ti:sapphire laser[70]. The group produced a tip-enhanced fluorescence image of a photosynthetic membrane fragment with spatial resolution of the order of 20 nm. Later, many other researchers achieved high-resolution fluorescence measurements by using the technique of field enhancement at a metallic nanostructure[71–76]. Recently, there has been a report on single molecular detection based on a similar concept[77]. One important drawback of tip-enhanced fluorescence is that the fluorescence tends to quench at the metallic tip, when the tip comes in close contact with the sample. The measured intensity of fluorescence is therefore a trade-off

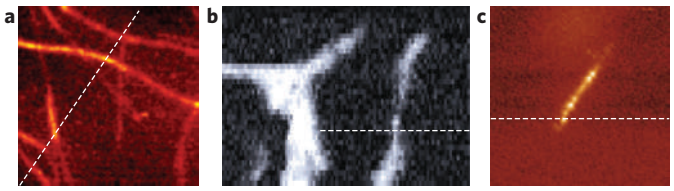


**Figure 5 | High-resolution imaging through tip-enhancement effects.** **a**, TERS image of SWNTs showing a spatial resolution of about 25 nm. **b**, TE-CARS image of a DNA network, with a spatial resolution better than 15 nm. The spatial resolution in Raman measurements can be improved by the nonlinearity in spectroscopy. **c**, Fluorescence image of an isolated SWNT, indicating a spatial resolution better than 15 nm. Images in **a**, **b** and **c** reproduced with permission from, respectively, ref. 29, © 2003 APS; ref. 61, © 2004 APS; and ref. 79, © 2005 ACS.

between quenching and enhancement[28,78]. Nevertheless, the results of fluorescence imaging through metallic tip have so far been outstanding. Figure 5c shows a tip-enhanced fluorescence image of SWNT, which is taken from the work of Novotny and his group[79]. A line profile corresponding to the dotted line in Fig. 5c determines the spatial resolution of the fluorescence image, which was found to be about 15 nm. Even though quenching is a serious obstacle, near-field fluorescence imaging has so far given us some important and interesting results. Recently, ion pump proteins bound in plasma membrane have been imaged in an aqueous environment by tip-enhanced fluorescent measurement[80,81]. Although the results of fluorescence enhancement near a metallic tip are evident, one should note that this technique suffers from bleaching over a long measurement time, particularly because the sample is illuminated over a much larger area than the actual measurement area. In contrast, similar Raman measurements do not have any bleaching.

## Single-molecule detection

Even though Raman efficiency is extremely low, several researchers have demonstrated in the past decade that plasmonic enhancement (sometimes combined with chemical enhancement) in SERS can reveal the spectroscopic signature of a single molecule. In most of the studies, silver colloids mixed with Raman active molecules are immobilized on a suitable substrate[42,57,82,83]. The concentration of the molecule is usually chosen to be very low so that statistically there is no more than one molecule per colloid, and thus any Raman signal originating from the sample can be considered to be coming from a single molecule. The other signature considered to be a characteristic of single-molecule emission is strong temporal fluctuation of these SERS signals, both in intensity and spectral shape[57,82,83]. The general consensus is that there are very few active colloids capable of producing the hot spot for single-molecule detection. Although some researchers have suggested that these hot spots could be generated near a single isolated metal nanoparticle, most other researchers have found that the hot spots are typically at the junction between two or more closely spaced nanoparticles. Such an interpretation is also supported by theoretical studies[84,85].

Kneipp *et al.* demonstrated in 1997 that by using aggregated colloidal silver they could detect single molecules of crystal violet in near-infrared experiments[56]. In the same year, Nie and Emory demonstrated wonderful single-molecule SERS observations with visible light ($\lambda$ = 514.5 nm) for rhodamine 6G molecules adsorbed on isolated silver nanoparticles[42]. Apart from Raman scattering, plasmonic enhancement was also used around the same time in other techniques, such as second harmonic generation, for field localization[86] and for the detection of single molecules[87]. Since then, many other reports have emerged on single-molecule detection through SERS[57,88–93], most of which discussed the importance of creating

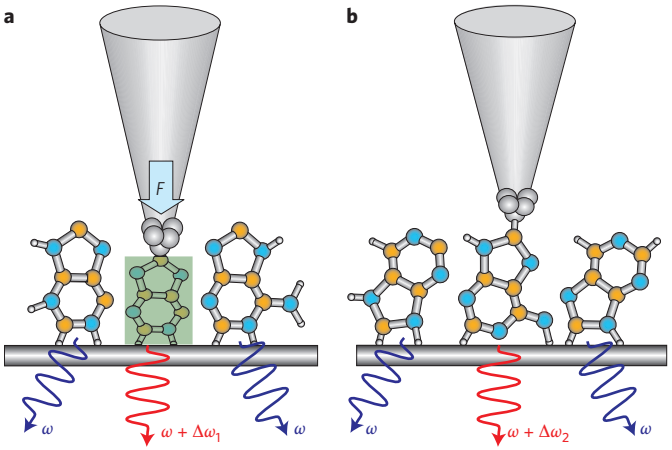


**Figure 6 | Higher resolution in TERS through mechanical and chemical effects.** **a**, When a sample is pressurized by a sharp tip during TERS measurement, selected sample molecules directly in contact with the tip apex can be compressed (coloured area). By sensing the modified vibrational frequencies of these molecules, one can achieve higher resolution. **b**, When the metallic tip comes into contact with a sample, some of the sample molecules may be adsorbed on the tip and change their orientations. This results in modified spectral response from these molecules, which can also provide very high spatial resolution, ideally to molecular level.

hot spots or boosting the surface active sites for better chemical enhancement. More recently, Le Ru *et al.* claimed that single-molecule observation is easier and more convincing when two dye molecules are mixed together[94].

## Imaging beyond plasmonics

So far in this review, we have mainly discussed the interaction between light and local plasmons of a metallic nanostructure, which invokes some interesting phenomena in optical investigation of materials. The role of plasmonics in optical imaging is remarkable, as it takes us far beyond the conventional limits of spatial resolution in optical imaging. But we still come to a resolution limit of around 10–15 nm, beyond which it seems impossible to go solely with plasmonic effects. The limit of spatial resolution in plasmon-related optical observation essentially comes from the size of the metallic nanostructure used in plasmonic studies, because the volume of the confined light, which determines the spatial resolution, is comparable to the size of the metallic nanostructure. To obtain high spatial resolution, however, one cannot simply keep on decreasing the size of the metallic structure, because plasmons are quanta of 'collective' electron oscillation, and we need a number of metal atoms to have enough free electrons for their collective oscillation.

It is therefore necessary to think beyond plasmonic effects to reach even better spatial resolution than has been achieved in TERS experiments so far. A combination of TERS with a completely different phenomenon can potentially help TERS to achieve higher resolution. For example, by combining a nonlinear optical phenomenon with TERS, as discussed earlier, the spatial resolution in TE-CARS could be improved by almost a factor of 2 in comparison with linear TERS. More recently, it has been argued that a combination of mechanical effects with TERS has the potential to improve the spatial resolution much further[95]. In this technique, controlled pressure is applied on the sample by the tip. Owing to the small size of silver grains on the surface of the tip, the actual contact area between silver-coated tip and sample is only a few nanometres. The idea is based on the fact that when the sample is pressurized by the tip, only those sample molecules that are in contact with the silver grain would feel the pressure, resulting in a perturbed spectrum

with a different spectral shape, and hence could be distinguished from the rest of the sample molecules. The mechanism is illustrated in Fig. 6a, where the sample molecules directly under the tip apex are compressed, resulting in a modified frequency of vibration compared with the vibrations of other unpressurized molecules. By sensing this spectral change, it is possible to image the sample with a spatial resolution of a few nanometres, much better than the resolution achieved in simple TERS.

Another interesting phenomenon that can be combined with TERS for better spatial resolution is the chemical effect between the sample and the silver atoms on the tip apex. The large enhancement in SERS is partially attributed to chemical effects between the sample and the silver atoms[56,89–94]. TERS, however, can provide better control over chemical effects, because the distance between the tip and the sample can be precisely regulated[58,96,97]. Figure 6b illustrates that when a metallic tip is placed on the sample under precise control, only a few molecules are chemically adsorbed on the tip. These molecules would have a different spectral response from the other molecules, providing high spatial resolution, ideally to molecula level[98].

## Future outlook

Although plasmonics has played an extremely important part in the area of nano-imaging by breaking through the conventional limits, we have come to realize that this phenomenon also has limitations on its spatial resolution. This primarily comes from the physical restrictions: for example, a certain minimum size of metallic nanostructure is required for efficient collective oscillation of plasmons. Thus going beyond plasmonics is a must for any further improvement. Although we have discussed some examples here, it will be crucial in the future to consider more physical phenomena that could be combined with plasmonics to improve the current limits. Another issue is spectroscopy with ultraviolet and deep-ultraviolet frequencies[99]. As seen in Fig. 1a, the plasmonic effect is significant only in the visible to near-infrared region. Noble metals including silver, gold and copper are not plasmonic beyond the plasmon resonance frequency, but dielectric. It will be essential to consider either natural or artificial materials that can work as plasmonic materials in this frequency region. Also, for frequencies lower than near-infrared, metals work as perfect conductors in which the wavelength shortening or slowing down of light is not observed. An artificial structure made by arranging conductive and dielectric layers can, however, show plasmonic behaviour in the terahertz (far infrared) to gigahertz (microwave) region[100]. Future research in this direction could prove to be decisive.

## References


1. Abbe, E. Beiträge zur Theorie des Mikroskops und der mikroskopischen Wahrnehmung. *Arch. Mikroskop. Anat.* **9,** 413–420 (1873).
2. Sommerfeld, A. Ueber die Fortpflanzung elektrodynamischer Wellen laengs eines Drahtes. *Ann. Phys. Chem.* **303,** 233–290 (1899).
3. Heisenberg, W. Ueber den anschaulichen Inhalt der quantentheoretischen Kinematik und Mechanik. *Z. Phys.* **43,** 172–198 (1927).
4. Inouye, Y. & Kawata, S. Near-field scanning optical microscope with a metallic probe tip. *Opt. Lett.* **19,** 159–161 (1994).
5. Pendry, J. B. Negative refraction makes a perfect lens. *Phys. Rev. Lett.* **85,** 3966–3969 (2000).
6. Smith, D. R., Schurig, D., Rosenbluth, M. & Schultz, S. Limitations on subdiffraction imaging with a negative refractive index slab. *Appl. Phys. Lett.* **82,** 1506–1508 (2003).
7. Born, M. & Wolf, E. *Principles of Optics* (Pergamon, 1959).
8. Smolyaninov, I. I., Davis, C. C., Elliott, J. & Zayats, A. V. Resolution enhancement of a surface immersion microscope near the plasmon resonance. *Opt. Lett.* **30,** 382–384 (2005).
9. Raether, H. *Surface Plasmons* (Springer, 1998).
10. Bozhevolnyi, S. I., Vohnsen, B., Smolyaninov, I. I. & Zayats, A. V. Direct observation of surface polariton localization caused by surface roughness. *Opt. Commun.* **117,** 417–423 (1995).
11. Wood, R. W. On a remarkable case of uneven distribution of light in a diffraction grating spectrum. *Phil. Mag.* **4,** 396–402 (1902).
12. Kawata, S. *Near Field Optics and Surface Plasmon Polariton* (Springer, 2001).
13. Podolskiy, V. A. & Narimanov, E. E. Near-sighted superlens. *Opt. Lett.* **30,** 75–77 (2005).
14. Taubner, T., Korobkin, D., Urzhumov, Y., Shvets, G. & Hillenbrand, R. Near-field microscopy through a SiC superlens. *Science* **313,** 1595 (2006).
15. Fang, N. & Zhang, X. Imaging properties of metamaterial superlens. *Appl. Phys. Lett.* **82,** 161–163 (2003).
16. Rao, X. R. & Ong, K. C. Subwavelength imaging by a left-handed material superlens. *Phys. Rev. E* **68,** 067601 (2003).
17. Fang, N., Lee, H., Sun, C. & Zhang, X. Sub-diffraction-limited optical imaging with a silver superlens. *Science* **308,** 534–537 (2005).
18. Liu, Z., Lee, H., Xiong, Y., Sun, C. & Zhang, X. Far-field optical hyperlens magnifying sub-diffraction-limited optics. *Science* **315,** 1686 (2007).
19. Smolyaninov, I. I., Hung, Y. J. & Davis, C. C. Magnifying superlens in the visible frequency range. *Science* **315,** 1699–1701 (2007).
20. Shvets, G., Trendafilov, S., Pendry, J. B. & Sarychev, A. Guiding, focusing, and sensing on the subwavelength scale using metallic wire arrays. *Phys. Rev. Lett.* **99,** 53903 (2007).
21. Kawata, S., Ono, A. & Verma, P. Subwavelength colour imaging with a metallic nanolens. *Nature Photon.* **2,** 438–442 (2008).
22. Kawata. S. & Shalaev, V. M. *Tip-Enhancement* (Elsevier, 2007).
23. Link, S. & El-Sayed, M. A. Spectral properties and relaxation dynamics of surface plasmon electronic oscillations in gold and silver nanodots and nanorods. *J. Phys. Chem. B* **103,** 8410–8426 (1999).
24. Sun, Y. & Xia, Y. Shape-controlled synthesis of gold and silver nanoparticles. *Science* **298,** 2176–2179 (2002).
25. Prodan, E. M., Radloff, C., Halas, N. J. & Nordlander, P. A hybridization model for the plasmon response of complex nanostructures. *Science* **302,** 419–422 (2003).
26. Hayazawa, N., Inouye, Y., Sekkat, Z. & Kawata, S. Near-field Raman scattering enhanced by a metalized tip. *Chem. Phys. Lett.* **335,** 369–374 (2001).
27. Barsegova, I. *et al.* Controlled fabrication of silver or gold nanoparticle near-field optical atomic force probes: Enhancement of second-harmonic generation. *Appl. Phys. Lett.* **81,** 3461–3463 (2002).
28. Anger, P., Bharadwaj, P. & Novotny, L. Enhancement and quenching of single-molecule fluorescence. *Phys. Rev. Lett.* **96,** 113002 (2006).
29. Hartschuh, A., Sánchez, E. J., Xie, X. S. & Novotny, L. High-resolution near-field Raman microscopy of single-walled carbon nanotubes. *Phys. Rev. Lett.* **90,** 095503 (2003).
30. Gleyzes, P., Boccara, A. C. & Bachelot, R. Near field optical microscopy using a metallic vibrating tip. *Ultramicroscopy* **57,** 318–322 (1995).
31. Zenhausern, F., O'Boyle, M. P. & Wickramasinghe, H. K. Apertureless near-field optical microscope. *Appl. Phys. Lett.* **65,** 1623–1625 (1994).
32. Knoll, B. & Keilmann, F. Near-field probing of vibrational absorption for chemical microscopy. *Nature* **399,** 134–137 (1999).
33. Bachelot, R., Gleyzes, P. & Boccara, A. C. Near-field optical microscopy by local perturbation of a diffraction spot. *Microsc. Microanal. Microstruct.* **5,** 389–397 (1994).
34. Fischer, U. C. & Pohl, D. W. Observation of single-particle plasmons by near-field optical microscopy. *Phys. Rev. Lett.* **62,** 458–461 (1989).
35. Sugiura, T., Okada, T., Inouye, Y., Nakamura, O. & Kawata, S. Gold-bead scanning near-field optical microscope with laser-force position control. *Opt. Lett.* **22,** 1663–1665 (1997).
36. Krug, J. T. II, Sánchez, E. J. & Xie, X. S. Design of near-field optical probes with optimal field enhancement by finite difference time domain electromagnetic simulation. *J. Chem. Phys.* **116,** 10895–10901 (2002).
37. Martin, Y. C., Hamann, H. F. & Wickramasinghe, H. K. Strength of the electric field in apertureless near-field optical microscopy. *J. Appl. Phys.* **89,** 5774–5778 (2001).
38. Martin, O. J. F. & Girard, C. Controlling and tuning strong optical field gradient at a local probe microscope tip apex. *Appl. Phys. Lett.* **70,** 705–707 (1997).
39. Fischer, U. C., Koglin, J. & Fuchs, H. The tetrahedral tip as a probe for scanning near-field optical microscopy at 30 nm resolution. *J. Microsc.* **176,** 231–237 (1994).
40. Koglin, J., Fischer, U. C. & Fuchs, H. Material contrast in scanning near-field optical microscopy at 1–10 nm resolution. *Phys. Rev. B.* **55,** 7977–7984 (1997).
41. Furukawa, H. & Kawata, S. Local field enhancement with an apertureless near-field-microscope probe. *Opt. Commun.* **148,** 221–224 (1998).
42. Nie, S. & Emory, S. R. Probing single molecules and single nanoparticles by surface-enhanced Raman scattering. *Science* **275,** 1102–1106 (1997).
43. Kottmann, J. P., Martin, O. J. F., Smith, D. R. & Schultz, S. Dramatic localized electromagnetic enhancement in plasmon resonant nanowires. *Chem. Phys. Lett.* **341,** 1–6 (2001).

44. Tian, Z.-Q., Ren, B. & Wu, D.-Y. Surface-enhanced Raman scattering: From noble to transition metals and from rough surfaces to ordered nanostructures. *J. Phys. Chem. B.* **106,** 9463–9483 (2002).
45. Talley, C. E. *et al.* Surface-enhanced Raman scattering from individual Au nanoparticles and nanoparticle dimer substrates. *Nano Lett.* **5,** 1569–1574 (2005).
46. Su, K.-H. *et al.* Interparticle coupling effects on plasmon resonances of nanogold particles. *Nano Lett.* **3,** 1087–1090 (2003).
47. Farahani, J. N., Pohl, D. W., Eisler, H.-J. & Hecht, B. Single quantum dot coupled to a scanning optical antenna: a tunable superemitter. *Phys. Rev. Lett.* **95,** 17402 (2005).
48. Farahani, J. N. *et al.* Bow-tie optical antenna probes for single-emitter scanning near-field optical microscopy. *Nanotechnology* **18,** 125506 (2007).
49. Mühlschlegel, P., Eisler, H.-J., Martin, O. J. F., Hecht, B. & Pohl, D. W. Resonant optical antennas. *Science* **308,** 1607–1609 (2005).
50. Schuck, P. J., Fromm, D. P., Sundaramurthy, A., Kino, G. S. & Moerner, W. E. Improving the mismatch between light and nanoscale objects with gold bowtie nanoantennas. *Phys. Rev. Lett.* **94,** 017402 (2005).
51. Hayazawa, N., Inouye, Y., Sekkat, Z. & Kawata, S. Metallized tip amplification of near-field Raman scattering. *Opt. Commun.* **183,** 333–336 (2000).
52. Pettinger, B., Ren, B., Picardi, G., Schuster, R. & Etrl, G. Nanoscale probing of adsorbed species by tip-enhanced Raman spectroscopy. *Phys. Rev. Lett.* **92,** 096101 (2004).
53. Futamata, M., Maruyama, Y. & Ishikawa, M. Critical importance of the junction in touching Ag particles for single molecule sensitivity in SERS. *J. Mol. Struct.* **735,** 75–84 (2005).
54. Hao, F. & Nordlander, P. Plasmonic coupling between a metallic nanosphere and a thin metallic wire. *Appl. Phys. Lett.* **89,** 103101 (2006).
55. Le, F., Lwin, N. Z., Halas, N. J. & Nordlander, P. Plasmonic interactions between a metallic nanoshell and a thin metallic film. *Phys. Rev. B* **76,** 165410 (2007).
56. Kneipp, K. *et al.* Single molecule detection using surface-enhanced Raman scattering (SERS). *Phys. Rev. Lett.* **78,** 1667–1670 (1997).
57. Michaels, A. M., Jiang, J. & Brus, L. Ag nanocrystal junctions as the site for surface-enhanced Raman scattering of single rhodamine 6G molecules. *J. Phys. Chem. B* **104,** 11965–11971 (2000).
58. Stöckle, R. M., Suh, Y. D., Deckert, V. & Zenobi, R. Nanoscale chemical analysis by tip-enhanced Raman spectroscopy. *Chem. Phys. Lett.* **318,** 131–136 (2000).
59. Anderson, M. S. Locally enhanced Raman spectroscopy with an atomic force microscope. *Appl. Phys. Lett.* **76,** 3130–3132 (2000).
60. Yeo, B. S., Schmid, T., Zhang, W. & Zenobi, R. Towards rapid nanoscale chemical analysis using tip-enhanced Raman spectroscopy with Ag-coated dielectric tips. *Anal. Bioanal. Chem.* **387,** 2655–2662 (2007).
61. Ichimura, T., Hayazawa, N., Hashimoto, M., Inouye, Y. & Kawata, S. Tip-enhanced coherent anti-Stokes Raman scattering for vibrational nanoimaging. *Phys. Rev. Lett.* **92,** 220801 (2004).
62. Hayazawa, N., Motohashi, M., Saito, Y. & Kawata, S. Highly sensitive strain detection in strained silicon by surface-enhanced Raman spectroscopy. *Appl. Phys. Lett.* **86,** 263114 (2005).
63. Lee, N. *et al.* High contrast scanning nano-Raman spectroscopy of silicon. *J. Raman Spectrosc.* **38,** 789–796 (2007).
64. Verma, P., Yamada, K., Watanabe, H., Inouye, Y. & Kawata, S. Near-field Raman scattering investigation of tip effects on $C_{60}$ molecules. *Phys. Rev. B* **73,** 045416 (2006).
65. Domke, K. F., Zhang, D. & Pettinger, B. Tip-enhanced Raman spectra of picomole quantities of DNA nucleobases at Au(111). *J. Am. Chem. Soc.* **129,** 6708–6709 (2007).
66. Rasmussen, A. & Deckert, V. Surface- and tip-enhanced Raman scattering of DNA components. *J. Raman Spectrosc.* **37,** 311–317 (2006).
67. Zhang, W. H., Yeo, B. S., Schmid, T. & Zenobi, R. Single molecule tip-enhanced Raman spectroscopy with silver tips. *J. Phys. Chem. C* **111,** 1733–1738 (2007).
68. Hartschuh, A., Qian, H., Meixner, A. J., Anderson, N. & Novotny, L. Nanoscale optical imaging of single-walled carbon nanotubes. *J. Lumin.* **119–120,** 204–208 (2006).
69. Yano, T., Verma, P., Kawata, S. & Inouye, Y. Diameter-selective near-field Raman analysis and imaging of isolated carbon nanotube bundles. *Appl. Phys. Lett.* **88,** 093125 (2006).
70. Sánchez, E. J., Novotny, L. & Xie, X. S. Near-field fluorescence microscopy based on two-photon excitation with metal tips. *Phys. Rev. Lett.* **82,** 4014–4017 (1999).
71. Yang, H. *et al.* Protein conformational dynamics probed by single-molecule electron transfer. *Science* **302,** 262–266 (2003).
72. Lakowicz, J. R. *et al.* Advances in surface-enhanced fluorescence. *J. Fluoresc.* **14,** 425–441 (2004).
73. Bharadwaj, P., Anger, P. & Novotny, L. Nanoplasmonic enhancement of single-molecule fluorescence. *Nanotechnology* **18,** 44017 (2007).
74. Gerton, J. M. *et al.* Tip-enhanced fluorescence microscopy at 10 nanometer resolution. *Phys. Rev. Lett.* **93,** 180801 (2004).
75. Ma, Z., Gerton, J. M., Wade, L. A. & Quake, S. R. Fluorescence near-field microscopy of DNA at sub-10 nm resolution. *Phys. Rev. Lett.* **97,** 260801 (2006).
76. Huang, F. M., Festy, F. & Richards, D. Tip-enhanced fluorescence imaging of quantum dots. *Appl. Phys. Lett.* **87,** 183101 (2005).
77. Steidtner, J. & Pettinger, B. Tip-enhanced Raman spectroscopy and microscopy on single dye molecules with 15 nm resolution. *Phys. Rev. Lett.* **100,** 236101 (2008).
78. Kühn, S., Håkanson, U., Rogobete, L. & Sandoghdar, V. Enhancement of single-molecule fluorescence using a gold nanoparticle as an optical nanoantenna. *Phys. Rev. Lett.* **97,** 017402 (2006).
79. Hartschuh, A., Qian, H., Meixner, A. J., Anderson, N. & Novotny, L. Nanoscale optical imaging of excitons in single-walled carbon nanotubes. *Nano Lett.* **5,** 2310–2313 (2005).
80. Höppener, C. & Novotny, L. Antenna-based optical imaging of single $Ca^{2+}$ transmembrane proteins in liquids. *Nano Lett.* **8,** 642–646 (2008).
81. Höppener, C. & Novotny, L. Imaging of membrane proteins using antenna-based optical microscopy. *Nanotechnology* **19,** 384012 (2008).
82. Xu, H.-X., Bjerneld, E. J., Käll, M. & Börjesson, L. Spectroscopy of single hemoglobin molecules by surface enhanced Raman scattering. *Phys. Rev. Lett.* **83,** 4357–4360 (1999).
83. Weiβ, J. *et al.* The unimolecular dissociation of the OH stretching states of HOCl: Comparison with experimental data. *J. Chem. Phys.* **115,** 8880–8887 (2001).
84. Hildebrandt, P. & Stockburger, M. Surface-enhanced resonance Raman spectroscopy of rhodamine 6G adsorbed on colloidal silver. *J. Phys. Chem.* **88,** 5935–5944 (1984).
85. Corni, S. & Tomasi, J. Surface enhanced Raman scattering from a single molecule adsorbed on a metal particle aggregate: A theoretical study. *J. Chem. Phys.* **116,** 1156–1164 (2002).
86. Peleg, G. *et al.* Gigantic optical non-linearities from nanoparticle-enhanced molecular probes with potential for selectively imaging the structure and physiology of nanometric regions in cellular systems. *Bioimaging* **4,** 215–324 (1996).
87. Peleg, G., Lewis, A., Linial, M. & Loew, L. M. Nonlinear optical measurement of membrane potential around single molecules at selected cellular sites. *Proc. Natl Acad. Sci. USA* **96,** 6700–6705 (1999).
88. Xu, H., Bjerneld, E. J., Kall, M. & Borjesson, L. Spectroscopy of single hemoglobin molecules by surface enhanced Raman scattering. *Phys. Rev. Lett.* **83,** 4357–4360 (1999).
89. Doering, W. E. & Nie, S. Single-molecule and single-nanoparticle SERS: Examining the roles of surface active sites and chemical enhancement. *J. Phys. Chem. B* **106,** 311–317 (2002).
90. Futamata, M., Maruyama, Y. & Ishikawa, M. Metal nanostructures with single molecule sensitivity in surface enhanced Raman scattering. *Vib. Spectrosc.* **35,** 121–129 (2004).
91. Xu, H. X., Aizpurua, J., Kall, M. & Apell, P. Electromagnetic contributions to single-molecule sensitivity in surface-enhanced Raman scattering. *Phys. Rev. E* **62,** 4318–4324 (2000).
92. Otto, A., Mrozek, I., Grabhorn, H. & Akemann, W. Surface-enhanced Raman scattering. *J. Phys. Condens. Matter* **4,** 1143–1212 (1992).
93. Stöckle, R. M., Deckert, V., Fokas, C., Zeisel, D. & Zenobi, R. Sub-wavelength Raman spectroscopy on isolated silver islands. *Vib. Spectrosc.* **22,** 39–48 (2000).
94. Le Ru, E. C., Meyer, M. & Etchegoin, P. G. Proof of single-molecule sensitivity in surface enhanced Raman scattering (SERS) by means of a two-analyte technique. *J. Phys. Chem. B* **110,** 1944–1948 (2006).
95. Yano, T., Inouye, Y. & Kawata, S. Nanoscale uniaxial pressure effect of a carbon nanotube bundle on tip-enhanced near-field Raman spectra. *Nano Lett.* **6,** 1269–1273 (2006).
96. Bharadwaj, P. & Novotny, L. Spectral dependence of single molecule fluorescence enhancement. *Opt. Express* **15,** 14266–14274 (2007).
97. Ichimura, T. *et al.* Subnanometric near-field Raman investigation in the vicinity of a metallic nanostructure. *Phys. Rev. Lett.* **102,** 186101 (2009).
98. Ichimura, T. *et al.* Temporal fluctuation of tip-enhanced Raman spectra of adenine molecules. *J. Phys. Chem. C* **111,** 9460–9464 (2007).
99. Taguchi, A., Hayazawa, N., Furusawa, K., Ishitobi, H. & Kawata, S. Deep-UV tip-enhanced Raman scattering. *J. Raman Spectrosc.* doi:10.1002/jrs.2287 (2009).
100. Pendry, J. B., Martin-Moreno, L. & Garcia-Vidal, F. J. Mimicking surface plasmons with structured surface. *Science* **305,** 847–848 (2004).


## Acknowledgements

This work was supported by the Core Research for Educational Science and Technology (CREST) project of the Japan Science and Technology Corporation, and by the RIKEN Extreme Photonics programme.

nature photonics

LETTERS

PUBLISHED ONLINE: 21 JUNE 2009 | DOI: 10.1038/NPHOTON.2009.95

# Nonlinear generation and manipulation of Airy beams

Tal Ellenbogen*, Noa Voloch-Bloch, Ayelet Ganany-Padowicz and Ady Arie*

**Recently, the first experimental observation of a new class of non-diffracting optical beams that freely accelerate in space was reported[1]. These so-called Airy beams were shown to be useful for optical micro-manipulation of small particles[2] and for the generation of curved plasma channels in air[3]. To date, these beams have been generated only by using linear diffractive elements. Here, we show a new way of generating Airy beams by using three-wave mixing processes, which occur in asymmetric nonlinear photonic crystals. We experimentally generated a second-harmonic Airy beam and examined the tuning properties of the nonlinear interaction and propagation dynamics of the pump and second-harmonic output beams. This nonlinear generation process enables Airy beams to be obtained at new wavelengths, and opens up new possibilities for all-optical switching and manipulation of Airy beams.**

Airy wavepackets were first predicted by Berry and Balazs[4] in the context of quantum mechanics as a free-particle solution of the Schrödinger equation. The envelope of these wavepackets is described by Airy functions, centred around a parabolic trajectory in space. The Airy wavepacket is the only non-spreading solution in one dimension. Its unique acceleration property is attributed to the caustic of the wavepacket and not to the centre of mass, so the acceleration does not contradict Ehrenfest's theorem.

The theoretical background to the generation of optical Airy beams was only recently presented[5], followed soon by their first experimental observation[1]. The ballistic dynamics of the beams, together with their facility to bypass obstacles, were examined[6]. Their special self-healing properties, that is, self-restoration of their canonical form after passing small obstacles, have been theoretically and experimentally demonstrated[2,7]. The dynamics of the first and second moments of these beams under different excitation parameters have also been studied[8], and it has been shown that, according to Ehrenfest's theorem, the centre of mass moves in a straight line but the local features of the beam show a nonlinear lateral shift. It has also been shown that the linear and angular momentum of these beams change during propagation, and the total momentum and energy are conserved[9].

To date, all studies have examined Airy beams generated by linear diffractive elements. In this work we investigate a novel type of Airy beams generated by three-wave mixing (TWM) processes, taking place in an asymmetrically modulated quadratic nonlinear optical media. The asymmetric structure induces a cubic phase front to the generated TWM output, for which the Fourier transform is an accelerating Airy beam[1].

Quasi-phase matching (QPM) in quadratic nonlinear photonic crystals[10,11] has attracted a great deal of interest in recent years, mainly due to the major improvements in poling technology that have enabled us diverse types of one- and two-dimensional nonlinear structures[12–14] with sub-micrometre resolution to be both designed and engineered[15]. The generation of Airy beams by quadratic nonlinear processes opens up new possibilities to control and manipulate their properties[16,17].

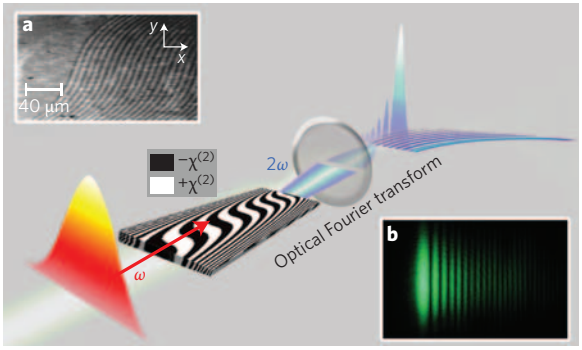


**Figure 1 | Nonlinear generation of Airy beams.** A Gaussian pump is converted to a second-harmonic Airy beam in an asymmetric nonlinear photonic crystal. $\omega$ is the angular frequency of the Gaussian pump beam. **a**, Microscope photograph of the C$^-$ facet of the quadratic crystal, after selective etching (which reveals the inverted domain pattern). The *x*- and *y*-axes were rescaled for viewing purposes and are not comparable. **b**, Profile photograph of the green second-harmonic Airy beam.

To generate the Airy beam we designed and fabricated an asymmetric quadratic nonlinear photonic structure with the following space-dependent quadratic nonlinear coefficient:

$$\chi^{(2)}(x,y) = d_{ij}\mathrm{sign}[\cos(2\pi f_x x + f_c y^3)] \qquad (1)$$

where $d_{ij}$ is an element of the quadratic susceptibility $\chi^{(2)}$ tensor, $f_x$ is the spatial frequency of the modulation in the beam's propagation direction, and $f_c$ represents the strength of the cubic modulation in the transverse direction. An illustration of the structure and the unique conversion process is shown in Fig. 1. This binary modulation function can be expanded to a series of oscillating terms with a dominant first-order term equal to $(2/\pi)\exp[\pm i(2\pi f_x x + f_c y^3)]$.

For simplicity we consider a two-dimensional second-harmonic generation (SHG) problem with a plane pump wave that propagates in the *x*-direction, and generation of a collinear second-harmonic wave with an arbitrary envelope as follows:

$$E_1(x,y) = A_1 e^{ik_1 x}, \quad E_2(x,y) = A_2(x,y)e^{ik_2 x} \qquad (2)$$

where $A_1$ and $k_1$ ($A_2$ and $k_2$) are the amplitude and wavevector of the first-harmonic (and second-harmonic) wave, respectively. By inserting the first-order term of the structure to the nonlinear wave equation we obtain

$$\nabla^2 A_2(x,y) + k_2^2 A_2(x,y) = -CA_1^2 e^{i(2k_1 - k_2 + 2\pi f_x)x + if_c y^3} \qquad (3)$$

Department of Physical Electronics, Fleischman Faculty of Engineering, Tel-Aviv University, Tel-Aviv 69978, Israel. *e-mail: ellenbog@post.tau.ac.il; ady@eng.tau.ac.il

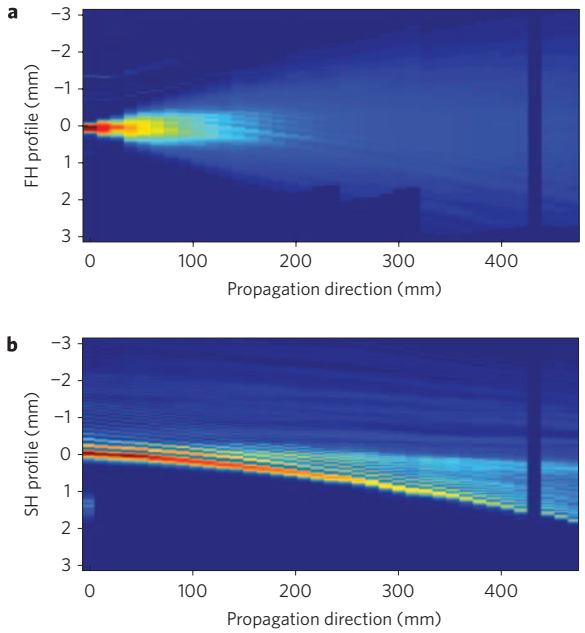


**Figure 2 | Recorded propagation dynamics of the optically Fourier transformed output beams. a**, Output first-harmonic (FH) pump beam. **b**, Output second-harmonic (SH) Airy beam.

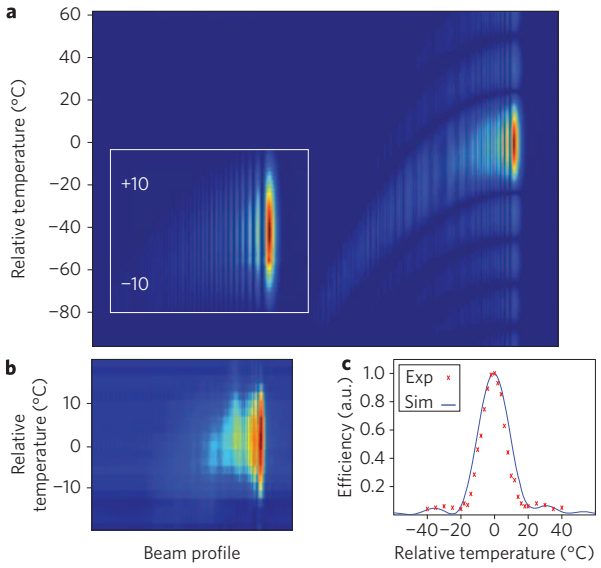


**Figure 3 | Temperature tuning of the nonlinear interaction. a**, Simulation of the second-harmonic beam profile (absolute amplitude values) as a function of the crystal temperature relative to phase matching point. Inset: main lobe intensity pattern. **b**, Experimental results for main lobe intensity pattern at the far field versus temperature. **c**, Simulation and experimental curves of doubling efficiency versus temperature.

where $C$ is a nonlinear coupling coefficient. The right-hand side of this equation is the nonlinear polarization source. In collinear QPM conditions, the difference between the wavevectors of the second-harmonic and fundamental waves satisfies a momentum conservation law, $k_2 - 2k_1 = 2\pi f_x$, so the polarization source oscillations in the propagation direction are reduced and a build-up of a second-harmonic wave with a cubic phase front occurs that results from the transverse component of the polarization source term. Performing an optical Fourier transform, for example, using a lens, on the TWM output (second-harmonic in this case), results in the Airy beam[1,5].

We fabricated the suggested structure by two-dimensional poling of a stoichiometric lithium tantalate (SLT) nonlinear crystal (see Methods) and generated an Airy beam at the second-harmonic of a single-mode Gaussian Nd:YLF pump. A microscope photograph of the modulated nonlinear crystal after selective etching and a photograph of the green second-harmonic Airy beam profile at the far field are shown in Fig. 1, insets (a) and (b). Using a pump wave with 3.6 kW peak power we measured a second-harmonic wave with a peak power of 42 W, giving an internal conversion efficiency (without Fresnel reflections at the crystal facets) of $8.2 \times 10^{-6}$ W$^{-1}$. In addition, we performed an optical Fourier transform to the output of the nonlinear photonic crystal, using a lens of 100 mm focal length, and recorded the propagation dynamics of the Fourier transformed pump and second-harmonic waves, as shown in Fig. 2 (see Methods).

The output pump wave has Gaussian beam propagation dynamics with slight intensity modulations that might be caused by small linear variations in the crystal due to the poling process. The output second-harmonic beam shows the propagation dynamics of a truncated Airy beam, that is, nearly non-diffracting and freely accelerating to one side. The size of the first lobe at the focal point of the lens was 147 μm.

The measured temperature tuning properties of the nonlinear interaction were compared to a split-step Fourier numerical simulation (see Methods and Fig. 3). The maximum conversion efficiency achieved by this structure was calculated to be ~0.9 of the maximum conversion efficiency achieved by a conventional one-dimensional periodically poled structure under the same experimental configuration. The inset shows the intensity pattern of the main phase matching lobe versus the temperature of the crystal, and Fig. 3b shows the experimental results. Note that for different phase matching conditions we obtain beams with slightly different profiles. This affects the propagation dynamics of the different output beams, as we discuss in the next paragraph. Figure 3c shows the numerical and experimental efficiency tuning curves, which are similar in shape to conventional temperature tuning curves[10,12]. The temperature of maximum intensity was 157 °C in the simulation and 120 °C in the experiment, possibly resulting from slight inaccuracies in the dispersion equation. Nevertheless, there is good agreement between the simulated and measured tuning properties.

The nonlinear response provides new possibilities for manipulating and controlling Airy beams that cannot be achieved using linear optics. One option, shown in Fig. 4, is all-optical shaping of the caustic of the Airy beam. We simulated the propagation properties of the second-harmonic output at different phase-matching conditions, that is, different temperatures or pump wavelengths and show output results for values that are in the main phase-matching lobe shown in Fig. 3. It is demonstrated that the caustic property of Airy beams is maintained even outside phase-matching conditions; however, for different phase-matching conditions the output beam peaks at different places along the parabolic trajectory. The peak intensity values for Fig. 4a–f with respect to a phase-matched interaction are 0.05, 0.57, 1, 0.5, 0.21 and 0.12. Shaping of the caustic by changing the phase-matching conditions of the crystal is a unique property of the generation of Airy beams using nonlinear photonic structures and could be applied in fluidic micro-manipulation[2] and in the generation of curved plasma channels[3].

Another application of the nonlinear response is to all-optically control the acceleration direction of the beam by relying on the physical difference between up-conversion and down-conversion processes. The phase mismatch values for up-conversion and down-conversion processes that involve the same three waves are opposite, so phase-matching terms with opposite signs are required by the nonlinear structure. This idea was proposed for switching the

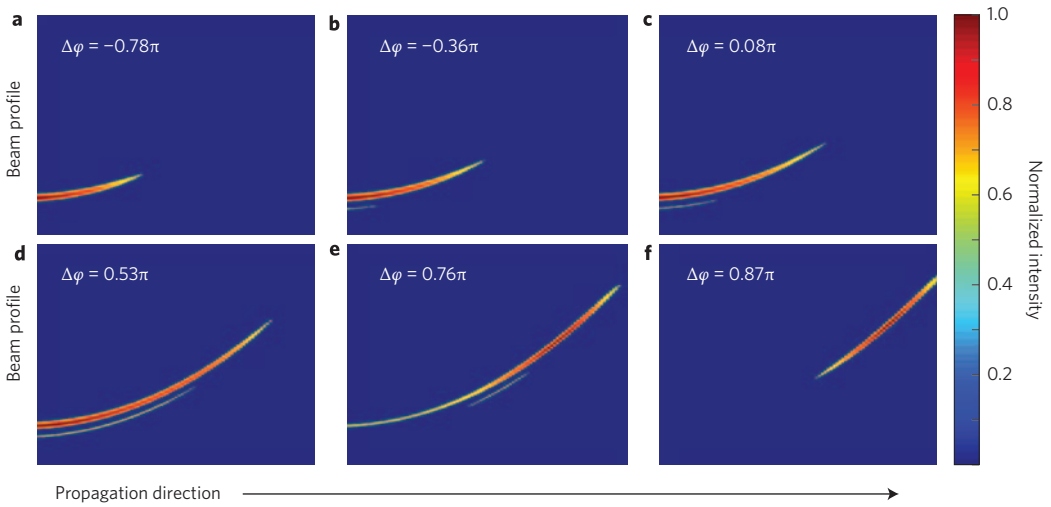


**Figure 4 | Shaping the caustic of the generated Airy wavepacket by changing phase-matching conditions ($\Delta\varphi = \Delta kL/2$).** The full intensity profile of the different panels resembles an Airy beam propagation profile; however, we have eliminated all values lower than half maximum values for viewing purposes. The left side of each panel is the origin of the Airy beam that propagates to the right. **a**, $\Delta\varphi = -0.78\pi$; **b**, $\Delta\varphi = -0.36\pi$; **c**, $\Delta\varphi = 0.08\pi$; **d**, $\Delta\varphi = 0.53\pi$; **e**, $\Delta\varphi = 0.76\pi$; **f**, $\Delta\varphi = 0.87\pi$.

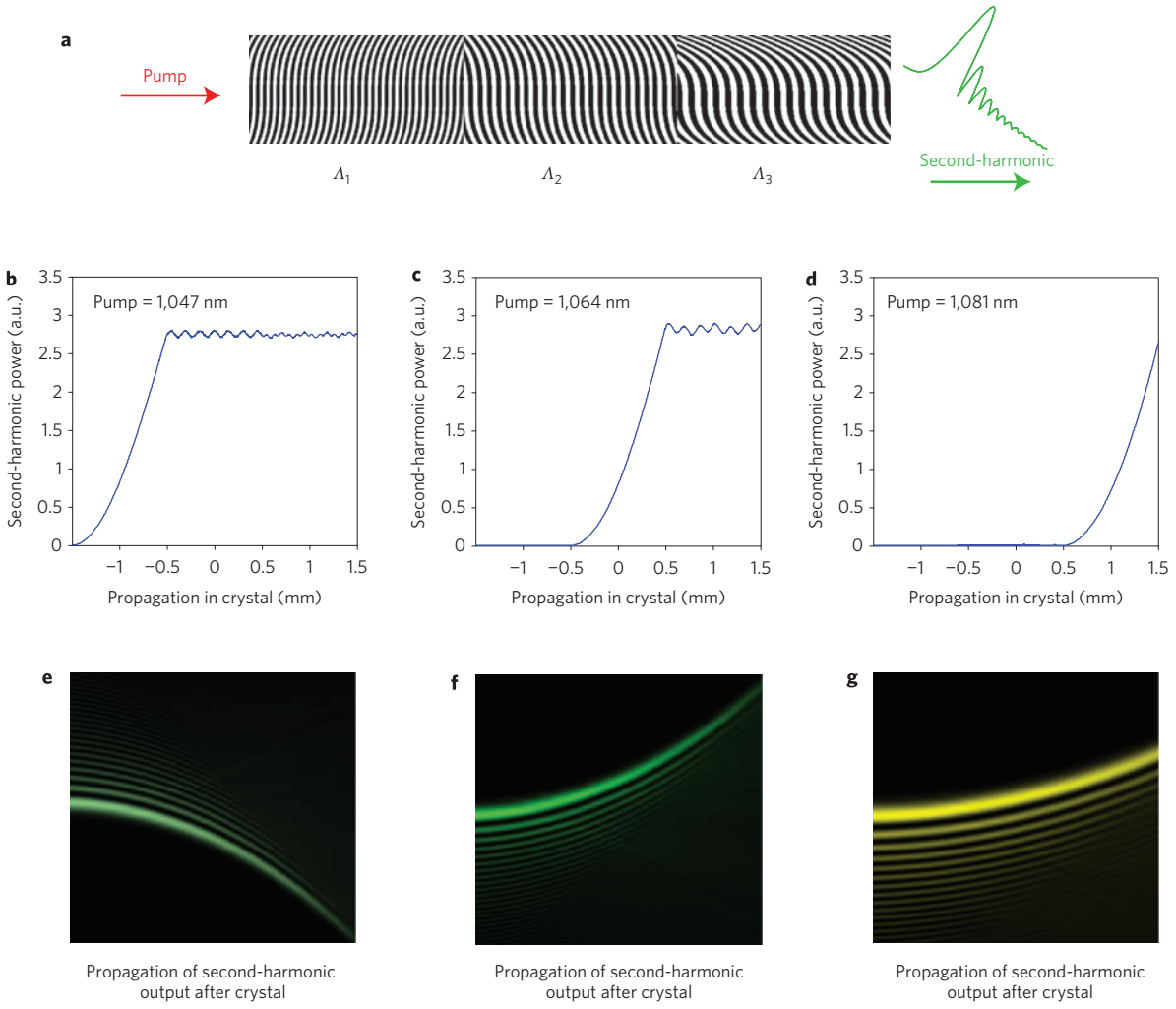


**Figure 5 | All-optical control of the Airy beam's acceleration properties using cascaded nonlinear structures with different periods in the propagation direction. a**, Illustration of the simulated structure in SLT crystal, where $\Lambda$ is the poling period of each subsection of the structure. In the simulations we used $\Lambda_1 = 7.38\,\mu m$, $\Lambda_2 = 7.75\,\mu m$ and $\Lambda_3 = 8.12\,\mu m$. **b–d**, Second-harmonic build-up in the crystal for different pump wavelengths and **e–g**, Respective output beams at the second-harmonic.

optical helicity of nonlinearly generated optical vortex beams[18]. By examining the polarization source in equation (3) under collinear QPM conditions in these two cases we obtain

$$S^{NL} = -C_1 e^{\pm i f_c y^3} \quad (4)$$

where $S^{NL}$ is the phase-matched nonlinear source and $C_1$ includes also the amplitudes of the generating waves. Switching from one process to another by choosing proper pump beams that satisfy the corresponding QPM conditions will change the sign of the effective cubic phase parameter $f_c$ and will therefore generate an Airy beam with an opposite acceleration direction. All-optical control of the acceleration of the Airy beam can also be achieved by using cascaded structures with different cubic phase parameter and slightly different QPM conditions. Slight changes in the wavelengths of the pump beams can control the origin of the generated Airy beam and the acceleration, as illustrated in Fig. 5.

In conclusion, we have extended the idea of linear generation of Airy beams to nonlinear quadratic crystals and demonstrated experimentally, for the first time, the generation of an Airy beam at the second harmonic of a Gaussian pump laser. Our method allows the creation of Airy beams at new wavelengths and high intensities that are not supported by conventional methods. Other possibilities for obtaining Airy beams at new wavelengths include using nonlinear mode conversion[19] or performing the nonlinear wave mixing of Airy beams at the Fourier plane, which will preserve the cubic phase of the interaction. In addition to the experimental realization of an Airy beam by TWM, we have shown by simulations that the caustic property of the wavepacket is maintained even for non-phase-matched interactions. Furthermore, we have demonstrated that the nonlinear generation of Airy beams allows all-optical control of the caustic and the acceleration properties of the beams. The nonlinear generation of Airy beams may also enable Airy beams to be parametrically amplified and may be useful in new quantum optics applications based on spontaneous parametric down-conversion. The idea presented here can be extended to other fields that make use of the QPM technique, for example, to generate and control extreme ultraviolet Airy beams by quasi-phase-matched high harmonic generation.

## Methods

**Fabrication of the crystal.** We have used a conventional fabrication technique for the poling process[17,20]. The modulation period in the propagation direction $1/f_x$ was 7.38 μm and the cubic modulation coefficient $f_c$ was $1.9 \times 10^{-7}$ μm$^{-3}$. The size of the modulated channel was $1 \times 1$ mm$^2$. We weakly focused the pump beam to the modulated crystal with waist radii of ~700 and ~45 μm in the crystallographic $y$- and $z$-directions, respectively. The maximum value of cubic coefficient for a fixed channel width and fixed $1/f_x$ value is limited by the minimum domain size possible. Using state-of-the-art poling technology[15] we can achieve sub-micrometre domain resolution, which in our configuration will enable us to obtain $f_c = 123 \times 10^{-7}$ μm$^{-3}$—two orders of magnitude larger.

**Recording the propagation dynamics and temperature dependence.** We placed a charge-coupled device camera after the focal spot of the lens and captured either the pump or second-harmonic intensity distributions (using appropriate bandpass filters) every 0.5 inches. From the photographs we derived the intensity profiles of the pump and second-harmonic waves. We used the straight trajectory of the pump to correct small lateral misalignments of the camera at different places along the trail. These profile measurements were used to produce Fig. 2.

To produce Fig. 3b we captured the far-field output of the crystal for different temperatures and derived the intensity profiles.

**Numerical simulation.** We simulated the nonlinear interaction using a split-step Fourier method[21]. We divided the modulated crystal into slabs of 2 μm thickness, and convolved in each slab the generated nonlinear source with the impulse response of a free-space slab. To examine the propagation dynamics of the output we calculated its Fourier transform (as was done in the experiments using a lens) and propagated the transformed output in free space.

Received 5 January 2009; accepted 13 May 2009; published online 21 June 2009

## References


1. Siviloglou, G. A., Broky, J., Dogariu, A. & Christodoulides, D. N. Observation of accelerating Airy beams. *Phys. Rev. Lett.* **99,** 213901 (2007).
2. Baumgartl, J., Mazilu, M. & Dholakia, K. Optically mediated particle clearing using Airy wavepackets. *Nature Photon.* **2,** 675–678 (2008).
3. Polynkin, P., Kolesik, M., Moloney, J. V., Siviloglou, G. A. & Christodoulides, D. N. Curved plasma channel generation using ultraintense Airy beams. *Science* **324,** 229–232 (2009).
4. Berry, M. V. & Balazs, N. L. Nonspreading wave packets. *Am. J. Phys.* **47,** 264–267 (1979).
5. Siviloglou, G. A. & Christodoulides, D. N. Accelerating finite energy Airy beams. *Opt. Lett.* **32,** 979–981 (2007).
6. Siviloglou, G. A., Broky, J., Dogariu, A. & Christodoulides, D. N. Ballistic dynamics of Airy beams. *Opt. Lett.* **33,** 207–209 (2008).
7. Broky, J., Siviloglou, G. A., Dogariu, A. & Christodoulides, D. N. Self-healing properties of optical Airy beams. *Opt. Express* **16,** 12880–12891 (2008).
8. Besieris, I. M. & Shaarawi, A. M. A note on an accelerating finite energy Airy beam. *Opt. Lett.* **32,** 2447–2449 (2007).
9. Sztul, H. I. & Alfano, R. R. The Poynting vector and angular momentum of Airy beams. *Opt. Express* **16,** 9411–9416 (2008).
10. Fejer, M. M., Magel, G. A., Jundt, D. H. & Byer, R. L. Quasi-phase-matched second harmonic generation: tuning and tolerances. *IEEE J. Quantum Electron.* **28,** 2631–2654 (1992).
11. Berger, V. Nonlinear photonic crystals. *Phys. Rev. Lett.* **81,** 4136–4139 (1998).
12. Broderick, N. G. R., Ross, G. W., Offerhaus, H. L., Richardson, D. J. & Hanna, D. C. Hexagonally poled lithium niobate: a two-dimensional nonlinear photonic crystal. *Phys. Rev. Lett.* **84,** 4345–4348 (2000).
13. Arie, A., Bahabad, A. & Habshoosh, N. Nonlinear interactions in periodic and quasi-periodic nonlinear photonic crystals, in *Ferroelectric Crystals for Photonic Applications* (eds Ferraro, P., Grilli, S. & De Natale, P.) Ch. 10, 259–284 (Springer Verlag, 2009).
14. Kasimov, D. *et al.* Annular symmetry nonlinear frequency converters. *Opt. Express* **14,** 9371–9376 (2006).
15. Canalias, C. & Pasiskevicius, V. Mirrorless optical parametric oscillator. *Nature Photon.* **1,** 459–462 (2007).
16. Konig, F., Mason, E. J., Wong, F. N. C. & Albota, M. A. Efficient and spectrally bright source of polarization-entangled photons. *Phys. Rev. A* **71,** 033805 (2005).
17. Ellenbogen, T., Ganany-Padowicz, A. & Arie, A. Nonlinear photonic structures for all-optical deflection. *Opt. Express* **16,** 3077–3082 (2008).
18. Bahabad, A. & Arie, A. Generation of optical vortex beam by nonlinear wave mixing. *Opt. Express* **15,** 17619–17624 (2007).
19. Ellenbogen, T., Dolev, I. & Arie, A. Mode conversion in quadratic nonlinear crystals. *Opt. Lett.* **33,** 1207–1209 (2008).
20. Furukawa, Y., Kitamura, K., Suzuki, E. & Niwa, K. Stoichiometric $LiTaO_3$ single crystal growth by double-crucible Czochralski method using automatic powder supply system. *J. Cryst. Growth* **197,** 889–895 (1999).
21. Agrawal, G. P. *Nonlinear Fiber Optics* (Academic Press, 1995).


## Acknowledgements

T.E. thanks Y. Sivan for fruitful discussions. This work was supported by the Israeli Science Foundation, grant no. 960/05 and by the Israeli Ministry of Science, Culture and Sport.

## Additional information

Reprints and permission information is available online at http://npg.nature.com/reprintsandpermissions/. Correspondence and requests for materials should be addressed to T.E. and A.A.

nature photonics

LETTERS

PUBLISHED ONLINE: 21 JUNE 2009 | DOI: 10.1038/NPHOTON.2009.97

# Optical entanglement of co-propagating modes

J. Janousek[1]*, K. Wagner[1], J-F. Morizur[1,2], N. Treps[2], P. K. Lam[1], C. C. Harb[3] and H-A. Bachor[1]

**Optical entanglement is a key requirement for many quantum communication protocols[1]. Conventionally, entanglement is formed between two distinct beams, with the quantum correlation measurements being performed at separate locations. Such setups can be complicated, requiring the repeated combination of complex resources, a task that becomes increasingly difficult as the number of entangled information channels, or modes, increases. We pave the way towards the realization of optical multimode quantum information systems by showing continuous variable entanglement between two spatial modes within one beam. Our technique is a major advance towards practical systems with minimum complexity. We demonstrate three major experimental achievements. First, only one source is required to produce squeezed light in two orthogonal spatial modes. Second, entanglement is formed through lenses and beam rotation, without the need for a beamsplitter. Finally, quantum correlations are measured directly and simultaneously using a multipixel quadrant detector.**

Optical entanglement between two laser beams has been used to study the fundamental quantum properties of light[2] and for the demonstration of quantum communication protocols[1]. The detection of continuous variables, the amplitude and phase quadratures, has been used to show dense coding[3], teleportation[4,5], quantum secret sharing[6] and entanglement distillation[7,8]. This was extended to the spatial domain, demonstrating Einstein-Podolsky-Rosen (EPR) correlations between position and momentum of the photons in two laser beams[9–11].

Multimode entanglement allows more complex processes and leads to more advanced techniques. Tripartite Greenberger-Horne-Zeilinger (GHZ) correlations and, more recently, cluster states combining four individual squeezed modes, have been demonstrated with impressive reliability[12,13]. However, using separate beams to build the quantum state requires the use of complex resources, in particular several squeezers, with many beamsplitters, phase shifters and a set of separate homodyne detectors. This technology is difficult to simplify as it is very sensitive to losses and any mode mismatch.

An alternative approach is to consider multiple orthogonal modes within a single beam. There have been proposals to use correlated modes with different frequencies generated in one source[14], to correlate several frequency sidebands[15] or to use temporal modes that describe different pulse shapes[16]. Spatial modes, in the basis of Hermite–Gaussian (H–G) modes $TEM_{nm}$, can be generated efficiently, squeezed[17], superposed with low losses[18,19] and many modes can be measured simultaneously using a single multipixel homodyne detector[11,20]. Shaping the local oscillator using a spatial light modulator and varying the gains on the pixels of the detector changes the measurement basis. This can create a family of orthogonal measurements. As an in-principle demonstration, we report here the entanglement of two spatial modes, $TEM_{01}$ and $TEM_{10}$, within one beam.

The crucial resource required in creating entangled beams is the squeezed light source. Here we use the well tested process of optical parametric amplification. There are several cavity designs for optical parametric amplifiers (OPA), the most common of which are the linear and bow-tie geometries. We use the linear design so as to benefit from the natural degeneracy of optical resonators with cylindrical symmetry[21].

Squeezed light in two orthogonal spatial modes was produced using a single degenerate OPA operating in the deamplification regime (Fig. 1a). The OPA was pumped with 532 nm light from a frequency-doubled diode-pumped Nd:YAG laser operating at 1,064 nm. The OPA crystal had dimensions $2 \times 2.5 \times 6.5\ mm^3$ and was made from bulk $LiNbO_3$, which was 7% doped with MgO and phase-matched at 61 °C. The OPA cavity was linear and formed by the rear surface of the crystal (radius of curvature = 8 mm, high reflector at 532 nm, $R = 99.9\%$ at 1,064 nm) and an external mirror (radius of curvature = 25 mm, $R = 10\%$ at 532 nm and $R = 96\%$ at 1,064 nm). The front surface of the crystal had a radius of curvature of 8 mm and was antireflection-coated at both 1,064 nm and 532 nm. The optical path length of the OPA cavity was ~38 mm.

The system was seeded with a weak $TEM_{01}$ field incident on the high-reflecting side of the OPA crystal and was carefully aligned such that the two orthogonal modes, that is $TEM_{01}$ bright mode and $TEM_{10}$ vacuum mode, resonated simultaneously. This degeneracy was optimized by changing the temperature of the laser crystal. The system was operated as a deamplifier with a gain of 0.4 using 180 mW pump power in the $TEM_{00}$ mode. This pump mode is not an optimum mode for an OPA operating in the $TEM_{01}$ mode, but still provides sufficient nonlinear gain[22]. As expected, a low-intensity amplitude squeezed field in the $TEM_{01}$ mode was produced. However, as the nonlinear crystal cavity was also resonant for the $TEM_{10}$ vacuum mode, the system operated as an optical parametric oscillator (OPO) below threshold for this particular mode. This resulted in the generation of vacuum squeezed light in $TEM_{10}$ mode, which for a perfectly aligned cavity would be exactly in-phase with the $TEM_{01}$ amplitude squeezed field.

The multimode squeezed light was analysed using homodyne detection (HD) with the local oscillator (LO) in the $TEM_{01}$ mode. We used a Dove prism for the spatial rotation of the LO beam so as to analyse the output of the degenerate OPA in any direction, that is, going from $TEM_{01}$ ($\theta = 0°$) to $TEM_{10}$ mode ($\theta = 90°$) and in between[23,24]. For $TEM_{01}$ operation, we typically observed −4 dB of squeezing and +6.5 dB of anti-squeezing at 4.8 MHz detection frequency, (Fig. 1b). More interestingly, we observed states of approximately the same squeezing and antisqueezing when the LO $TEM_{01}$ mode was rotated with respect to the $x$-axis, (Fig. 1c). This clearly demonstrates multimode squeezing generation using a single linear degenerate OPA.

To verify that the two orthogonal states produced by the degenerate OPA are independent we used a quadrant detector (QD) with one LO field in the $TEM_{00}$ mode, (Fig. 2a). The eigenmode of such a detection system is a flipped mode, (Fig. 2b), giving us at best only 64% efficiency for $TEM_{01}$ detection. By combining the outputs of

[1]ARC Centre of Excellence for Quantum-Atom Optics, The Australian National University, Canberra, Australia, [2]Laboratoire Kastler Brossel, Université Pierre et Marie Curie – Paris 6, ENS, CNRS, Paris, France, [3]Australian Defence Force Academy, Canberra, Australia. *e-mail: jiri.janousek@anu.edu.au

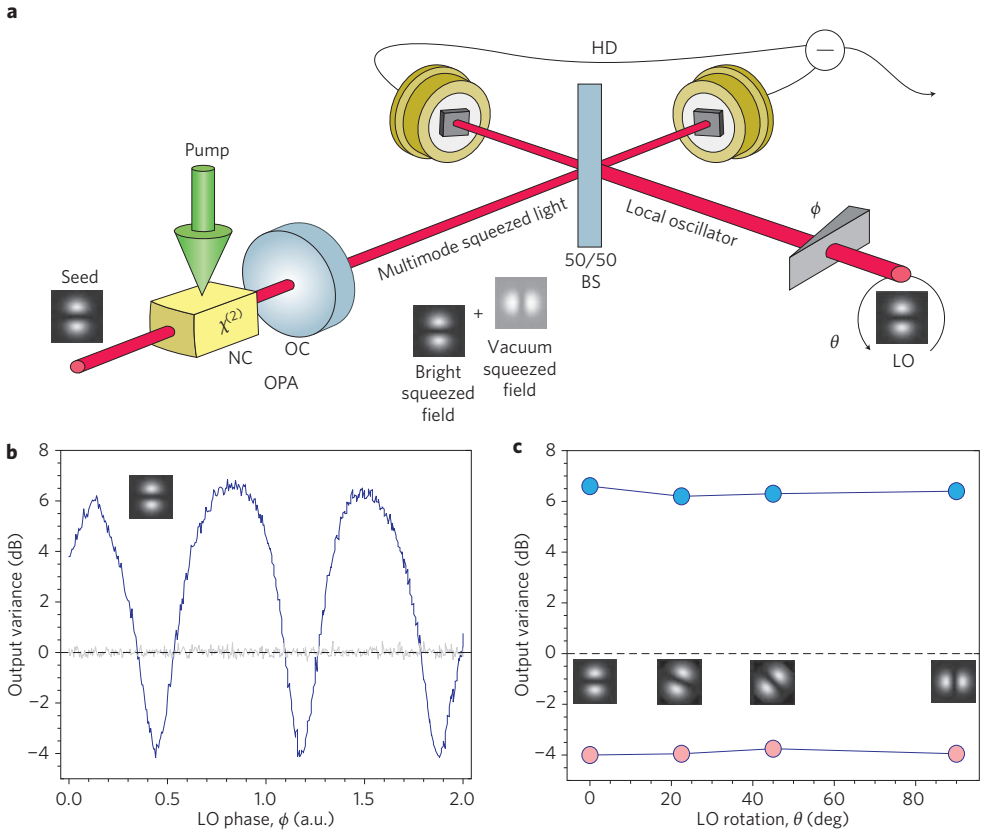


**Figure 1 | Multimode squeezing. a**, Schematic of the squeezing experimental setup. OPA, optical parametric amplifier with its cavity formed by the rear surface of the nonlinear crystal (NC) and an output coupling mirror (OC); BS, beamsplitter; LO, local oscillator; HD, homodyne detection. **b**, Measurement of squeezed field in the $TEM_{01}$ mode and scanning the phase, $\phi$, of the LO. **c**, Measurements of squeezing/antisqueezing when the $TEM_{01}$ LO beam is spatially rotated by $\theta$ along the $x$-axis using a Dove prism.

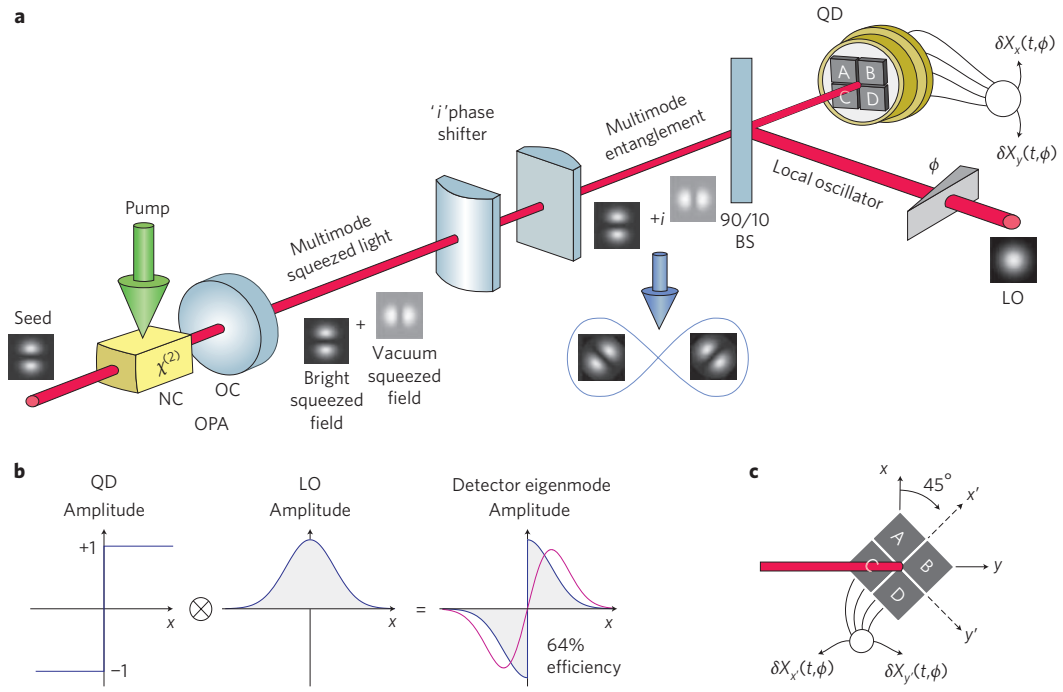


**Figure 2 | Multimode entanglement and detection. a**, Schematic of the experimental setup. $\delta X_x(t, \phi)$ is equivalent to $\delta X_{(A+B)-(C+D)}(t, \phi)$, and $\delta X_y(t, \phi)$ is given by $\delta X_{(A+C)-(B+D)}(t, \phi)$. OPA, optical parametric amplifier; NC, nonlinear crystal; OC, output coupling mirror; BS, beamsplitter; LO, local oscillator; QD, quadrant detector. **b**, Principle of the split-detection technique. The eigenmode of a split-detector is a flipped mode, resulting in 64% detection efficiency in $TEM_{10}$ basis. **c**, A spatial 50/50 beamsplitter is introduced by carrying out a measurement in a 45° rotated basis.

the QD with electronic splitters and using a fast data acquisition system, we are able to measure properties of states in the $TEM_{01}$ mode and $TEM_{10}$ mode simultaneously, using just a single detector and one local oscillator. The temporal fluctuations are directly recorded, and the data is then post-processed. It is filtered for various frequency bands (with a width of 100 kHz), and the correlations and variances are then directly determined from the time-varying data. Such measurements are shown in Fig. 3a at 4.8 MHz detection frequency. Using the quadrant detector we measure −1.7 dB of squeezing in the two modes, which is sufficient for use in a demonstration of entanglement. An interesting feature and limiting factor is the small phase shift, about $\pi/7$, between the two fields, which might have an origin in a small misalignment of the OPA cavity.

There is a well-established set of requirements for entangling two optical beams, and we meet all of these in our unusual setup. A $\pi/2$ (or $i$) phase shift is first required between the two beams, which for standard entanglement is simply a matter of delaying one of the beams with respect to the other. The beams then need to be mixed together, which is generally achieved with a 50/50 beamsplitter. Finally, we need to observe a pair of conjugate observables, which requires a phase-sensitive detector to measure quadrature entanglement. This is usually achieved with one HD on each of the entangled beams.

To induce the $\pi/2$ phase shift we used an elegant optical method using the Gouy phase shift in higher-order modes[25]. The output of the degenerate OPA was mode-matched into a symmetric two cylindrical-lens system (focal lengths $f = 250$ mm, with lens separation of $\sqrt{2}f$), which imparts a $\pi/2$ phase shift on one of the modes, as shown in the comparison of the squeezing results in Fig. 3a and Fig. 3b.

We then need to mix the $TEM_{01}$ and $TEM_{10}$ modes, equivalent to a 50/50 beamsplitter. Any H-G mode can be expressed as a superposition of two orthogonal modes of the same order as the original field. This is analogous to the superposition of polarization modes in a two-dimensional basis. A $TEM_{10}$ mode rotated by $\pm 45^\circ$ relative to the $x$-axis can be expressed as $1/\sqrt{2}(TEM_{10} \pm TEM_{01})$. This means that our 'beamsplitter' can be realized by detecting in a basis that is 45° rotated relative to the axis of the cylindrical-lens system (Fig. 2c), and this is the basis where entanglement then exists. As expected from quantum theory, measurements of the arbitrary quadratures of entangled fields show noisy states (Fig. 3c). These measurements were again carried out with the QD, giving the advantage of being able to measure both modes simultaneously.

With these data we can calculate the inseparability criterion $\mathcal{I}$ (ref. 26), which is a direct measure of entanglement. A value less than one implies that entanglement exists between the two modes, with a perfectly entangled system having a value of zero. With the sum and difference of the signals of the two orthogonal fields, we evaluate the equation $\mathcal{I} = \sqrt{V_{x'+y'}(\phi_0)V_{x'-y'}(\phi_0+\pi/2)}$, where $\phi_0$ is chosen such that $\mathcal{I}$ is minimized, as shown in Fig. 4. This results in a value of $\mathcal{I} = 0.79 \pm 0.02$ at 3.3 MHz detection frequency, after corrections are made for electronic noise. We demonstrate significant entanglement between two orthogonal spatial modes within one optical beam. This entanglement can be enhanced with the use of specially designed multipixel detectors.

In conclusion, we have demonstrated an elegant technique to create and measure entanglement between two orthogonal spatial modes in a single beam of light. We have shown and tested several simplifications on traditional entanglement schemes, including generating two squeezed modes from a single OPA, using imaging components to mix the modes with the correct phase, and detecting the two modes simultaneously with one QD. The results for two modes are similar to those that can be achieved with polarization techniques. However, this technique can be expanded to produce entanglement between any two orthogonal modes of the form $TEM_{jk}$ and $TEM_{kj}$, creating a larger number of quantum channels.

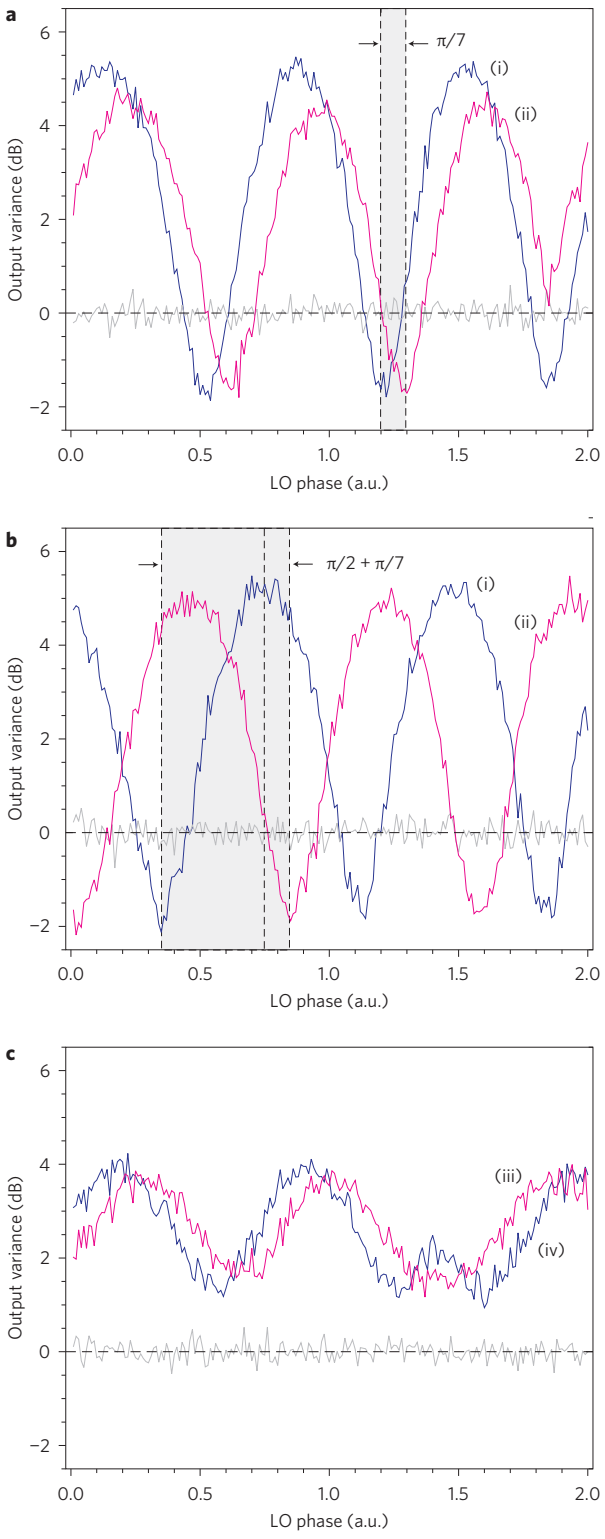


**Figure 3 | Noise measurements. a**, Output variance of the degenerate optical parametric amplifier for the $TEM_{10}$ field, with variance $V_x(\phi)$ (i), and the $TEM_{01}$ field, with variance $V_y(\phi)$ (ii), using a quadrant detector and scanning the local oscillator phase. **b**, The same setup as **a**, but with the cylindrical-lens system included. **c**, Output variances $V_{x'}(\phi)$ (iii) and $V_{y'}(\phi)$ (iv) for the 45° rotated fields using a quadrant detector and scanning the local oscillator phase.

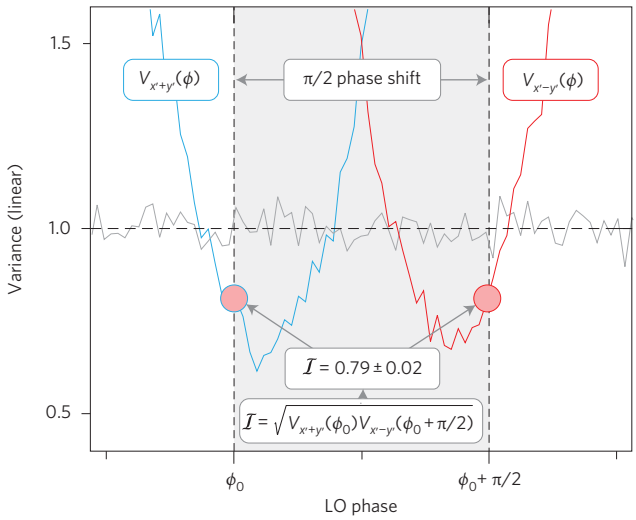


**Figure 4 | Results for inseparability.** Measurement of the variance for the sum $V_{x'+y'}(\phi)$ and difference $V_{x'-y'}(\phi)$ for the 45° rotated fields. The data, both below the quantum noise limit, are combined to one value for the inseparability.

The tools for a multimode system are being developed. We can already synthesize a beam with several higher-order spatial modes from several sources of squeezed light[19]. The mixing and entanglement could be performed for a larger number of modes using imaging techniques, for example, by making use of a programmable spatial light modulator. A single multipixel detector with multiple gain functions applied to match the field amplitude of each orthogonal mode could be used to make simultaneous measurements of all the higher-order spatial modes with one local oscillator. Accessing this expanded basis of quantum information channels within a single beam and the possible manipulation of the modes makes this technology a practical contender for optical multimode quantum communication systems.

Received 28 January 2009; accepted 18 May 2009; published online 21 June 2009

## References


1. Gisin, N. & Thew, R. Quantum communication. *Nature Photon* **1,** 165–171 (2007).
2. Reid, M. D. *et al.* The Einstein–Podolsky–Rosen paradox—a fundamental challenge and a tool for quantum engineering. *Rev. Mod. Phys.* (accepted); <http://arXiv:0806.0270> (2008).
3. Lee, H., Ahn, D. & Hwang, S. W. Dense coding in entangled states. *Phys. Rev. A* **66,** 024304 (2002).
4. Bowen, W. P., Schnabel, R., Lam, P. K. & Ralph, T. C. An experimental investigation of criteria for continuous variable entanglement. *Phys. Rev. Lett.* **90,** 043601 (2003).
5. Yonezawa, H., Aoki, T. & Furusawa, A. Demonstration of a quantum teleportation network for continuous variables. *Nature* **431,** 430–433 (2004).
6. Lance, A. *et al.* Continuous-variable quantum-state sharing via quantum disentanglement. *Phys. Rev. A* **71,** 033814 (2005).
7. Dong, R. *et al.* Experimental entanglement distillation of mesoscopic quantum states. *Nature Phys.* **4,** 919–923 (2008).
8. Hage, B. *et al.* Preparation of distilled and purified continuous-variable entangled states. *Nature Phys.* **4,** 915–918 (2008).
9. Wagner, K. *et al.* Entangling the spatial properties of laser beams. *Science* **321,** 541–543 (2008).
10. Hsu, M. T. L., Bowen, W. P., Treps, N. & Lam, P. K. Continuous-variable spatial entanglement for bright optical beams. *Phys. Rev. A* **72,** 013802 (2005).
11. Delaubert, V. *Quantum Imaging with a Small Number of Transverse Modes.* PhD thesis, ANU, CNRS (2007).
12. Yukawa, M., Ukai, R., van Loock, P. & Furusawa, A. Experimental generation of four-mode continuous-variable cluster states. *Phys. Rev. A* **78,** 012301 (2008).
13. Su, X. *et al.* Experimental preparation of quadripartite cluster and Greenberger–Horne–Zeilinger entangled states for continuous variables. *Phys. Rev. Lett.* **98,** 070502 (2007).
14. Menicucci, N. C., Flammia, S. T., Zaidi, H. & Pfister, O. Ultracompact generation of continuous-variable cluster states. *Phys. Rev. A* **76,** 010302 (2007).
15. Huntington, E. H., Milford, G. N., Robilliard, C. & Ralph, T. C. Coherent analysis of quantum optical sideband modes. *Opt. Lett.* **30,** 2481–2483 (2005).
16. de Valcarcel, G. J., Patera, G., Treps, N. & Fabre, C. Multimode squeezing of frequency combs. *Phys. Rev. A* **74,** 061801 (2006).
17. Lassen, M. *et al.* Generation of squeezing in higher order Hermite–Gaussian modes with an optical parametric amplifier. *J. Eur. Opt. Soc.* **1,** 06003 (2006).
18. Treps, N. *et al.* Surpassing the standard quantum limit for optical imaging using nonclassical multimode light. *Phys. Rev. Lett.* **88,** 203601 (2002).
19. Lassen, M. *et al.* Tools for spatial multi-mode quantum information: modulation, detection and quantum correlations. *Phys. Rev. Lett.* **98,** 083602 (2007).
20. Beck, M. Quantum state tomography with array detectors. *Phys. Rev. Lett.* **84,** 5748–5751 (2000).
21. Lugiato, L. A. & Gatti, A. Spatial structure of a squeezed vacuum. *Phys. Rev. Lett.* **70,** 3868–3871 (1993).
22. Janousek, J. *Investigation of Non-classical Light and its Application in Ultrasensitive Measurements.* PhD thesis, DTU (2007).
23. Hsu, M. T. L., Bowen, W. P. & Lam, P. K. Spatial-state Stokes-operator squeezing and entanglement for optical beams. *Phys. Rev. A* **79,** 043825 (2009).
24. Lassen, M., Leuchs, G. & Andersen, U. L. Continuous variable entanglement and squeezing of orbital angular momentum states. *Phys. Rev. Lett.* **102,** 163602 (2009).
25. Siegman, A. *Lasers* (University Science, 1986).
26. Duan, L.-M., Giedke, G., Cirac, J. I. & Zoller, P. Inseparability criterion for continuous variable systems. *Phys. Rev. Lett.* **84,** 2722–2725 (2000).


## Acknowledgements

We would like to thank A. Dreau for her contributions to the design of the data aquisition system. This work was funded by the Centre of Excellence program of the Australian Research Council. It was supported by the ANU, CNRS and the Ecole Normale Superieur, Paris. We acknowledge the financial support of the Future and Emerging Technologies (FET) programme within the Seventh Framework Programme for Research of the European Commission, under the FET-Open grant agreement HIDEAS, number FP7-ICT-221906.

## Additional information

Reprints and permission information is available online at http://npg.nature.com/reprintsandpermissions/. Correspondence and requests for materials should be addressed to J.J.

nature photonics

LETTERS

PUBLISHED ONLINE: 21 JUNE 2009 | DOI: 10.1038/NPHOTON.2009.99

# Voltage-programmable liquid optical interface

C. V. Brown*, G. G. Wells, M. I. Newton and G. McHale

**Recently, there has been intense interest in photonic devices based on microfluidics, including displays[1,2] and refractive tunable microlenses and optical beamsteerers[3–5] that work using the principle of electrowetting[6,7]. Here, we report a novel approach to optical devices in which static wrinkles are produced at the surface of a thin film of oil as a result of dielectrophoretic forces[8–10]. We have demonstrated this voltage-programmable surface wrinkling effect in periodic devices with pitch lengths of between 20 and 240 μm and with response times of less than 40 μs. By a careful choice of oils, it is possible to optimize either for high-amplitude sinusoidal wrinkles at micrometre-scale pitches or more complex non-sinusoidal profiles with higher Fourier components at longer pitches. This opens up the possibility of developing rapidly responsive voltage-programmable, polarization-insensitive transmission and reflection diffraction devices and arbitrary surface profile optical devices.**

The device structure is shown in Fig. 1. The side view (Fig. 1a) shows the glass substrate coated with patterned gold/titanium conducting electrodes, on the top of which there is a thin solid dielectric layer (either photoresist or a dielectric stack), upon which is coated a thin layer of oil. The electrodes were arranged as an array of stripes parallel to the $y$-direction in the $xy$-plane. This geometry allowed every other electrode to be electrically connected as shown in the plan view in Fig. 1b.

Electrically induced wrinkling at the oil surface will be considered first for a device with an electrode pitch $p$ of 80 μm. When a small volume (0.1 μl) of 1-decanol was initially dispensed onto the device it formed a spherical cap with a contact angle of 5°. Every other stripe in the electrode array was biased with an a.c. voltage of magnitude $V_0$ (r.m.s.) and the interdigitated stripes between them were earthed as shown in Fig. 1. This created a highly non-uniform, periodic electric field profile in the plane of the oil layer. A polarizable dielectric material in a region containing non-uniform electric fields experiences a force (known as a dielectrophoretic force) in the direction of the increase in magnitude of the electric field[8–10]. When the r.m.s. electrode voltage was greater than $V_0 = 20$ V the dielectrophoretic forces spread the oil into a thin film of uniform thickness $\bar{h} = 12$ μm, across the area covered by the electrodes.

Increasing the voltage between neighbouring electrodes gave rise to a periodic undulation at the surface of the oil. The period of the wrinkle was equal to the electrode pitch, 80 μm, and the peaks and troughs of the wrinkle lay parallel to the electrode fingers along the $y$-direction. This undulation arises because the highest electric field gradients occur in the gaps between the electrodes and so the dielectrophoretic forces in these regions cause the oil to collect there preferentially. The interdigitated electrode geometry is commonly used in biological particle manipulation[9,11] but dielectrophoretic actuation in fluids has previously been limited to nanodroplet formation and lab-on-a-chip applications[12].

The wrinkle at the oil–air interface and the associated periodic variation in the optical path for light travelling through the

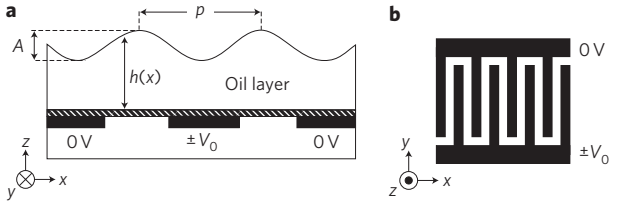


**Figure 1 | Structure of the device. a**, Side view. A thin layer of oil coats a dielectric layer (shown cross-hatched), which has been deposited onto a glass substrate containing an array of gold/titanium interdigitated striped electrodes (shown by the black electrodes). **b**, Plan view of the interdigitated electrode geometry.

film has been directly visualized here using a Mach–Zehnder interferometer[13]. The device was illuminated in transmission mode with He–Ne laser light at a wavelength of 633 nm. One of the mirrors of the interferometer was tilted to produce parallel intensity interference fringes localized at the position of the oil layer. The individual interference fringes were oriented parallel to the $x$-direction and a periodic change in the oil thickness $h(x)$ caused a directly proportionate periodic shift of the fringes in the $y$-direction. The interferograms shown as insets in Fig. 2 show the fringe patterns when voltages (20 kHz a.c.) of $V_0 = 80$ V (top left inset) and $V_0 = 160$ V (top right inset) were applied between adjacent in-plane electrodes.

Knowledge of the refractive index of the oil ($n_{oil} = 1.438$ for 1-decanol, ref. 14) allowed the peak-to-peak amplitude $A$ of the wrinkle at the oil–water interface to be calculated directly from the interferometer fringe patterns. The results are shown as filled circles in Fig. 2, where the square of the r.m.s. amplitude of the applied voltage is plotted as the abcissae. The solid line shows the linear regression fit to the data: $A = (5.107 \times 10^{-5})\, V_0^2 + 0.118$, in micrometres.

Under an applied periodic potential the appearance of the wrinkle at the oil–air interface decreases the dielectric energy of the system, but this in turn causes an increase in the area of the oil–water interface. The interfacial surface tension provides a restorative force that resists the undulation deformation on the spread oil film. The observed dependence on the square of the voltage is reproduced by a simple calculation using the following approximations: (i) the wrinkle amplitude is small ($A \ll p$); (ii) the periodic potential profile due to the electrodes, $V(x, y)$, is described by a Fourier series expansion to second order only; and (iii) the potential profile is unperturbed by the presence of the oil–air interface. Equating and minimizing the sum of the electrostatic and surface tension energies with respect to the peak-to-peak amplitude $A$ of the wrinkle yields equation (1):

$$A = \left[\frac{16\varepsilon_0}{3\gamma\pi^4}(\varepsilon_{oil} - \varepsilon_{air})\exp\left(-\frac{4\pi\bar{h}}{p}\right)\right]V_0^2 \qquad (1)$$

School of Science and Technology, Nottingham Trent University, Clifton Lane, Nottingham, NG11 8NS, UK. *e-mail: carl.brown@ntu.ac.uk

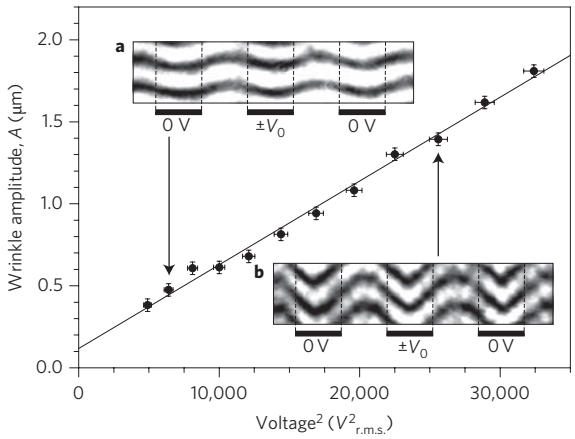


**Figure 2 | Plot of the peak-to-peak amplitude *A* of the wrinkle at the oil–air interface and interferograms at different voltages.** The insets present interferograms showing periodic displacements of tilt fringes at a wavelength of 633 nm (0.61 mW cm$^{-2}$ at device) in a Mach–Zehnder interferometer. These fringe patterns were produced by a layer of 1-decanol oil coating a device with a dielectric stack of thickness 1.13 μm (see Supplementary information) with voltages (r.m.s. 20 kHz a.c.) of 80 V (top-left inset) and 160 V (bottom-right inset). The electrode (and wrinkle) pitch was 80 μm. The peak-to-peak amplitude *A* of the wrinkle at the oil–air interface was obtained from the interferometer fringe patterns and is plotted against the square of the a.c. voltage, $V_0^2$.

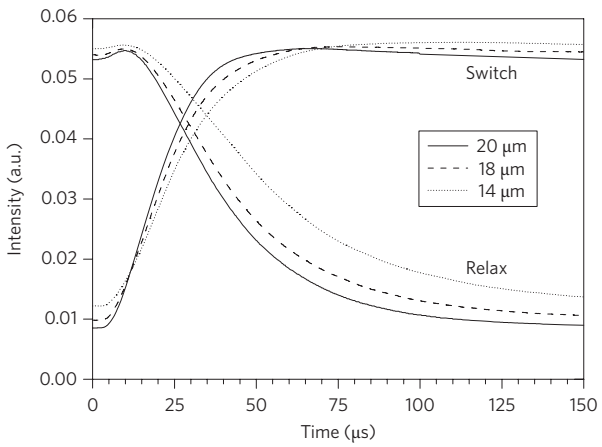


**Figure 3 | Transient response of the intensity of the reflection mode first diffracted order as a function of time.** Data were taken at a wavelength of 543 nm (0.08 W cm$^{-2}$) after a wrinkle of amplitude $A = 0.36$ μm at the surface of 1-decanol was turned on ('Switch') or off ('Relax') at time 0 μs. Measurements are shown for oil layers of three different thicknesses coating the same device as used in Fig. 2, for which the pitch was $p = 80$ μm.

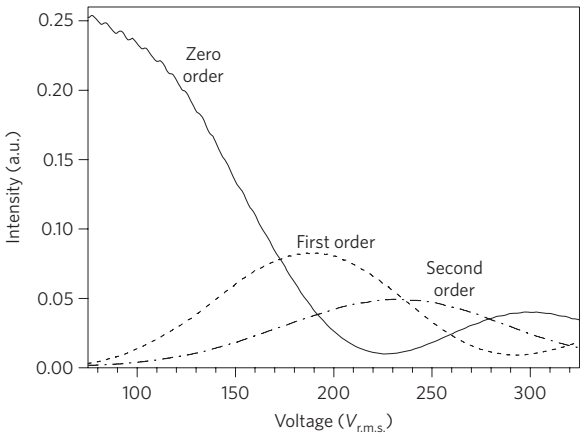


**Figure 4 | Intensity of the zero-, first- and second-order peaks due to the diffraction of light at 543 nm.** Intensities of the transmitted diffracted orders at 543 nm (0.08 W cm$^{-2}$) are shown for a film of 1-decanol with average thickness $\bar{h} = 3$ μm as a function of the magnitude of the voltage (20 kHz a.c.) applied between adjacent in-plane electrodes. The orders were observed at angles of 0° (zero), 1.56° (+1) and 3.11° (+2). For this device the dielectric layer was 2 μm thick and was fabricated from SU-8 photoresist (see Supplementary information), and the electrode pitch was $p = 20$ μm, which also corresponded to the wrinkle pitch.

This reproduces the intuitive result that, at a particular voltage, higher wrinkle amplitudes will result from using oil with a higher dielectric constant and lower surface tension. Substituting the values from the linear regression fit to the data in Fig. 2 and the values of $\varepsilon_{oil} = 8.1$ and $\gamma = 28.4$ mN m$^{-1}$ (ref. 14) for the dielectric constant and surface tension of 1-decanol into equation (1) yields $\bar{h} = 5.5$ μm. This is the correct order of magnitude but lower than the average thickness of $\bar{h} = 12$ μm estimated from the fringe pattern at the edge of the spread film (see Supplementary information).

The switching speed was measured by monitoring the time-dependent intensity of the reflection mode first-order diffraction peak in response to a sudden change in the amplitude of the voltage $V_0$. The device was illuminated in reflection with laser light at a wavelength of 543 nm and the applied voltage (20 kHz a.c. square-wave) was discontinuously switched between a low value, $V_0 = 10$ V, and a high value every 5 ms. The low value was just sufficient to maintain the uniformity of the oil coating. The high value of the voltage was adjusted to achieve a peak in the intensity of the first diffracted order for each particular oil film thickness. For the three different thicknesses $\bar{h} = 20$, 18 and 14 μm, the r.m.s. amplitudes of the high voltages were $V_0 = 93$, 90 and 86 V, respectively. From simultaneous transmission measurements of the high-voltage fringe displacements on the Mach–Zehnder interferometer this was found to correspond to a wrinkle of amplitude $A = 0.36$ μm for all cases. Data are shown in Fig. 3 for the low to high voltage transition labelled 'Switch', and for the high to low voltage transition labelled 'Relax'. The times for the intensity to change from the value at 0 μs to 90% of the difference between the initial and asymptotic intensities were 35, 40, 49 μs (switching) and 79, 89, 108 μs (relaxing) for $\bar{h} = 20$, 18 and 14 μm, respectively.

An amplitude-programmable phase diffraction grating[15] has been demonstrated in transmission mode using wrinkles with a shorter pitch of $p = 20$ μm in a film of 1-decanol oil having an average thickness of $\bar{h} = 3$ μm. Figure 4 shows the intensities of the zero-, first- and second-order peaks due to the diffraction of light at 543 nm transmitted through the film with its periodic surface wrinkle as a function of the voltage $V_0$ (20 kHz a.c.) (see also Supplementary information).

The ratio of the peak intensity in the first order to the zero-order peak intensity at low voltage is 32.6%. This is close to the value of 33.8% that would be predicted by the Fraunhofer approximation for a 'thin sinusoidal phase grating'[16].

Still shorter pitches on the scale of micrometres or lower appear feasible, but there are technological challenges in creating a sufficiently thin film of oil. Still higher diffraction efficiencies may be possible by making the fluid surface (rather than the substrate) fully reflective[17,18]. It is also possible that the surface wrinkle could be produced at the interface between two density-matched liquids, for example, a high-refractive-index oil and water, in an encapsulated device that could be used in any orientation[3] (see Supplementary information).

Figure 5 shows oil film surface shapes that are more interesting than the simple sinusoidal profiles that have been discussed above. Each of

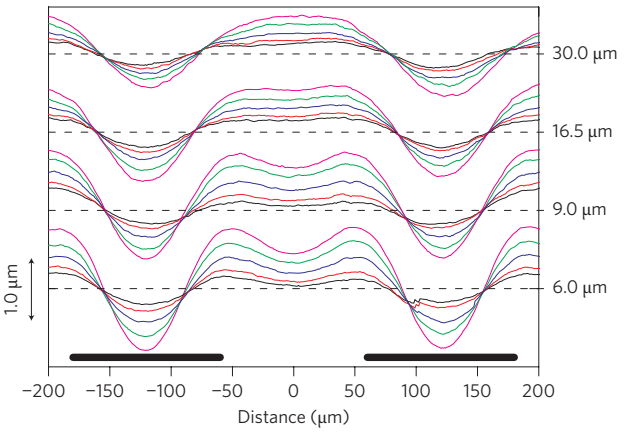


**Figure 5 | Profiles at a hexadecane oil–air interface that have been created by the action of a non-uniform electric field profile.** The profiles were measured using a Mach–Zehnder interferometer (633 nm and 0.61 mW cm$^{-2}$ at the device). Oil films with four different thicknesses were used, $\bar{h}$ = 6.0, 9.0, 16.5 and 30.0 μm, as indicated by the dotted lines. At each different thickness the profiles obtained with different applied voltages are shown by solid lines of different colours: $V_{r.m.s.}$ = 275 V (black), 325 V (red), 400 V (blue), 475 V (green) and 550 V (magenta). For this device the dielectric layer was 2 μm thick and was fabricated from SU-8 photoresist (see Supplementary information), and the electrode pitch was $p$ = 240 μm, which also corresponded to the wrinkle pitch. The positions of the electrodes are shown by the black lines at the bottom of the figure. The vertical scale is the same for each profile, but the profiles at different thicknesses have been displaced vertically for clarity.

the solid lines shows an individual surface profile that has been created for a particular voltage (represented using different colours) and for a particular average oil film thickness (shown by the horizontal dotted line on which it lies). By using oil with a lower dielectric constant (hexadecane, $\varepsilon_{oil}$ = 2.05), combined with a longer electrode pitch ($p$ = 240 μm), it has been possible to program non-sinusoidal profiles and so switch on other Fourier components with higher spatial frequencies. These higher Fourier components are most prominent at the lowest film thickness, $\bar{h}$ = 6.0 μm, where the surface of the oil film lies closer to the highly non-uniform fringing electric fields at the electrode edges.

In conclusion, we have presented a new and potentially versatile concept of using dielectrophoretic forces to create fluid-based optical switching devices. As an example photonic device application we have demonstrated a switchable phase diffraction grating where the intensity modulation of the undeviated zero order, as well as the diffracted orders, are intrinsically polarization insensitive; the zero- and first-order intensities can be fully modulated at speeds below 40 μs. The voltage-programmable optical effect uses a straightforward device structure and is static, reproducible and stable[19–21] when switched on. This combination of properties in a single device is significant compared with existing technologies based on, for example, birefringent liquid crystals[22,23], electro-optic or acousto-optic modulators[24,25], or deformable polymer layers[26]. Our further demonstration of more complex non-sinusoidal surface wrinkle profiles suggests the possibility of producing aperiodic or arbitrary surface profiles using independently addressable electrodes for application in two-dimensional spatial light modulator arrays.

Videos showing the modulation of the diffraction pattern in response to a slowly ramping voltage (i) in transmission mode using the 20-μm pitch, and (ii) in reflection mode using the 80-μm pitch are available as Supplementary Information. The Supplementary Information also provides additional experimental details and discussion of equation (1).

Received 22 March 2009; accepted 21 May 2009; published online 21 June 2009

## References

1. Hayes, R. A. & Feenstra, B. J. Video-speed electronic paper based on electrowetting. *Nature* **425,** 383–385 (2003).
2. Heikenfeld, J. & Steckl, A. J. High-transmission electrowetting light valves. *Appl. Phys. Lett.* **86,** 151121 (2005).
3. Berge, B. & Peseux, J. Variable focal lens controlled by an external voltage: An application of electrowetting. *Euro. Phys. J. E* **3,** 159–163 (2000).
4. Kuiper, S. & Hendriks, B. H. W. Variable-focus liquid lens for miniature cameras. *Appl. Phys. Lett.* **85,** 1128–1130 (2004).
5. Smith, N. R., Abeysinghe, D. C., Haus, J. W. & Heikenfeld, J. Agile wide-angle beam steering with electrowetting microprisms. *Opt. Express* **14,** 6557–6563 (2006).
6. de Gennes, P. G. Wetting: statics and dynamics. *Rev. Mod. Phys.* **57,** 827–862 (1985).
7. Mugele, F. & Baret, J. C. Electrowetting: from basics to applications. *J. Phys. Condens. Matter* **17,** R705–R774 (2005).
8. Pellat, H. Mésure de la force agissant sur les diélectriques liquides non électrisés placés dans un champ électrique. *C. R. Acad. Sci. Paris* **119,** 691–694 (1895).
9. Pohl, H. A. *Dielectrophoresis: The Behaviour of Neutral Matter in Non-Uniform Electric Fields, Cambridge Monographs on Physics* (Cambridge Univ. Press, 1978).
10. Lorrain, P. & Corson, D. R. *Electromagnetic Fields and Waves* 2nd edn (W. H. Freeman, 1970).
11. Pethig, R. Using inhomogeneous a.c. electrical fields to separate and manipulate cells. *Crit. Rev. Biotech.* **16,** 331–348 (1996).
12. Jones, T. B., Gunjii, M., Washizu, M. & Feldman, M. J. Dielectrophoretic liquid actuation and nanodroplet formation. *J. Appl. Phys.* **89,** 1441–1448 (2001).
13. Born, M. & Wolf, E. *Principles of Optics* 7th edn (Cambridge Univ. Press, 2005).
14. *Knovel Critical Tables* 2nd edn (Knovel, 2003).
15. Hutley, M. C. *Diffraction Gratings* (Academic Press, 1982).
16. Goodman, J. W. *Introduction to Fourier Optics* 2nd edn (McGraw-Hill, 1996).
17. Hubert, H. & Girault, H. H. Electrowetting: shake, rattle and roll. *Nature Mater.* **5,** 851–852 (2006).
18. Bucaro, M. A., Kolodner, P. R., Taylor, J. A., Sidorenko, A., Aizenberg, J. & Krupenkin, T. N. Tunable liquid optics: electrowetting-controlled liquid mirrors based on self-assembled janus tiles. *Langmuir* **25,** 3876–3879 (2009).
19. Herminghaus, S. Dynamical instability of thin liquid films between conducting media. *Phys. Rev. Lett.* **83,** 2359–2361 (1999).
20. Schäffer, E., Thurn-Albrecht, T., Russell, T. P. & Steiner, U. Electrically induced structure formation and pattern transfer. *Nature* **403,** 874–877 (2000).
21. Staicu, A. & Mugele, F. Electrowetting-induced oil film entrapment and instability. *Phys. Rev. Lett.* **97,** 167801 (2006).
22. Komanduri, R. K., Chulwoo, O. & Escuti, M. J. Reflective liquid crystal polarization gratings with high efficiency and small pitch, in *Liquid Crystals XII* (ed. Khoo, Iam Choon) *Proc. SPIE*, **7050,** 70500J (2008).
23. De La Tocnaye, J. L. D. Engineering liquid crystals for optimal uses in optical communication systems. *Liq. Cryst.* **31,** 241–269 (2004).
24. Eldada, L. Optical communication components. *Rev. Sci. Instrum.* **75,** 575–593 (2004).
25. Mias, S. & Camon, H. A review of active optical devices: I. Amplitude modulation. *J. Micromech. Microeng.* **18,** 083001 (2008).
26. Bowden, N., Brittain, S., Evans, A. G., Hutchinson, J. W. & Whitesides, G. M. Spontaneous formation of ordered structures in thin films of metals supported on an elastomeric polymer. *Nature* **393,** 146–149 (1998).

## Acknowledgements

The authors gratefully acknowledge J. Fyson at Kodak (European Research) Ltd and N. J. Shirtcliffe and C. L. Trabi at Nottingham Trent University for fruitful discussions. G.W. gratefully acknowledges The EPSRC/DTI COMIT Faraday Partnership and Kodak (European Research) Ltd for funding.

## Author contributions

C.V.B., M.I.N. and G.M. conceived the concept and planning. C.V.B., G.G.W. and M.I.N. designed the experiment. C.V.B. and G.M. carried out theoretical work. C.V.B. wrote the paper and G.G.W. performed the experimental work and data analysis.

## Additional information

Supplementary information accompanies this paper at www.nature.com/naturephotonics. Reprints and permission information is available online at http://npg.nature.com/reprintsandpermissions/. Correspondence and requests for materials should be addressed to C.V.B.

ARTICLES
PUBLISHED ONLINE: 21 JUNE 2009 | DOI: 10.1038/NPHOTON.2009.96
nature photonics

# Increased light harvesting in dye-sensitized solar cells with energy relay dyes

Brian E. Hardin[1,2], Eric T. Hoke[1], Paul B. Armstrong[3], Jun-Ho Yum[2], Pascal Comte[2], Tomás Torres[4], Jean M. J. Fréchet[3], Md Khaja Nazeeruddin[2], Michael Grätzel[2] and Michael D. McGehee[1]*

**Conventional dye-sensitized solar cells have excellent charge collection efficiencies, high open-circuit voltages and good fill factors. However, dye-sensitized solar cells do not completely absorb all of the photons from the visible and near-infrared domain and consequently have lower short-circuit photocurrent densities than inorganic photovoltaic devices. Here, we present a new design where high-energy photons are absorbed by highly photoluminescent chromophores unattached to the titania and undergo Förster resonant energy transfer to the sensitizing dye. This novel architecture allows for broader spectral absorption, an increase in dye loading, and relaxes the design requirements for the sensitizing dye. We demonstrate a 26% increase in power conversion efficiency when using an energy relay dye (PTCDI) with an organic sensitizing dye (TT1). We estimate the average excitation transfer efficiency in this system to be at least 47%. This system offers a viable pathway to develop more efficient dye-sensitized solar cells.**

Dye-sensitized solar cells (DSCs) work on the basis of light harvesting using a sensitizing dye (SD) attached to a wide-bandgap semiconductor[1–5]. DSCs are composed mainly of abundant, non-toxic materials and offer an inexpensive route to the development of highly efficient photovoltaic cells. State-of-the-art DSCs, which absorb light from 350 to 700 nm, have validated power conversion efficiencies of over 11% (ref. 6). A key to improving the efficiency of DSCs is to increase their spectral absorption range. To reach power conversion efficiencies of 15% using an $I^-/I_3^-$ redox couple, DSCs must absorb ~80% of the solar spectrum from 350 to 900 nm (ref. 7). Light absorption in DSCs is determined by the molar extinction coefficient of the SD, the surface coverage of the dye (dye molecules $nm^{-2}$), and the total surface area of the oxide film[8]. Films comprising $TiO_2$ nanoparticles enhance the surface area; 10-μm-thick films have surface areas ×1,000 greater than that of a flat junction. SDs generally pack tightly on the $TiO_2$ surface with a density of 0.5–1 dye molecules $nm^{-2}$ (ref. 8). The SD has traditionally been made from ruthenium-based complexes (for example, N719 and Z907)[6,9] that have fairly broad absorption spectra ($\Delta\lambda \approx 350$ nm) but low molar extinction coefficients (5,000–20,000 $M^{-1}\,cm^{-1}$). Organic dyes have recently been developed with substantially higher molar extinction coefficients (50,000–200,000 $M^{-1}\,cm^{-1}$) but narrow spectral bandwidths ($\Delta\lambda \approx 250$ nm)[10–13]. As a general rule, dyes that absorb strongly do not typically exhibit broad absorption.

Co-sensitization of titania by dyes with complimentary absorption spectra has been demonstrated to enhance light absorption and broaden the spectral response of organic DSCs (ref. 14). However, the limited number of sites on the titania surface to which dye molecules attach places a constraint on the light absorption achievable by co-sensitization. Furthermore, co-sensitization requires that each dye adsorb strongly on the surface, transfer charge efficiently into the $TiO_2$ (refs 15–18), have slow recombination (that is, in the millisecond time domain)[17,19–21], and regenerate with the redox couple[22]. Few dyes exist that are both excellent absorbers and possess the requisite energy levels and chemical anchoring groups to be good SDs. A recent study has demonstrated the use of Förster resonant energy transfer (FRET) between covalently linked energy donor molecules to the SD attached on the titania surface[23]. Siegers and colleagues[23] were able to demonstrate a high excitation transfer efficiency (>89%) between attached dye molecules and an improvement in the device external quantum efficiency of 5–10% between 400 and 500 nm. However, the overall power conversion efficiency enhancement of the DSC was low (<9%) and linked more to an increase in the open-circuit voltage rather than an increase in the short-circuit photocurrent density.

In this Article we demonstrate that unattached, highly luminescent chromophores (PTCDI) inside the liquid electrolyte can absorb high-energy photons and efficiently transfer the energy to the anchored near-infrared sensitizing zinc phthalocyanine dye (TT1), increasing the absorption bandwidth of the DSC. Figure 1 shows two routes for charge generation incorporated in this system. In typical DSCs, light is absorbed by the SD (1), which transfers an electron into the titania and a hole into the electrolyte. In the new design, the unattached energy relay dye (ERD) is excited by higher energy (blue) photons and then undergoes Förster energy transfer (2) to the SD. This design is analogous to photosynthesis in purple bacteria, where an aggregate of light-harvesting pigments transfer their energy to the reaction centre, initiating charge separation[24]. In particular, the pigment LH-II is not in direct contact with the reaction centre, and transfers its excitation by means of an intermediate pigment (LH-I) in under 100 ps with ~95% efficiency[25,26].

We recently proposed using unattached ERDs and long-range energy transfer to increase light absorption[27]. Placing the ERDs inside the electrolyte has several important advantages. First, because the attached dye only has to absorb light over a smaller spectral region, it can be chosen to have a stronger and narrower

[1]Department of Material Science and Engineering, Stanford University, Stanford, California, 94305-4045, USA, [2]Laboratoire de Photonique et Interfaces, École Polytechnique Fédérale de Lausanne, CH-1015, Lausanne, Switzerland, [3]Department of Chemistry, University of California, Berkeley, California 94720-1460, USA, [4]Departamento de Química Orgánica (C-I) and Departamento de Física de Materiales (C-IV), Facultad de Ciencias, Universidad Autónoma de Madrid, Cantoblanco, 28049 Madrid, Spain. *e-mail: mmcgehee@stanford.edu

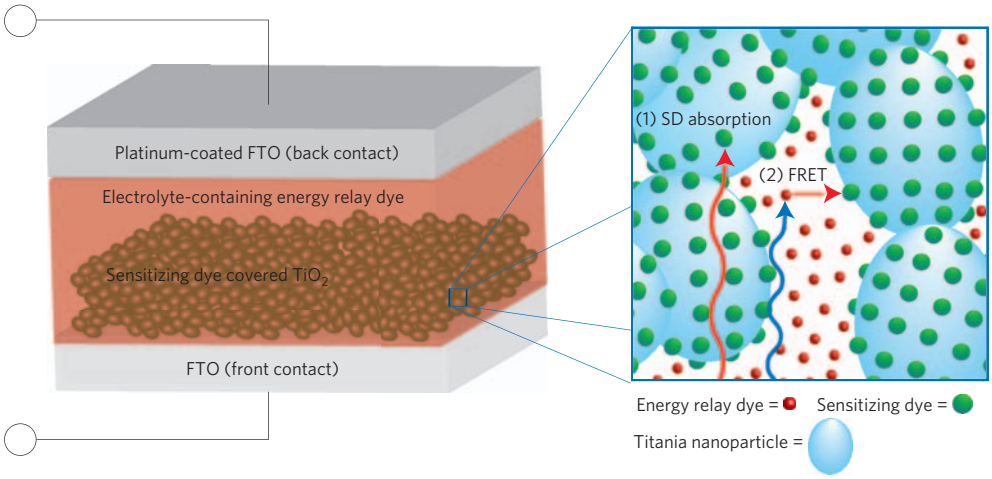


**Figure 1 | Schematic representation of a dye-sensitized solar cell (DSC) with energy relay dyes (ERDs).** The right side of the figure shows the typical absorption process for lower energy (red) photons in the DSC: light is absorbed by the sensitizing dye (1), transferring an electron into the titania, and a hole is transported to the back contact through the electrolyte. The ERD process is similar, except that higher energy (blue) photons are first absorbed by the ERD, which undergoes Förster energy transfer (2) to the sensitizing dye (SD).

absorption spectrum. Second, the SD can be redshifted compared to the commonly used dyes because the ERD can absorb higher energy photons. Furthermore, it is possible to place multiple ERDs with complementary absorption spectra to tailor light absorption inside the device. Finally, the ERD does not need to be attached to the titania surface and with no additional processing steps can be mixed in very large concentrations inside the electrolyte. In summary, the addition of ERDs into the electrolyte makes the overall absorption spectrum wider and stronger for the same film thickness. It is important to note that the ERDs do not participate in the charge transfer or collection process and thus do not require precise energy levels or specialized attachment groups[28]. ERDs should be designed to be soluble in and not greatly quenched by the electrolyte. The ERD concept is particularly applicable to solid-state DSCs (refs 3,29,30), which are currently restricted to a thickness of 2 μm and are not able to absorb all of the light, even at the peak of the dyes' absorption spectrum. Incorporating long-range energy transfer into the solid-state DSC will require ERDs that avoid charge transfer into the hole transporter. The ERD system is also extremely useful for nanostructured systems (for example, $TiO_2$ nanotubes[31], ZnO nanorods[32]) that have less available surface area and thus poorer light absorption.

FRET involves dipole–dipole coupling of two chromophores, known as the donor and acceptor, through an electric field[33]. An excitation of the donor, or in our case the ERD, can be transferred non-radiatively through the field to the acceptor, or SD, if there is overlap between the emission spectrum of the donor and the absorption spectrum of the acceptor. Efficient energy transfer over 3–8 nm can be achieved with strong spectral overlap and high donor emission efficiencies, for an isotropic alignment between individual chromophores in solution. If, however, the single acceptor chromophore is replaced by a dense two-dimensional array (that is, SDs tightly packed on the titania surface) FRET can become efficient well over 25 nm from the interface[34,35].

High FRET transfer rates ($k_{FRET}$) are essential to quickly transfer the energy before the excited ERD non-radiatively decays. The FRET rate is dependent upon the Förster radius ($R_o$) between the ERD and the SD, the separation distance between the ERD and the SD/$TiO_2$ interface, which is a function of pore size and geometry, and the natural fluorescence decay rate of the ERD, $k_0 = 1/\tau_0$. The Förster radius, or the distance in which Förster energy transfer is 50% probable between individual chromophores, can be calculated[33] using equation (1):

$$R_o^6 = \frac{9000 \cdot \ln(10)\kappa^2 Q_D}{128 \cdot \pi^5 n^4 N_A} \int F_D(\lambda)\varepsilon_A(\lambda)\lambda^4 \, d\lambda \qquad (1)$$

where $n$ is the index of refraction of the host medium (1.4–1.5 for the DSC electrolyte), $\kappa^2$ the orientational factor (2/3 for random orientation), $N_A$ Avogadro's number, $Q_D$ the photoluminescence (PL) efficiency, $F_D$ the emission profile of the donor and $\epsilon(\lambda)$ is the molar extinction coefficient.

A previously reported[36] derivative of perylene-3,4,9,10-tetracarboxylic diimide (PTCDI; Fig. 2b) was synthesized (see Methods) for use as an ERD. PTCDI is an ideal ERD candidate because of its extremely high PL efficiency (>90%), fast fluorescence lifetime (4.8 ns), excellent photo and air stability and relatively strong absorption coefficient (50,000 $M^{-1}$ $cm^{-1}$ at 580 nm)[37] . Its bulky alkyl phenyl substituents were designed to reduce chromophore interactions between adjacent dye molecules in order to prevent aggregate formation and reduction of fluorescence. A zinc phthalocyanine dye (TT1; Fig. 2c) was chosen as the SD for its high molar extinction coefficient of 191,500 $M^{-1}$ $cm^{-1}$ centred at 680 nm (ref. 14). One would prefer a dye with a smaller energy gap, but such dyes are not readily available yet with the necessary anchoring groups. When attached to titania, the TT1 dye absorption broadens (as shown in Fig. 2a) and significantly overlaps the PL emission of the PTCDI. Given the absorption and emission profile of the TT1 and PTCDI, respectively, the Förster radius is estimated to be 8.0 nm. Time-resolved PL measurements on solutions with varying concentration of TT1 determined $R_o$ to be 7.5–7.6 nm (see Supplementary Fig. S1).

Once excited, the ERD can transfer its energy to the SD by means of FRET, emit a photon or non-radiatively decay. Non-radiative decay in the DSC system is greatly increased due to the presence of triiodide in the electrolyte. Triiodide is a highly mobile ion that is known as a 'perfect quencher', meaning that collisions with the ERD have a near unity probability of quenching the excited state[38]. Given the high concentrations of triiodide in the DSC electrolyte, the quenching rate of chromophores can be 20–2,000 times greater than the natural decay rate. Collisional quenching of the PTCDI by triiodide is described by the Stern–Volmer equation (2) (refs 39,40),

$$\frac{PL_0}{PL} = \frac{\tau_0}{\tau} = 1 + k_q \tau_0 [Q] \qquad (2)$$

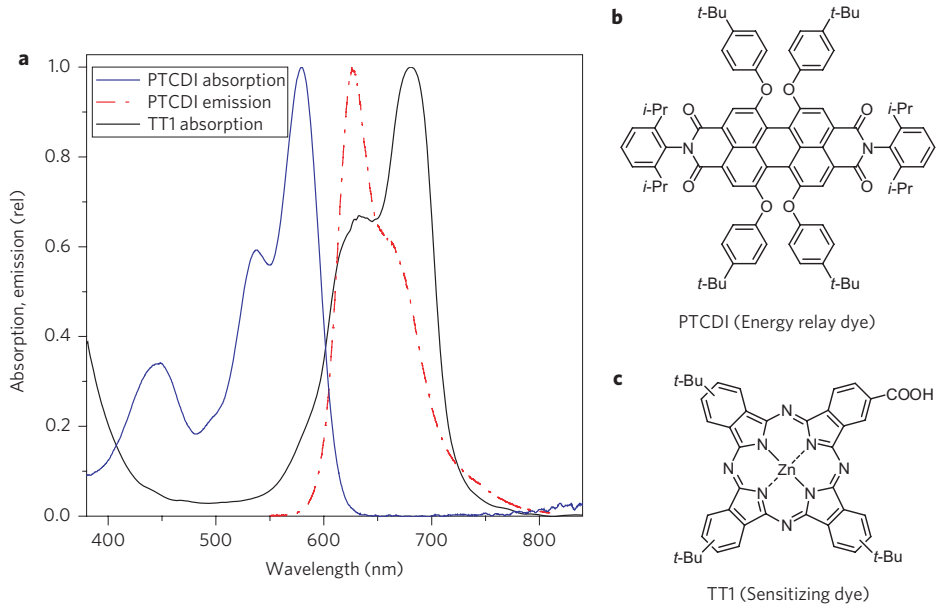


**Figure 2 | PTCDI and TT1 properties. a**, PTCDI absorption (blue), PTCDI emission (red) in chloroform and TT1 absorption (black) on titania nanoparticles. **b**,**c**, Chemical structures of the energy relay dye PTCDI (**b**), and sensitizing dye TT1 (**c**).

where $PL_0$ is the photoluminescence in the absence of a quencher, PL the photoluminescence for a given quencher concentration $[Q]$, $\tau_0$ the natural fluorescence lifetime, $\tau$ the fluorescence lifetime for a given $[Q]$ and $k_q$ the bimolecular quenching constant, typically around $1 \times 10^9$ to $1 \times 10^{10}$ $M^{-1}$ $s^{-1}$. Because the bimolecular constant and the electrolyte concentrations are relatively fixed, a short $\tau_0$ is important for minimizing the fluorescence quenching. We determined the fluorescence lifetime of the PTCDI to be 4.8 ns (see Supplementary Fig. S2). Figure 3 shows that the fluorescence intensity and lifetime are both reduced with increasing concentrations of the 1-methyl-3-propyl imidazolium iodide (PMII) and $I_2$ species with $k_q$ values of $3.17 \times 10^{10}$ and $0.67 \times 10^{10}$ $M^{-1}$ $s^{-1}$, respectively, indicating dynamic quenching. For the electrolyte used in the DSC (0.6 M PMII, 0.05 M $I_2$) the non-radiative decay rate due to quenching ($k_{QUENCH}$) is calculated to be ~30 times greater than the natural fluorescence decay rate ($k_{QUENCH} = 30k_0$).

The excitation transfer efficiency (ETE) is the probability that an excited ERD will transfer its energy to a SD. The ETE for a single relay dye molecule at position $\vec{x}$ is dependent on the rate of Förster energy transfer, $k_{FRET}$, relative to the combined rate of all decay mechanisms including the natural decay rate and quenching rate:

$$\mathrm{ETE}(\vec{x}) = \frac{k_{\mathrm{FRET}}(\vec{x})}{k_0 + k_{\mathrm{QUENCH}} + k_{\mathrm{FRET}}(\vec{x})} \qquad (3)$$

The FRET rate is a function of the separation distance between the ERD molecule and nearby acceptor molecules. The rate of Förster energy transfer between isolated chromophores, known as point-to-point transfer, is given by $k_{FRET} = k_0(R_o)^6/r^6$, where $r$ is the separation distance. When multiple acceptor molecules are present, the FRET rate is equal to the sum of the transfer rates to each of the acceptors. ERDs within the Förster radius of the SD array will transfer their excitation with high efficiency, whereas ERDs in the middle of a large pore may be quenched before energy transfer occurs. We have developed a model that approximates the nanopores as either cylinders or spheres to calculate FRET rate profiles, $k_{FRET}(\vec{x})$, and excitation transfer efficiency profiles, $\mathrm{ETE}(\vec{x})$, using equation (3), and assuming uniform SD coverage over the pore walls. The morphology of the pores has important implications on ERD/SD array separation distance. Assuming a homogeneous ERD concentration,

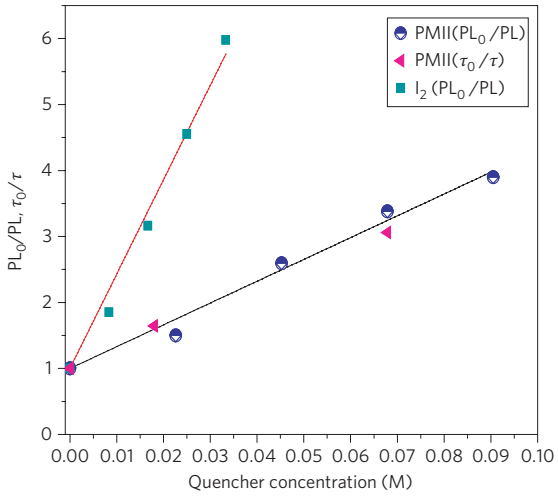


**Figure 3 | Quenching of PTCDI by electrolyte species.** The PTCDI photoluminescence is reduced with increasing concentration of PMII (half-filled blue circles) and $I_2$ (green squares). The reduction in photoluminescence ($PL_0$/PL) by PMII is equivalent to the reduction in excitation lifetime ($\tau_0/\tau$) shown as the red triangles. The PTCDI concentration was $1 \times 10^{-4}$ M in gamma-butyrolactone.

the average separation distance between the ERD and the closest $SD/TiO_2$ interface in a spherical pore is a quarter of the pore radius, whereas in a cylinder the average separation distance is one-third of the pore radius. Figure 4 shows how the average excitation transfer efficiency, $\overline{\mathrm{ETE}}$, depends on the pore diameter for cylindrical and spherical pores using the parameters calculated for the PTCDI–TT1 DSC system. Although the excited ERD has a non-radiative decay half-life of only 0.15 ns (4.8 ns/31) when placed in the electrolyte, it has an expected $\overline{\mathrm{ETE}}$ between 55 and 70% in a 30 nm pore.

The titania film comprised 20-nm particles to ensure close proximity of the ERD to the SD. The 20-nm $TiO_2$ particles produce pore diameters between 22 and 38 nm, a film porosity of 68% (without the addition of the dye), and a roughness factor of 97 $\mu m^{-1}$ (see Supplementary Figs S3,S4). A 10-μm-thick layer of 20-nm particles and a 5-μm-thick layer of 400-nm scattering

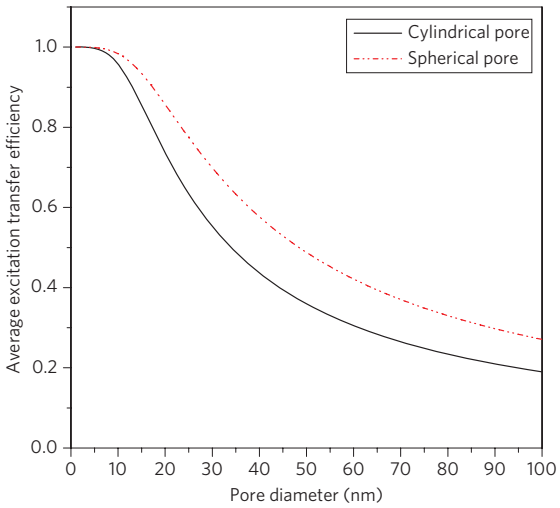


**Figure 4 | Modelled average excitation transfer efficiency as a function of pore diameter for spherical and cylindrical pores.** Modelling results are based on a Förster radius of 7.5 nm, a measured dye coverage of 0.045 $nm^{-2}$ and a quenching rate of $30k_0$.

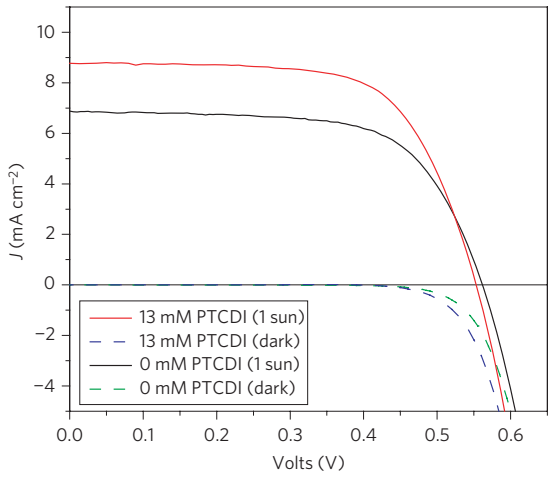


**Figure 5 | Photocurrent density–voltage ($J$–$V$) characteristics of devices with (13 mM PTGCDI) and without (0 mM PTCDI) energy relay dye (ERD) under AM 1.5G (100 mW $cm^{-2}$).** Dashed lines represent the dark current for the ERD containing DSC (blue) and the control device (green).

particles (CCIC, HPW-400) was formed by means of screen printing, sintered at 450 °C, and subsequently treated in $TiCl_4$ (ref. 41). The films were then dipped in a $1 \times 10^{-5}$ M solution of TT1 with 10 mM chenodeoxycholic acid for 4 h and rinsed in acetonitrile[42].

Chloroform was chosen as the electrolyte solvent because PTCDI is significantly more soluble in it (>50 mM) compared to commonly used solvents such as acetonitrile (<2 mM) and gamma-butyrolactone (<2 mM). However, chloroform-based electrolytes displayed lower internal quantum efficiency (70% versus 80%) and lower power conversion efficiencies at higher light intensities (see Supplementary Table S1 and Figs S5,S6)[43,44]. These issues are caused by the reduced $I_3^-$ concentration, lower solubility of useful additives such as LiI and guanidinium rhodanide, and the lower dielectric constant of chloroform ($\varepsilon = 5$) compared to acetonitrile ($\varepsilon = 36$)[45–47]. Devices without the ERD were also made with acetonitrile-based electrolytes and had similar device performances compared to the literature (see Supplementary Fig. S7)[14] . The electrolyte contained 0.6 M PMII, 0.05 M $I_2$, and up to the solubility limits of tertbutyl pyridine (~0.04 M), LiI (~0.01 M) and guanidinium thiocyanate (~0.02 M) in chloroform. PTCDI (13 mM) was subsequently added before electrolyte filling of the DSC. The preparation of the platinum counter-electrode on fluorine-doped tin oxide glass (TEC 15 Ω/□, 2.2 mm thick, Pilkington) is described in a previous report[48]. Electrodes were sealed using a 25-μm-thick hot-melt film (Surlyn 1702, Dupont). A small hole was drilled in the counter-electrode and electrolyte filled using a vacuum pump. It should be noted that $CHCl_3$ has a low boiling point and during electrolyte filling the concentration of PTCDI inside the DSC invariably changed. Higher molar concentrations of PTCDI in the electrolyte did not increase dye loading, but did result in clogging of the hole as the PTCDI electrolyte gelled quickly. A precise determination of the true PTCDI concentration is beyond the scope of this paper, but will be addressed in future publications.

Figure 5 shows the photocurrent density–voltage ($J$–$V$) characteristics of DSCs with and without the ERD measured under AM 1.5G (100 mW $cm^{-2}$) conditions (data shown in Table 1. Devices containing no ERD (0 mM PTCDI) had power conversion efficiencies (PCE) of 2.55% and devices with 13 mM PTCDI had a PCE of 3.21%. The 26% increase in device performance is attributed to the increase in short-circuit photocurrent density ($J_{SC}$) caused by an increase in the EQE from 400 to 600 nm as shown in Fig. 6a, while the fill factor and open-circuit voltage ($V_{OC}$) remained relatively unchanged (see Table 1). Devices made with PTCDI but without the SD were found to have very low photocurrent ($J_{SC} <$ 42 μA $cm^{-2}$ and PCE ≈ 0.01%), demonstrating that energy transfer to the SD is necessary for photocurrent generation by the ERD.

A lower bound for EQE of the ERD ($EQE_{ERD}$) can be calculated from the difference between the EQE of the device containing the ERD and the EQE of the control, ΔEQE, shown in Fig. 6b. The EQE enhancement has a peak of 29.5% at 530 nm, which is ×8 greater than the control (0 mM PTCDI). The ΔEQE spectrum does not perfectly match the absorption of PTCDI because light scattering is greater at lower wavelengths increasing the optical pathway, and at longer wavelengths (>550 nm) the ERD and SD compete for light absorption. The EQE of the ERD is equivalent to the product of the absorption efficiency of the dye, the average excitation transfer efficiency, $\overline{ETE}$, and the internal quantum efficiency (IQE) of the control device:

$$EQE_{ERD} = \eta_{abs,ERD} \cdot \overline{ETE} \cdot IQE \quad (4)$$

A minimum bound for the $\overline{ETE}$ can be calculated by assuming that there is complete light absorption at the ΔEQE peak. Using the dye absorption profiles, this corresponds to $\eta_{abs,ERD} = 89.7\%$ from PTCDI and 10.3% by TT1. If the IQE is assumed to be equal to the peak EQE (70%), a minimum $\overline{ETE}$ of 47% is calculated (see Supplementary Fig. S8).

Using the distribution of pore sizes in the DSC measured by the Brunauer, Emmett and Teller (BET) method (see Supplementary Fig. S4), the measured Förster radius (7.5 nm), the SD surface coverage of 0.045 dye molecules $nm^{-2}$ and the quenching rate calculated above from lifetime measurements ($k_{QUENCH} = 30k_0$) we simulate an $\overline{ETE}$ of 58% for the cylindrical pores and 70% for the spherical pores. This is consistent with the minimum possible ETE observed from the EQE data.

**Table 1 | PV characteristics.**

| | 13 mM PTCDI | 0 mM PTCDI | Change (%) |
|---|---|---|---|
| $J_{SC}$ (mA $cm^{-3}$) | 8.78 | 6.88 | 28 |
| $V_{OC}$ (mV) | 553 | 562 | −1.60 |
| Fill factor | 0.66 | 0.65 | −1.50 |
| PCE (%) | 3.21 | 2.55 | 26 |

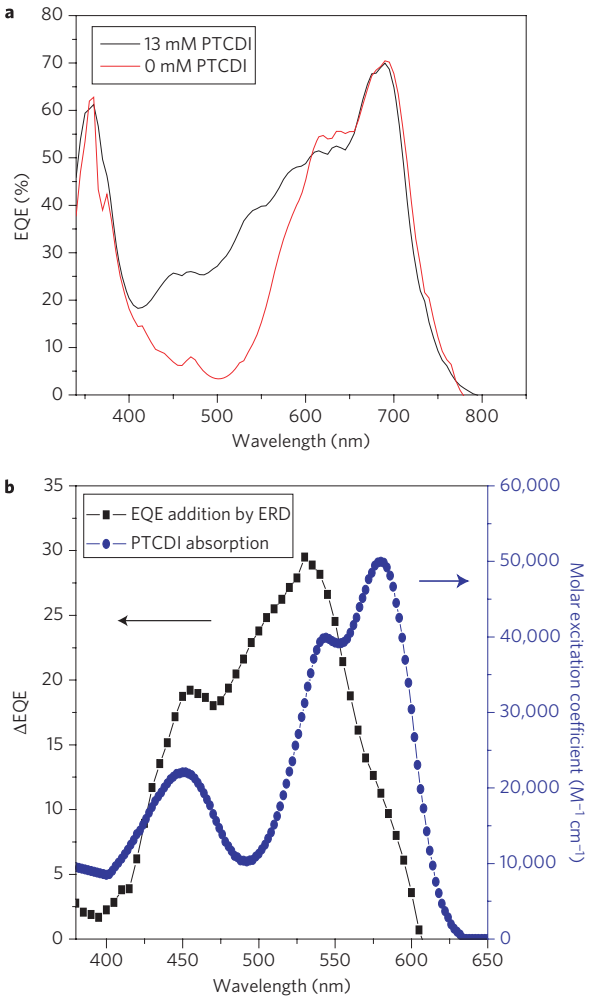


**Figure 6 | Light harvesting characteristics of the energy relay dye (ERD) dye-sensitized solar cell (DSC). a**, External quantum efficiency (EQE) versus wavelength of the DSC with ERD (PTCDI) and a control device (0 mM PTCDI). **b**, EQE addition (black squares) caused by FRET from the ERD to the sensitizing dye (SD) and PTCDI absorption (blue circles). The peak ΔEQE generated by PTCDI was 29.5% at 530 nm.

It is possible to increase the $\overline{ETE}$ by reducing the average pore size inside the titania film. The ETE can be greater than 90% when using smaller nanoparticles (for example, 14 nm) assuming a SD surface concentration of the SD is 0.2 dye molecules $nm^{-2}$ and a spherical pore geometry. Initial results using 14-nm nanoparticles indicate >69% ETE when using PTCDI with TT1; however, more rigorous analysis is necessary both in determining the exact concentration of PTCDI inside the film and the porosity of the samples with the inclusion of the SD. Incorporating PTCDI derivatives that are soluble in acetonitrile or gamma-butyrolactone into films that contain smaller pores should allow PCEs exceeding 5.5% for the PTCDI/TT1 system (see Supplementary Fig. S9). If multiple relay dyes that have complementary absorption spectra are incorporated into the system, higher PCEs are possible.

Given the predicted $\overline{ETE}$, the development of DSCs with PCEs greater than 15% is possible by using a series of ERDs that absorb light from 350 to 800 nm and an SD that absorbs from 800 to 1,000 nm. The realization of extremely efficient DSCs will require the research and development of SDs that can absorb strongly in the infrared. Future infrared SDs will not be required to absorb as broadly, and because the Förster radius is dependent on the emission/absorption overlap multiplied by the wavelength to the fourth power ($\lambda^4$ in equation (1)), it may not need to absorb as strongly. However, the SD will need to have excellent charge injection properties. The potential difference required between the HOMO of the SD and the Nernst potential of the electrolyte is ~300 meV for the iodide/triiodide redox couple and 100–200 meV for the solid-state hole conductor to regenerate the dye. There are many available fluorophores including quantum dots currently used for biomedical imaging that have the potential to be used as ERDs[38], and it may be possible to design ERDs that are minimally quenched by triiodide. Candidates for ERDs should be fast emitters (<100 ns) to reduce quenching by the triiodide and have moderately high PL quantum efficiency (>20%).

## Methods

**Materials synthesis.** All glassware was dried overnight in an oven or by flame before use. Reactions were carried out under nitrogen using standard Schlenk techniques. Reactions were monitored by thin-layer chromatography using Whatman® 250-μm silica gel plates. Flash column chromatography was performed using Merck silica gel, 230–400 mesh. Solvents were removed with a rotary evaporator at aspirator pressure. All reagents were used as received from commercial suppliers without further purification. 9(10),16(17),23(24)-tri-*tert*-butyl-2-carboxy-5,28:14,19-diimino-7,12:21,26 dinitrilotetrabenzo[*c,h,m,r*]tetraazacycloeicosinator-(2⁻)-$N^{29}$,$N^{30}$,$N^{31}$,$N^{32}$ zinc (II) (TT1) was made by a previously reported procedure (ref. 14).

NMR spectra were recorded in $CDCl_3$ with a TMS standard using a Bruker AVB-400 spectrometer. $^{13}C$ NMR was recorded at 100 MHz using $^{1}H$ decoupling. Mass spectrometry and elemental analysis data were recorded by staff members at the UC Berkeley mass spectrometry facility.

**Procedure for *N,N′*-di(2,6-diisopropylphenyl)-1,6,7,12-tetra(4-*tert*-butyl phenyoxy)-perylene-3,4,9,10-tetracarboxylic diimide (PTCDI).** A solution of *N,N′*-di(2,6-diisopropylphenyl)-1,6,7,12-tetrachloroperylene-3,4,9,10-tetracarboxylic diimide (3.00 g, 3.54 mmol, procedure from ref. 49), 4-*tert*-butylphenol (2.66 g, 17.7 mmol), and potassium carbonate (2.92 g, 17.7 mmol) in anhydrous *N*-methylpyrrolidinone (50 ml) was stirred at 130 °C for 16 h. The solution was rapidly poured into 1 M HCl (200 ml) and the resulting precipitate isolated by vacuum filtration and washed repeatedly with water. The precipitate was dissolved in chloroform and extracted twice with water. The chloroform layer was then dried over $Na_2SO_4$ and concentrated. Purification by flash column chromatography (eluent: 40–55% dichloromethane in hexanes) yielded 1.55 g of red solid (34% yield). A portion of this product was further purified by recrystallization: 1.00 g of product was dissolved in dichloromethane (100 ml) and placed in a 1,000 ml graduated cylinder. Methanol (200 ml) was carefully layered on top of the dichloromethane, and the two layers were allowed to mix slowly over 1 week. The resulting red crystals were isolated by filtration and dried under vacuum, yielding 740 mg of red product.

**Characterization.** m.p. > 300 °C. $^{1}H$ NMR (400 MHz, $CDCl_3$, δ): 8.29 (s, 4H), 7.42 (t, $J$ = 7.8 Hz, 2H), 7.22–7.28 (m, 12H), 6.87 (dt, $J$ = 8.8 and 2.5 Hz, 8H), 2.71 (m, $J$ = 6.8 Hz, 4H), 1.28 (s, 36H), 1.13 (d, $J$ = 6.8 Hz, 24H). $^{13}C$ NMR (100 MHz, $CDCl_3$, δ): 163.55, 156.12, 152.99, 147.55, 145.82, 133.44, 130.88, 129.60, 126.88, 124.09, 122.89, 120.97, 120.45, 120.39, 119.41, 34.58, 31.66, 29.28, 24.24. FTIR (film on NaCl): $\nu$ = 2,963, 2,870, 1,709, 1,675, 1,588, 1,505, 1,406, 1,340, 1,285, 1,209, 1,175 $cm^{-1}$. HRMS (FAB+, $m/z$): calculated for $C_{88}H_{91}N_2O_8$, 1303.6775; found, 1303.6786. Anal. calculated for $C_{88}H_{90}N_2O$: C 81.07, H 6.96, N 2.15; found: C, 80.08; H, 6.97; N, 2.09.

**Electrical measurements.** The power of the AM 1.5 solar simulator (100 mW $cm^{-2}$) was calibrated using a reference silicon photodiode equipped with an infrared cutoff filter (KG-3, Schott) to reduce the mismatch between the simulated light and solar spectrum from 350–700 nm to less than 2% (ref. 50). The *J–V* curves were obtained by externally biasing the DSC and measuring the photocurrent using a Keithley 2400 digital source meter. All measurements were performed using a metal mask with an aperture of 0.159 $cm^2$ to reduce light scattering.

The EQE measurement light source was a 300 W xenon lamp (ILC Technology), which was focused through a Gemini-180 double monochromator (Jobin Yvon). EQE measurements were performed at 1% sun using a metal mask with an aperture area of 0.159 $cm^2$. Integrating the EQE spectra of the ERD-containing and control DSCs resulted in slightly higher (~10%) estimated $J_{SC}$ at full sun than those measured in the devices. This is a result of charge transport limitations caused by the electrolyte at higher light intensities. Extrapolating device results from measurements taken at 10% sun (see Supplementary Fig. S6) to full sun are consistent with the estimated $J_{SC}$ from the EQE results. The difference in the integrated EQE spectrum between the ERD-containing and control devices is the same ratio as the differences in $J_{SC}$ at full sun.

**Photoluminescence lifetime measurements.** Time-resolved PL measurements were performed using a time-correlated single-photon counting (TCSPC) system from PicoQuant. Solutions were excited with a pulsed laser diode, (model LDH 485: 481 nm, 70 ps FWHM, 5 MHz) detected with a single-photon avalanche diode

(PDM 100CT SPAD) attached to a monochromator and processed by a PicoHarp 300 correlating system.

Received 12 March 2009; accepted 18 May 2009; published online 21 June 2009

## References


1. O'Regan, B. & Gratzel, M. A low-cost, high-efficiency solar cell based on dye-sensitized colloidal $TiO_2$ films. *Nature* **353,** 737–740 (1991).
2. Peter, L. M. Dye-sensitized nanocrystalline solar cells. *Phys. Chem. Chem. Phys.* **9,** 2630–2642 (2007).
3. Snaith, H. J. & Schmidt-Mende, L. Advances in liquid-electrolyte and solid-state dye-sensitized solar cells. *Adv. Mater.* **19,** 3187–3200 (2007).
4. Bisquert, J., Cahen, D., Hodes, G., Ruhle, S. & Zaban, A. Physical chemical principles of photovoltaic conversion with nanoparticulate, mesoporous dye-sensitized solar cells. *J. Phys. Chem. B* **108,** 8106–8118 (2004).
5. Hagfeldt, A. & Gratzel, M. Molecular photovoltaics. *Acc. Chem. Res.* **33,** 269–277 (2000).
6. Nazeeruddin, M. K. *et al.* Combined experimental and DFT-TDDFT computational study of photoelectrochemical cell ruthenium sensitizers. *J. Am. Chem. Soc.* **127,** 16835–16847 (2005).
7. Hamann, T. W., Jensen, R. A., Martinson, A. B. F., Ryswyk, H. V. & Hupp, J. T. Advancing beyond current generation dye-sensitized solar cells. *Energy Environ. Sci.* **1,** 66–78 (2008).
8. Gratzel, M. Conversion of sunlight to electric power by nanocrystalline dye-sensitized solar cells. *J. Photochem. Photobiol. A* **164,** 3–14 (2004).
9. Wang, P. *et al.* A stable quasi-solid-state dye-sensitized solar cell with an amphiphilic ruthenium sensitizer and polymer gel electrolyte. *Nature Mater.* **2,** 402–407 (2003).
10. Yum, J.-H. *et al.* Efficient far red sensitization of nanocrystalline $TiO_2$ films by an unsymmetrical squaraine dye. *J. Am. Chem. Soc.* **129,** 10320–10321 (2007).
11. Burke, A., Schmidt-Mende, L., Ito, S. & Gratzel, M. A novel blue dye for near-IR 'dye-sensitized' solar cell applications. *Chem. Commun.* **3,** 234–236 (2006).
12. Campbell, W. M. *et al.* Highly efficient porphyrin sensitizers for dye-sensitized solar cells. *J. Phys. Chem. C* **111,** 11760–11762 (2007).
13. He, J. *et al.* Modified phthalocyanines for efficient near-IR sensitization of nanostructured $TiO_2$ electrode. *J. Am. Chem. Soc.* **124,** 4922–4932 (2002).
14. Cid, J.-J. *et al.* Molecular cosensitization for efficient panchromatic dye-sensitized solar cells. *Angew. Chem.* **119,** 8510–8514 (2007).
15. Tachibana, Y., Nazeeruddin, M. K., Grätzel, M., Klug, D. R. & Durrant, J. R. Electron injection kinetics for the nanocrystalline $TiO_2$ films sensitised with the dye $(Bu_4N)_2Ru(dcbpyH)_2(NCS)_2$. *Chem. Phys.* **285,** 127–132 (2002).
16. Tachibana, Y., Moser, J. E., Gratzel, M., Klug, D. R. & Durrant, J. R. Subpicosecond interfacial charge separation in dye-sensitized nanocrystalline titanium dioxide films. *J. Phys. Chem.* **100,** 20056–20062 (1996).
17. Haque, S. A. *et al.* Parameters influencing charge recombination kinetics in dye-sensitized nanocrystalline titanium dioxide films. *J. Phys. Chem. B* **104,** 538–547 (2000).
18. Nazeeruddin, M. K. *et al.* Conversion of light to electricity by *cis*-$X_2$*bis*(2,2′-bipyridyl-4,4′-dicarboxylate)ruthenium(II) charge-transfer sensitizers (X = $Cl^-$, $Br^-$, $I^-$, $CN^-$ and $SCN^-$) on nanocrystalline titanium dioxide electrodes. *J. Am. Chem. Soc.* **115,** 6382–6390 (1993).
19. Haque, S. A., Tachibana, Y., Klug, D. R. & Durrant, J. R. Charge recombination kinetics in dye-sensitized nanocrystalline titanium dioxide films under externally applied bias. *J. Phys. Chem. B* 1998, 1745–1749 (1998).
20. O'Regan, B. C. *et al.* Catalysis of recombination and its limitation on open circuit voltage for dye sensitized photovoltaic cells using phthalocyanine dyes. *J. Am. Chem. Soc.* **130,** 2906–2907 (2008).
21. O'Regan, B. C. *et al.* Structure/function relationships in dyes for solar energy conversion: a two-atom change in dye structure and the mechanism for its effect on cell voltage. *J. Am. Chem. Soc.* **131,** 3541–3548 (2009).
22. Clifford, J. N., Palomares, E., Nazeeruddin, M. K., Gratzel, M. & Durrant, J. R. Dye dependent regeneration dynamics in dye sensitized nanocrystalline solar cells: Evidence for the formation of a ruthenium bipyridyl cation/iodide intermediate. *J. Phys. Chem. C* **111,** 6561–6567 (2007).
23. Siegers, C. *et al.* A dyadic sensitizer for dye solar cells with high energy-transfer efficiency in the device. *Chem. Phys. Chem.* **8,** 1548–1556 (2007).
24. Hu, X. & Schulten, K. How nature harvests sunlight. *Phys. Today* **50,** 28–34 (1997).
25. Hu, X., Damjanovic, A., Ritz, T. & Schulten, K. Architecture and mechanism of the light-harvesting apparatus of purple bacteria. *Proc. Natl Acad. Sci. USA* **95,** 5935–5941 (1998).
26. Pullerits, T. & Sundstrom, V. Photosynthetic light-harvesting pigment–protein complexes: Toward understanding how and why. *Acc. Chem. Res.* **29,** 381–389 (1996).
27. Hardin, B. E. in *et al.* Materials Research Society Fall Meeting (Boston, MA, 2008).
28. Siegers, C. *et al.* Overcoming kinetic limitations of electron injection in the dye solar cell via coadsorption and FRET. *Chem. Phys. Chem.* **9,** 793–798 (2008).
29. Bach, U. *et al.* Solid-state dye-sensitized mesoporous $TiO_2$ solar cells with high photon-to-electron conversion efficiencies. *Nature* **395,** 583–585 (1998).
30. Snaith, H. J. *et al.* Efficiency enhancements in solid-state hybrid solar cells via reduced charge recombination and increased light capture. *Nano Lett.* **7,** 3372–3376 (2007).
31. Mor, G. K., Shankar, K., Paulose, M., Varghese, O. K. & Grimes, C. A. Use of highly-ordered $TiO_2$ nanotube arrays in dye-sensitized solar cells. *Nano Lett.* **6,** 215–218 (2006).
32. Law, M., Greene, L. E., Johnson, J. C., Saykally, R. & Yang, P. Nanowire dye-sensitized solar cells. *Nature Mater.* **4,** 455–459 (2005).
33. Forster, T. Transfer mechanisms of electronic excitation. *Discuss. Faraday Soc.* **27,** 7 (1959).
34. Scully, S. R., Armstrong, P. B., Edder, C., Frechet, J. M. J. & McGehee, M. D. Long-range resonant energy transfer for enhanced exciton harvesting for organic solar cells. *Adv. Mater.* **19,** 2961–2966 (2007).
35. Liu, Y. X., Summers, M. A., Edder, C., Fréchet, J. M. J. & McGehee, M. D. Using resonance energy transfer to improve exciton harvesting in organic–inorganic hybrid photovoltaic cells. *Adv. Mater.* **17,** 2960–2964 (2005).
36. Hill, Z. B., Rodovsky, D. B., Leger, J. M. & Bartholomew, G. P. Synthesis and utilization of perylene-based n-type small molecules in light-emitting electrochemical cells. *Chem. Commun.* 6594–6596 (2008).
37. Wurthner, F. Perylene bisimide dyes as versatile building blocks for functional supramolecular architectures. *Chem. Commun.* 1564–1579 (2004).
38. Lakowicz, J. R. *Principles of Fluorescence Spectroscopy* (Plenum, 1999).
39. Stern, V. O. & Volmer, M. Uber die abklingungszeit der fluoreszenz. *Zeitschrift für Physik* **20,** 183–189 (1919).
40. Mac, M., Wach, A. & Najbar, J. Solvents effects on the fluorescence quenching of anthracene by iodide ions. *Chem. Phys. Lett.* **176,** 167–172 (1991).
41. Sommeling, P. M. *et al.* Influence of a $TiCl_4$ post-treatment on nanocrystalline $TiO_2$ films in dye-sensitized solar cells. *J. Phys. Chem. B* **110,** 19191–19197 (2006).
42. Yum, J.-H. *et al.* Effect of coadsorbent on the photovoltaic performance of zinc pthalocyanine-sensitized solar cells. *Langmuir* **24,** 5636–5640 (2008).
43. Haque, S. A. *et al.* Charge separation versus recombination in dye-sensitized nanocrystalline solar cells: the minimization of kinetic redundancy. *J. Am. Chem. Soc.* **127,** 3456–3462 (2005).
44. Huang, S., Schlichthorl, G., Nozik, A., Gratzel, M. & Frank, A. Charge recombination in dye-sensitized nanocrystalline $TiO_2$ solar cells. *J. Phys. Chem. B* **101,** 2576–2582 (1997).
45. Kebede, Z. & Lindquist, S.-E. Donor–acceptor interaction between non-aqueous solvents and $I_2$ to generate $I_3^-$, and its implication in dye sensitized solar cells. *Solar Energy Mater. Solar Cells* **57,** 259–275 (1999).
46. Fabregat-Santiago, F., Bisquert, J., Garcia-Belmonte, G., Boschloo, G. & Hagfeldt, A. Influence of electrolyte in transport and recombination in dye-sensitized solar cells studied by impedance spectroscopy. *Solar Energy Mater. Solar Cells* **87,** 117–131 (2005).
47. Haque, S. A. *et al.* Charge separation versus recombination in dye-sensitized nanocrystalline solar cells: The minimization of kinetic redundancy. *J. Am. Chem. Soc.* **127,** 3456–3462 (2005).
48. Ito, S. *et al.* Fabrication of thin film dye sensitized solar cells with solar to electric power conversion efficiency over 10%. *Thin Solid Films* **516,** 4613–4619 (2008).
49. Klok, H. A., Hernández, J. R., Becker., S. & Müllen, K. Star-shaped fluorescent polypeptides. *J. Polym. Sci. Part A: Polym. Chem.* **39,** 1572–1583 (2001).
50. Ito, S. *et al.* Calibration of solar simulator for evaluation of dye-sensitized solar cells. *Solar Energy Mater. Solar Cells* **82,** 421–429 (2004).


## Acknowledgements

The authors thank Y.C. Jun and M.L. Brongersma for access to time-resolved PL measurement equipment and assistance with measurements. B.E.H. would like to thank P. Péchy for his assistance in making the electrolyte. This work was supported by the King Abdullah University of Science and Technology Center for Advanced Molecular Photovoltaics and by the Office of Naval Research contract no. N00014-08-1-1163. B.E.H. received financial support from the National Department of Defense Science and Engineering Graduate Fellowship (NDSEG). E.T.H. is supported by the National Science Foundation GRFP and the Fannie and John Hertz Foundation. J.M.F. is supported by DOE-BES contract DE-AC02-05CH11231.

## Author contributions

B.E.H. assembled the DSCs and performed measurements for Figs 3, 5 and 6. E.T.H. modelled the excitation transfer efficiency for the spherical and cylindrical geometries shown in Fig. 4. P.B.A. synthesized the ERD (PTCDI) and T.T. synthesized the sensitizing dye (TT1). P.C. fabricated the $TiO_2$ electrodes and provided BET data to determine pore size. J.Y.H. and M.K.N. measured dye absorption and dye adsorption on $TiO_2$ and provided guidance in electrolyte design. J.M.J., M.G. and M.D.M. provided technical advice on dye design and DSC device physics.

## Additional information

Supplementary information accompanies this paper at www.nature.com/naturephotonics. Reprints and permission information is available online at http://npg.nature.com/reprintsandpermissions/. Correspondence and requests for materials should be addressed to M.D.M.

ARTICLES
PUBLISHED ONLINE: 21 JUNE 2009 | DOI: 10.1038/NPHOTON.2009.98
nature photonics

# Multispectral opto-acoustic tomography of deep-seated fluorescent proteins *in vivo*

Daniel Razansky[1]*, Martin Distel[2], Claudio Vinegoni[3], Rui Ma[1], Norbert Perrimon[4], Reinhard W. Köster[2] and Vasilis Ntziachristos[1]*

**Fluorescent proteins have become essential reporter molecules for studying life at the cellular and sub-cellular level, re-defining the ways in which we investigate biology. However, because of intense light scattering, most organisms and tissues remain inaccessible to current fluorescence microscopy techniques at depths beyond several hundred micrometres. We describe a multispectral opto-acoustic tomography technique capable of high-resolution visualization of fluorescent proteins deep within highly light-scattering living organisms. The method uses multiwavelength illumination over multiple projections combined with selective-plane opto-acoustic detection for artifact-free data collection. Accurate image reconstruction is enabled by making use of wavelength-dependent light propagation models in tissue. By performing whole-body imaging of two biologically important and optically diffuse model organisms, *Drosophila melanogaster* pupae and adult zebrafish, we demonstrate the facility to resolve tissue-specific expression of eGFP and mCherrry fluorescent proteins for precise morphological and functional observations *in vivo*.**

Fluorescence protein (FP) imaging is increasingly being used as a key technology allowing the comprehension of complex and diverse mechanisms in many areas of biology and medical research[1]. By allowing *in vivo* observation of multifactorial dynamic interactions, confocal and multiphoton tissue-sectioning microscopies have become the major means of FP visualization, radically changing biological understanding[2–4]. Despite significant technological progress[4–7], high-resolution imaging is limited by the interaction of photons with cellular interfaces and organelles, which results in high levels of photon scattering. Consequently, state-of-the-art intravital (*in vivo*) microscopy operates only at depths that are less than one transport mean free path length (MFPL) in tissue[8] (the distance it takes for light to become highly diffuse, typically between a few hundred micrometres and 1 mm). As a result, a significant amount of *in vivo* biological research revolves around the study of organisms that are virtually transparent, such as early-stage *Caenorhabditis elegans* or zebrafish (*Danio rerio*)[9], or uses highly invasive techniques such as the implementation of biocompatible windows to study activity deeper in the body[10]. Optical projection tomography (OPT)[11], selective-plane illumination microscopy (SPIM)[12] and ultramicroscopy[13] have been developed recently as alternative tomographic methods to confocal and nonlinear microscopy, but are also strongly limited by tissue scattering. They can be similarly applied to the imaging of naturally transparent live specimens, such as organisms at very early stages of development, or organisms and tissues chemically treated to remove scattering (when applied to dimensions of the order of one MFPL or larger), which applies therefore only to studies that can be performed post mortem.

The urgent need to improve *in vivo* visualization capacity in the post-genomic era has been recently outlined[14]. *In vivo* imaging beyond one transport MFPL can be used to follow cell motility and interaction or organ development and function within large tissue volumes over long periods of time[15]. Non-invasive high-resolution tomographic imaging of FPs in adult organisms and mice could therefore offer an important visualization tool for functional genomics and proteomics at different system levels, that is, from the cell to the organ. Such a capacity will also shift the paradigm of biological observations and accelerate discovery by enabling *in vivo* longitudinal observation of dynamic phenomena on the same growing or developing organism, thus minimizing the need for laborious histological examinations and large cohorts to obtain meaningful statistics. From high-throughput whole-body phenotyping and time-lapse imaging in adult model organisms to understanding signalling and interactions of tissues with drugs and environmental factors, visualization beyond the penetration limit of modern microscopy will open new pathways for biological discovery.

In this work we report on the visualization of fluorescent proteins well beyond the penetration limits of optical microscopy while preserving high sensitivity and spatial resolution. To achieve this, we have developed and implemented a selective-plane multispectral opto-acoustic tomography (MSOT) method based on ultrasonic detection of pressure waves generated by the absorption of pulsed light in elastic media. The amplitude of the broadband ultrasound waves, generated by the absorption of pulsed light by tissue chromophores[16], is processed tomographically to offer three-dimensional images of optical contrast reaching ultrasonic diffraction-limited resolution, not limited by the degree of light scattering. The ability to create images based on opto-acoustics has already been established in resolving vascular structures[17,18] and functional imaging in mice[19]. Applied in reflectance scanning mode, high-resolution functional photoacoustic microscopy[20] has also demonstrated the ability to image subcutaneous tumour angiogenesis and blood oxygen saturation in rats and humans at a depth of ~600 μm. In recent years, attention has also been given to resolving molecular contrast using fluorescent contrast agents[21], chromogenic assays[22] and nanoparticles[23].

[1]Institute for Biological and Medical Imaging, Technical University of Munich and Helmholtz Center Munich, Ingolstädter Landstraße 1, D-85764 Neuherberg, Germany, [2]Institute of Developmental Genetics, Helmholtz Center Munich, Ingolstädter Landstraße 1, D-85764 Neuherberg, Germany, [3]Center for Systems Biology, Massachusetts General Hospital and Harvard Medical School, Richard B. Simches Research Center, 185 Cambridge Street, Boston, Massachusetts 02114, USA, [4]Department of Genetics, Harvard Medical School and Howard Hughes Medical Institute, 77 Avenue Louis Pasteur, Boston, Massachusetts 02115, USA. *e-mail: dr@tum.de; v.ntziachristos@tum.de

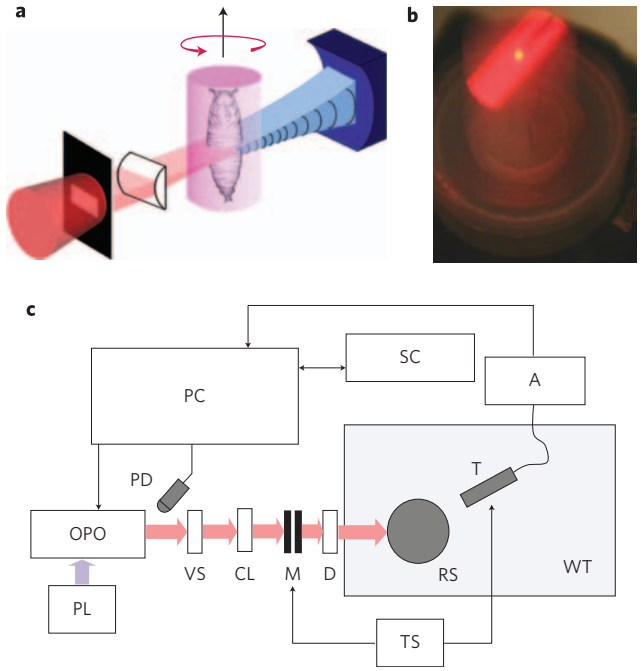


**Figure 1 | Experimental setup of multispectral opto-acoustic tomography.** **a**, Confocal illumination and detection scheme (red, illuminating light beam; blue, generated ultrasonic waves). **b**, Top-view photograph of the cylindrically focused beam passing through agar phantom with embedded *Drosophila* pupae. **c**, Schematic of the experimental setup. OPO, optical parametric oscillator; RS, rotation stage; SC, stage controller; VS, variable slit; CL, cylindrical lens; WT, water tank; D, engineered diffuser; T, ultrasonic transducer; M, mirror; TS, translation stage; PD, photodiode; PC, computer; A, amplifier; PL, pump laser.

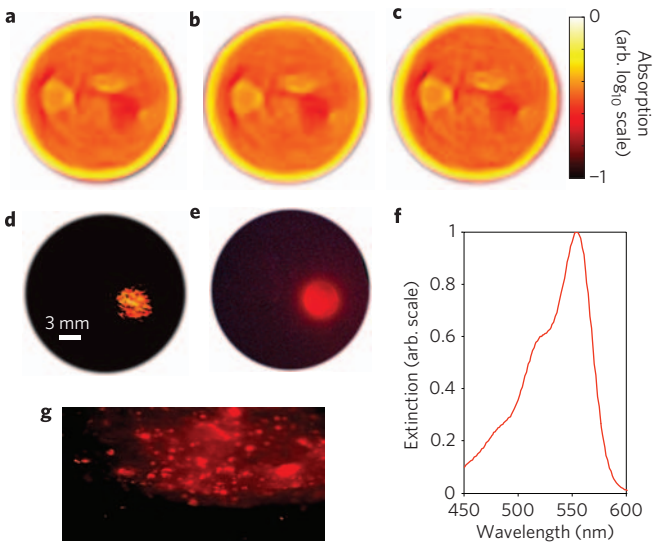


**Figure 2 | Multispectral opto-acoustic imaging of tissue-mimicking phantom containing DsRed-expressing HeLa cells. a–c**, Single-wavelength opto-acoustic images of the phantom acquired at 550 nm (**a**), 560 nm (**b**) and 570 nm (**c**). **d**, Spectrally resolved (MSOT) image of DsRed distribution in the phantom. **e**, Fluorescence image of dissected phantom at approximately the same imaging plane (red colour corresponds to the location of fluorescent cells). **f**, Extinction spectra of DsRed. **g**, Magnified image of phantom at the boundary of the area containing the DsRed cells.

In contrast to existing studies, we have established a multiprojection MSOT method that can volumetrically resolve FPs *in vivo* in small animals and tissues. By combining selective-plane illumination to minimize out-of-plane contributions and tomographic principles for image reconstruction, we demonstrate that it is possible to tune accurately the inversion process and detect specific FPs over non-specific background absorption with high sensitivity. In addition, the underlining anatomical images of the tissue are simultaneously provided. Applied to biological specimens, this technology extends fluorescence imaging to dimensions never visualized optically in the past, because it is capable of *in vivo* visualization of fluorescent proteins in intact model organisms at depth scales that are significantly larger than 1 mm, currently unattainable by other imaging techniques applied to living specimens, including confocal and multiphoton microscopies.

The experimental setup used nanosecond pulsed laser illumination at multiple wavelengths, which passed through a variable-slit aperture and focused, using a cylindrically focusing lens, onto the sample, creating a planar sheet of light (Fig. 1). The imaged objects were fixed on a rotation stage submerged into water to facilitate detection of acoustic signals. Opto-acoustic signals were recorded by a broadband ultrasonic transducer, cylindrically focused at the optical illumination plane (confocal arrangement). At each illumination wavelength and imaging height, the in-plane images were reconstructed using a filtered back-projection algorithm (see Methods for details on the experimental system and image reconstruction algorithms).

To confirm the basic ability of the method to detect fluorescent proteins over background absorption and quantify its performance, a cylindrical tissue-mimicking phantom (diameter, 1.9 cm; optical absorption coefficient, 0.3 $cm^{-1}$; scattering, 10 $cm^{-1}$) was generated by dissolving India ink and Intralipid in agar (see Supplementary information for a detailed description of phantom preparation). The phantom mimics the dimensions and average optical properties of mouse tissue at a wavelength of ~630 nm. Two 4-mm-diameter insertions were incorporated into the phantom. The first insertion contained stable transgenic HeLa cells ($4 \times 10^6$ $ml^{-1}$) expressing a mitochondrial targeted DsRedT4 fluorescent protein variant mixed with a solution of Intralipid and ink similar to background. The second insertion (absorption coefficient, 0.6 $cm^{-1}$; scattering, 10 $cm^{-1}$) served as a control and contained a higher concentration of India ink but no fluorescent cells.

The principle of detection is based on differentiation of the absorption spectral signature of the protein over background tissue absorption by the analysis of multiwavelength data. Fluorescent proteins are excellent molecules for this role compared to other chromophoric substances such as India ink, because they exhibit a steep declining absorption slope at lower energies, which can easily be detected spectroscopically, as shown in Fig. 2f, by taking measurements at multiple wavelengths. Although single-wavelength images only reveal the highly absorbing control insertion and some phantom heterogeneities (Fig. 2a–c), the non-specific contrast from the insertion containing DsRed-expressing cells is barely visible. Nevertheless, multiwavelength processing of the images on a per-pixel basis (see Methods) renders high contrast from the FP-expressing cells with a contrast-to-noise ratio (CNR) of 32, while suppressing other non-specific contrast (Fig. 2d). The results show excellent agreement with the epifluorescence image shown in Fig. 2e, obtained after phantom sectioning to validate the tomographic images of the intact phantom.

To investigate the *in vivo* capacity of the method to image tissues beyond the limits of modern microscopy, the zebrafish and *Drosophila melanogaster* (fruit fly) were selected as the imaging targets, partly because these organisms are extensively used in various fields of genetics and other areas of modern biology. By extending non-invasive fluorescence imaging of optically transparent organisms in early development stages to imaging opaque

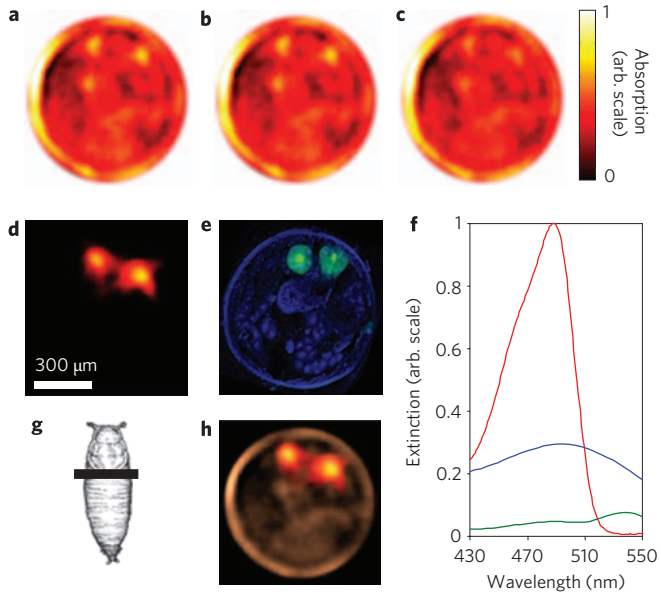


**Figure 3 | Imaging of eGFP distribution in *Drosophila melanogaster* pupa.** **a**–**c**, Opto-acoustic images acquired at 488 nm (**a**), 498 nm (**b**) and 508 nm (**c**). **d**, Spectrally resolved (MSOT) image of eGFP distribution in an intact pupa. **e**, Corresponding histology of DAPI-stained pupa at approximately the same imaging plane (green colour corresponds to GFP-expressing salivary glands). **f**, Extinction spectra of eGFP (red) along with measured absorption of pupa case (blue) and fat areas (green). **g**, Imaging plane. **h**, Overlay between the image at 508 nm (**c**) and the spectrally resolved image.

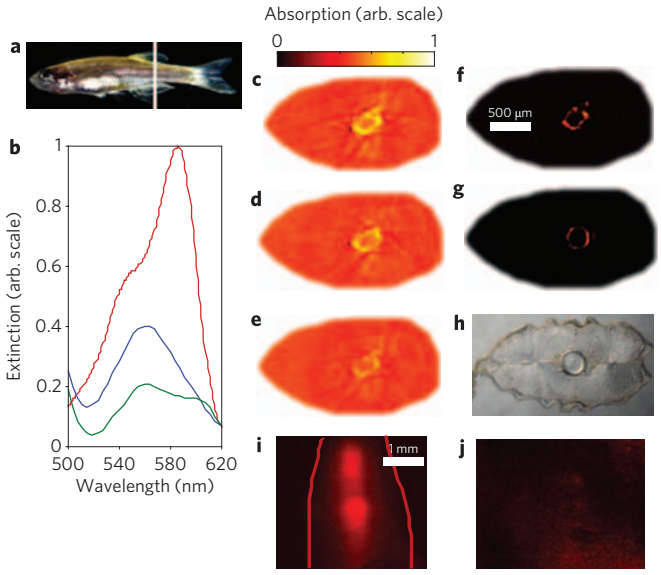


**Figure 4 | Imaging of mCherry distribution in the vertebral column of an adult zebrafish.** **a**, Location of the imaging plane. **b**, Extinction spectra of mCherry (red curve) and the intrinsic background (vertebral column, blue; muscles, green). **c**–**e**, Opto-acoustic images acquired at 587 nm (**c**), 597 nm (**d**) and 607 nm (**e**). **f**, Spectrally resolved image of mCherry distribution in an intact animal. **g**, Histological epifluorescence image of dissected tissue at approximately the same imaging plane (red colour corresponds to mCherry-expressing vertebral column). **h**, Regular histological section. **i**, Epifluorescence image of a living zebrafish. Red curves show the surface outline. **j**, Coronal confocal image at a depth of ~500 μm from the surface. A juvenile two-month-old zebrafish was used in this case (short axis thickness of ~1 mm in the imaged area).

organisms through adulthood, several dynamic aspects of molecular and cellular mechanisms of disease aetiology and progression, aging and the effects of environmental factors may be studied *in vivo* in an intact specimen. Furthermore, the large number of FPs available have provided powerful tools for mechanistic and functional genetic research, and many transgenic models expressing these genetic fluorescent markers in a cell-type-specific manner have been established to investigate cellular and sub-cellular function.

Imaging results from a *Drosophila melanogaster* pupa are presented in Fig. 3. In this case, a Gal-4/UAS system was used to specifically express eGFP (enhanced green fluorescent protein) in the salivary glands of the fly pupae (see Supplementary information for details). The imaging plane was located in the posterior part of the salivary glands area, as shown in Fig. 3 g. In this pupal stage, the *Drosophila* exhibits significant scattering[25] and is not accessible through its intact case by conventional fluorescent microscopy. The opto-acoustic images at three representative wavelengths are shown in Fig. 3a–c. The pupal case is readily identified in those images as having rather high optical absorption compared to internal structures. The various fatty structures are also clearly visualized. As in the previous imaging sessions, despite their strong eGFP expression, the salivary glands are not clearly distinguishable on single-wavelength images due to other non-specific background absorption. Figure 3f shows the spectral response of the pupal tissue as calculated by corresponding multiwavelength opto-acoustic measurements. After spectral processing, the salivary glands can be accurately visualized as shown in Fig. 3d,h. The corresponding histological section at approximately the same imaging plane is shown in Fig. 3e and is in good agreement with the reconstruction. The in-plane spatial resolution of opto-acoustic images is mainly determined by the effective bandwidth of the ultrasonic detector (20 MHz), leading to ~38 μm diffraction limited (half-wavelength) resolution in water. The vertical resolution was limited by the focal width of the ultrasonic detector to 150 μm.

To demonstrate the ability of the system to image through larger dimensions, we imaged adult zebrafish. Figure 4 shows results from a transgenic three-month old zebrafish in which the Gal-4/UAS system was used to express the mCherry FP in the vertebral column (see Supplementary information for details). This transgenic strain was chosen because the vertebral column represents one of the deeper structures in the highly scattering adult trunk and thus provides a significant imaging challenge. The specimen, measuring $2.5 \times 4$ mm$^2$ (see image cross-section in Fig. 4a), was held in the imaging setup by an agar phantom. Illumination was performed at multiple wavelengths, targeting the steep declining slope of the mCherry extinction spectra shown in Fig. 4b. Opto-acoustic images of the mCherry-expressing zebrafish at three representative wavelengths are shown in Fig. 4c–e and, as expected, exhibit strong contrast from varying tissue absorption in the vertebral column and surrounding structures. Similarly, spectral decomposition accurately resolves the location of mCherry expression in the intact animal (Fig. 4f). Subsequent histological sectioning (Fig. 4h) and epifluorescence image recording of tissue sections (Fig. 4g) demonstrated high congruence between *in vivo* and *ex vivo* images from the animal. The MSOT images provided an in-plane spatial resolution of less than 40 μm, as can be elucidated from the thickness of the fluorescent ring-like structure of the vertebral column in Fig. 4f. This spatial resolution can be substantially improved by using ultrasonic detectors with larger bandwidth. There is no methodology currently available that allows visualization of reporter molecules at these resolutions and these dimensions. Existing microscopy methods are mostly limited by resolution and SNR degradation due to light diffusion beyond depths of ~500 μm in scattering tissue. For comparison, we also provide an image of a juvenile (one-month-old) zebrafish using confocal

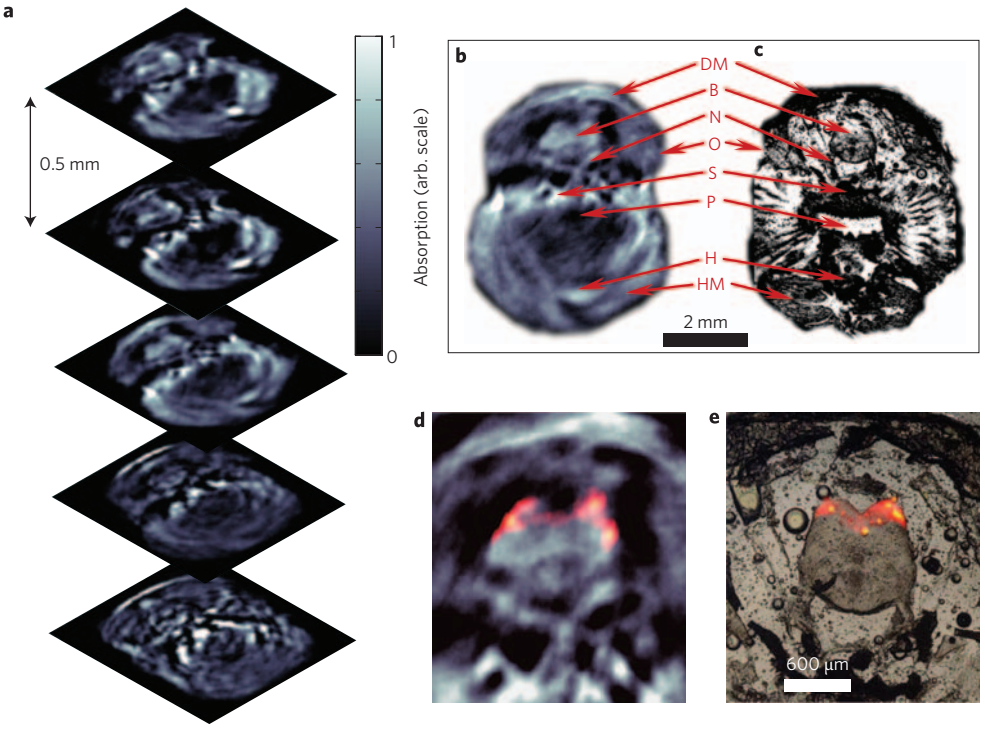


**Figure 5 | Three-dimensional *in vivo* imaging through the brain of an adult (six-month-old) mCherry-expressing transgenic zebrafish. a**, Five transverse opto-acoustic imaging slices through the hindbrain area at the level of crista cerebellaris of a living zebrafish taken at 585 nm. **b**,**c**, Example of an imaged slice (**b**) and its corresponding histological section in inverted colours (**c**). DM, dorsal fin musculature; B, hindbrain; N, lateral line nerve; O, operculum; S, skull bones; P, pharynx; H, heart; HM, hypobranchial musculature. **d**, MSOT image of the brain (enlarged) with mCherry expression shown in colour. **e**, Corresponding fluorescent histology of a dissected fish at the hindbrain level.

microscopy in Fig. 4j. Even though the cross-section here measures only ~1–2 mm as compared to 2.5–4 mm as imaged by MSOT, the confocal microscopy cannot image through the highly scattering juvenile zebrafish while an additional epifluorescence image (Fig. 4i) shows that the fluorescent vertebral column exhibits a highly diffusive appearance through 1–2 mm of tissue. Although multiphoton microscopy could possibly penetrate slightly deeper, it would also be limited by this light diffusion at about one transport MFPL, that is, <1 mm in scattering tissue.

To further showcase the MSOT capacity of performing three-dimensional *in vivo* scans we also imaged through the head of an adult (six-month-old) mCherry-expressing transgenic zebrafish (see Supplementary Information for details) with a cross-sectional diameter of ~6 mm. To guarantee survival, the fish was attached to the rotation stage by partially embedding it into modelling clay so that the upper parts including the head and gills were exposed to the anaesthetic solution (Tricaine) in the imaging tank. The fish fully recovered from the *in vivo* imaging sessions. The imaging results, shown in Fig. 5, demonstrate the ability of the process to reveal many morphological features, as is evident from Fig. 5a,b, supported by the corresponding histology (Fig. 5c). Moreover, multispectral reconstructions accurately resolved FP expression in the hindbrain of an intact living animal (Fig. 5d), in high congruence with the corresponding epifluorescence images of the dissected brain (Fig. 5e).

The ability to optically interrogate and visualize intact organisms beyond the limits of microscopy is of great importance in the post-genomic era for accelerating the study of genomics and proteomics. This work reports on the development of multiprojection multispectral opto-acoustic tomography (MSOT) for imaging biological organisms, and discusses its previously undocumented capacity for effectively detecting FPs in tissues, *in vivo*. The method was found to be capable of offering a new generation of biological imaging by visualizing optical reporter molecules deep inside the body of mature organisms with high (mesoscopic) resolution, while simultaneously providing the necessary reference anatomical images. A particular strength of the technology is its ability to scale with different tissue sizes. Imaging of a zebrafish up to 6 mm thick was shown. However, as demonstrated in phantom experiments, several centimetres of penetration with nearly the same resolution can be achieved, particularly when using near-infrared light. Indeed, many relevant biological samples and model organisms (such as worms, developing and adult insects, and vertebrates including small mammals and their extremities) have sizes lying in this range and could therefore be visualized.

The phantom measurements of Fig. 2 allow for the calculation and prediction of the detection limits of the current system. To achieve this, we performed a theoretical analysis to translate the system noise and signals detected from known volumes and cell populations to predict signals from different volumes and cell numbers of interest. The method uses an analytical solution of optical and acoustic propagation as well as target size and depth and yields, as recently described in ref. 24, a nonlinear dependence of signal strength with target volume. According to the spatio-temporal characteristics of the ultrasonic detector, the model assumed that the effective volume in the phantom of Fig. 2, from which the individual opto-acoustic signals were detected, contained on average ~$10^4$ cells and assumed a minimum detection limit corresponding to a CNR of 5 (that is, CNR < 5 does not constitute detection). In this case, the minimal detectable number of cells was found to be ~$10^3$. It was further calculated that, for achieving single cell detection sensitivity, the SNR of the system would need to be improved by a factor of ~2500, which corresponds to an equivalent increase of the signal or reduction of the noise floor by a factor of $\sqrt{2500} = 50$ (in rms voltage terms). Such an improvement is technically feasible and can be achieved by a combination of using

detectors of higher sensitivity, averaging over longer periods of time, or using larger arrays of detectors in parallel.

Multiwavelength imaging combined with selective-plane illumination offers the possibility of improving contrast, reducing out-of-plane and other imaging artifacts (see, for example, Fig. 3), as well as simultaneously resolving multiple FPs, dyes and other chromophores. In the applications shown, no photobleaching effects were observed, because the method operates with significantly less power per unit volume than that achieved with focused light, as in confocal microscopy. Although the spatial resolution in these studies was ~38 μm, broadband acoustic detectors constructed in arrays may lead to superior resolution and also offer real-time imaging capability, which is the goal of the next-generation setup. One important issue to be addressed regarding the accuracy of multispectral reconstruction is the wavelength dependence of the light distribution in tissue. As the MSOT method proposed herein capitalizes on the steep changes in absorption spectra of FPs in the vicinity of their excitation wavelength, it only needs very narrow spectral bands to operate efficiently (of the order of 30 nm). Within this spectral region the scattering properties of even very diffuse tissues are not expected to differ by more than 10% (assuming scattering is normally inversely proportional to the square of the wavelength), leading to corresponding fluence changes of less than 5%, as can be calculated by the light diffusion equation. However, if scattering variations in certain applications are higher, then correction on the data could be applied by corresponding adjustment of the photon diffusion model used to account for wavelength-dependent light propagation differences in the tissues due to scattering. In addition, because contrast is calculated in the spectral analysis on a relative per voxel basis, there is also low sensitivity to spatially varying scattering. Therefore, in contrast to conventional opto-acoustic imaging, MSOT is not affected significantly by possible scattering heterogeneity within the tissues or wavelengths used.

In comparison, surface-limited fluorescence microscopy methods or those applied to transparent or post mortem to chemically treated samples achieve better spatial resolution but offer penetration depths limited to less than one MFPL[25], that is, ~1 mm in the case of opaque living tissue. It is also possible to perform optical tomography through entire mice with high sensitivity, but low resolution[8,26] (~1 mm or worse). In contrast, selective-plane MSOT offers an imaging platform that is not limited by light diffusion and can achieve a penetration from several millimetres to potentially centimetres with a resolution that can vary practically in the range 20–100 μm. Importantly, the resolution achieved remains constant as a function of depth and depends only on the ultrasonic detector characteristics, that is, on bandwidth and sensitivity, as well as on the overall SNR achieved. MSOT therefore fills a significant area in biological imaging that goes well beyond the penetration limit of modern microscopy and could become the method of choice in studying signalling pathways and gene expression, morphogenesis, disease progression and many other targeted mechanisms through whole bodies of opaque living organisms and animals. It may not only significantly enhance the usefulness of currently existing transgenic FP lines, but may even call for the development of more reporters and probes that could tag, with higher flexibility, development, disease and aging-related processes.

## Methods

**Experimental setup and data acquisition.** The schematic of the experimental setup is shown in Fig. 1c. It uses an optical parametric oscillator (OPO) based laser (MOPO series, Spectra Physics Inc.), tunable in the visible and near-infrared region (430–1,800 nm) and capable of producing 8-ns pulses with a repetition frequency of 30 Hz. The imaged objects were fixed on the rotation stage, controlled by a stage controller (ESP-3000, Newport Corp.). The laser beam was passed through a variable-slit aperture, and focused using a cylindrically focusing lens onto a sample submerged in water, thus creating a planar sheet of light. Before entering the water tank, the beam was further homogenized in the imaged (horizontal) plane using a diffuser to reduce the effects associated with hot spots and other beam instability artifacts. Maximal light intensity at the surface of the imaged objects was ~5 mW mm$^{-2}$. The geometric focal line was extended for ~2–3 mm into the scattering object to allow maximal possible confinement of a planar light sheet within the acoustic detection plane (image plane). This kind of selective-plane illumination strategy is especially useful in cases where the studied organism presents high absorption contrast between different structures. This is because, for the first one or two millimetres, the light is only partially diffused as it passes through the scattering object, thus, signals coming from 'out-of-focus plane' absorptive structures are minimized. Each imaged object was illuminated by up to seven wavelengths spaced by 10 nm and located near the peak excitation of the particular FP being imaged; however, a minimum of three wavelengths are normally required for efficient spectral decomposition. Broadband ultrasonic transducers (Models V382 and V319, Olympus-Panametrics, 100% bandwidth, central frequencies 3.5 and 15 MHz, respectively), cylindrically focused at the optical illumination plane (confocal arrangement), were used to detect the opto-acoustic signals. The V382 transducer was used for phantom measurements while the V319 model served in other high-resolution *in vivo* experiments. The samples were rotated 360° with 3° steps to enable in-plane two-dimensional image reconstruction. Three-dimensional data acquisition was enabled by means of vertical scanning of both illumination and detection planes by mounting the transducer and a 45°-angled mirror onto a vertical translational stage. The recorded time-resolved signals were amplified, digitized and averaged by an embedded oscilloscope PCI card at 100 Msps (NI PCI-5122, National Instruments Corp.) with 14-bit resolution. To further reduce beam instability artifacts and increase the accuracy of multispectral reconstructions, a photodiode was used to detect pulse energy and all recorded signals were normalized with the actual light energy on a per-pulse basis. Planar image data acquisition normally took ~2 min at each wavelength.

**Image reconstruction.** A filtered backprojection algorithm[27] was used to reconstruct the detected opto-acoustic responses. Two-dimensional single-wavelength image reconstruction was carried out on a dual-core Pentium IV 3.2 GHz processor with 2 GB RAM, and typically required ~3 s on a 200 × 200 mesh. Because the raw opto-acoustic signals represent a combined contribution of light fluence and optical absorption, to extract more accurate optical absorption data it might be necessary to normalize the images by the light distribution in the object. It was, however, found that for *Drosophila* and zebrafish, due to their relatively small size, normalization for light distribution was not critical for the quality of the reconstructed images. This is because, in the range considered, the signal drop of the light sheet is not significant (less than an order of magnitude) so it does not significantly affect image quality through SNR deterioration. Nevertheless, correction for light distribution is essential for the 1.9-cm-diameter phantom to obtain contrast from the deep structures[28]. To facilitate the correction, we represent the initially reconstructed opto-acoustic image as a product between optical absorption distribution $\mu_a(\boldsymbol{r})$ and local light fluence $U(\boldsymbol{r})$. The latter is calculated using a finite-element method (FEM) solution to the light diffusion equation

$$\nabla^2 U(\boldsymbol{r}) - k^2 U(\boldsymbol{r}) = -q_0$$

where $k = \sqrt{3\mu_a(\mu_a + \mu_a')}$. The light source term $q_0$ is assigned onto the phantom boundary, directly extracted from the opto-acoustic image. For first-order correction, we further assume that the phantom has homogeneous a priori known background optical properties. The average background properties of an object can in principle be approximately measured by comparing the magnitude of the surface opto-acoustic response to the one recorded from a calibrated object with known optical properties. Subsequently, the initial images at each wavelength are normalized by the calculated light distribution to obtain quantified optical absorption data on a per-pixel basis. In cases with a highly heterogeneous background with unknown optical properties, iterative normalization methods have been suggested for planar boundary two-dimensional configurations[29], and were recently extended to three dimensions by iteratively feeding data from a segmented opto-acoustic image into the FEM-based light diffusion model[30].

The correct location and concentration of FPs was resolved by spectral processing of opto-acoustic images[21,31] obtained at $n$ discrete wavelengths $\lambda_1, \ldots, \lambda_n$. As mentioned, opto-acoustic measurements were taken in control animals containing no FPs to establish the spectral behaviour of the background absorption. It was subsequently assumed that every pixel $k$ in the opto-acoustic image represents a combined contribution of the FP and the background. This can be written in the form of $N$ linear equations:

$$\mu_a^k(\lambda_m) = \alpha_b(\lambda_m)c_b^k + \alpha_{FP}(\lambda_m)c_{FP}^k, \quad m = 1, \ldots, N$$

where $\mu_a^k(\lambda)$ is the reconstructed wavelength-dependent absorption in pixel $k$, $\alpha_b(\lambda)$ and $\alpha_{FP}(\lambda)$ are the molar extinction spectra of the FP and the background, and $c_b^k$ and $c_{FP}^k$ are the corresponding concentrations. Using the measured total absorption values and the known spectra for the measured wavelengths, the concentrations $c_{FP}^k$ of the FP and the background $c_b^k$ are subsequently reconstructed from the above linear equations on a per-pixel basis using a linear regression method. It should be noted that, although $\alpha_{FP}(\lambda)$ and $c_{FP}^k$ represent the actual molar extinction coefficient of the FP and its concentration, the measured background spectra $\alpha_b(\lambda)$ and the extracted

values of the concentration $c_b^k$ have arbitrary scale values and only their product $\alpha_b(\lambda)c_b^k$ has a real physical interpretation. Additional spectral contributions can be introduced by simply adding new terms to the spectral equations.

Received 27 November 2008; accepted 20 May 2009; published online 21 June 2009

## References


1. Giepmans, B. N. G., Adams, S. R., Ellisman, M. H. & Tsien, R. Y. The fluorescent toolbox for assessing protein location and function. *Science* **312,** 217–224 (2006).
2. Lichtman, J. W. & Conchello, J. A. Fluorescence microscopy. *Nature Methods* **2,** 910–919 (2005).
3. Conchello J. A. & Lichtman, J. W. Optical sectioning microscopy. *Nature Methods* **2,** 920–931 (2005).
4. Bahlmann, K. *et al.* Multifocal multiphoton microscopy (MMM) at a frame rate beyond 600 Hz. *Opt. Express* **15,** 10991–10998 (2007).
5. Minsky, M. Microscopy apparatus. US patent 3,013,467 (1961).
6. Denk, W., Strickler, J. H. & Webb, W. W. 2-photon laser scanning fluorescence microscopy. *Science* **248,** 73–76 (1990).
7. Helmchen, F. & Denk, W. Deep tissue two-photon microscopy. *Nature Methods* **2,** 932–940 (2005).
8. Ntziachristos, V., Ripoll, J., Wang, L. H. V. & Weissleder, R. Looking and listening to light: the evolution of whole-body photonic imaging. *Nature Biotechnol.* **23,** 313–320 (2005).
9. Hove, J. R. *et al.* Intracardiac hemodynamics are an essential epigenetic factor for embryonic cardiogenesis. *Nature* **421,** 172–177 (2003).
10. Jain, R. K., Munn, L. L. & Fukumura, D. Dissecting tumor pathophysiology using intravital microscopy. *Nature Rev. Cancer* **2,** 266–276 (2002).
11. Sharpe, J. *et al.* Optical projection tomography as a tool for 3D microscopy and gene expression studies. *Science* **296,** 541–545 (2002).
12. Huisken, J. *et al.* Optical sectioning deep inside live embryos by selective plane illumination microscopy. *Science* **305**, 1007–1009 (2004).
13. Dodt, H. U. *et al.* Ultramicroscopy: three-dimensional visualization of neuronal networks in the whole mouse brain. *Nature Methods* **4,** 331–336 (2007).
14. Editorial. Geneticist seeks engineer: must like flies and worms. *Nature Methods* **4,** 463 (2007).
15. Schroeder, T. Imaging stem-cell-driven regeneration in mammals. *Nature* **453,** 345–351 (2008).
16. Gusev, V. E. & Karabutov, A. A. *Laser Optoacoustics* (*American Institute of Physics*, 1993).
17. Zhang, E. Z., Laufer, J. G., Pedley, R. B. & Beard, P. C. *In vivo* high-resolution 3D photoacoustic imaging of superficial vascular anatomy. *Phys. Med. Biol.* **54,** 1035–1046 (2009).
18. Lao, Y., Xing, D., Yang, S. & Xiang, L. Noninvasive photoacoustic imaging of the developing vasculature during early tumor growth. *Phys. Med. Biol.* **53,** 4203–4212 (2008).
19. Wang, X. *et al.* Noninvasive laser-induced photoacoustic tomography for structural and functional *in vivo* imaging of the brain. *Nature Biotechnol.* **21,** 803–806 (2003).
20. Zhang, H. F., Maslov, K., Stoica, G. & Wang, L. V. Functional photoacoustic microscopy for high-resolution and noninvasive *in vivo* imaging. *Nature Biotechnol.* **24,** 848–851 (2006).
21. Razansky, D., Vinegoni, C. & Ntziachristos, V. Multispectral photoacoustic imaging of fluorochromes in small animals. *Opt. Lett.* **32,** 2891–2893 (2007).
22. Li, L., Zemp, R. J., Lungu, G., Stoica, G. & Wang, L. V. Photoacoustic imaging of lacZ gene expression *in vivo*. *J. Biomed. Opt.* **12,** 020504 (2007).
23. De La Zerda, A. *et al.* Carbon nanotubes as photoacoustic molecular imaging agents in living mice. *Nature Nanotechnol.* **3,** 557–562 (2008).
24. Razansky, D., Baeten, J. & Ntziachristos, V. Sensitivity of molecular target detection by multispectral optoacoustic tomography (MSOT). *Med. Phys.* **36,** 2891–2893 (2009).
25. Vinegoni, C., Pitsouli, C., Razansky, D., Perrimon, N. & Ntziachristos, V. *In vivo* imaging of *Drospophila melanogaster* pupae with mesoscopic fluorescence tomography. *Nature Methods* **5,** 45–47 (2008).
26. Ntziachristos, V., Tung, C.-H., Bremer, C. & Weissleder, R. Fluorescence molecular tomography resolves protease activity *in vivo*. *Nature Med.* **8,** 757–760 (2002).
27. Xu, M. & Wang, L. V. Universal back-projection algorithm for photoacoustic computed tomography. *Phys. Rev. E* **71,** 016706 (2005).
28. Razansky, D. & Ntziachristos, V. Hybrid photoacoustic fluorescence molecular tomography using finite-element-based inversion. *Med. Phys.* **34,** 4293–4301 (2007).
29. Cox, B. T., Arridge, S. R., Kostli, K. P. & Beard, P. C. 2D quantitative photoacoustic image reconstruction of absorption distributions in scattering media using a simple iterative method. *Appl. Opt.* **45,** 1866–1875 (2006).
30. Jetzfellner, T. *et al.* Iterative optoacoustic image normalization in non-uniform illumination configurations. *Appl. Phys. Lett.* **95,** (2009) (in the press).
31. Laufer, J. G., Delpy, D. T., Elwell, C. E. & Beard, P. C. Quantitative spatially resolved measurement of tissue chromophore concentrations using photoacoustic spectroscopy: application to the measurement of blood oxygenation and haemoglobin concentration. *Phys. Med. Biol.* **52,** 141–168 (2007).


## Acknowledgements

D.R. acknowledges financial support by the Deutsche Forschungsgemeinschaft (DFG) research grant RA 1848/1-1. M.D. is a fellow of the Studienstiftung des deutschen Volkes. R.W.K. is supported by a BioFuture Award Grant (0311889) of the German Ministry for Education and Research (BMBF). We thank R. Jagasia for providing Hela mitodsRed cells.

## Additional information

Supplementary information accompanies this paper at www.nature.com/naturephotonics. Reprints and permission information is available online at http://npg.nature.com/reprintsandpermissions/. Correspondence and requests for materials should be addressed to D.R. and V.N.

# Optical adhesives

The encapsulation of LEDs, termination of optical fibres and assembly of complex lens systems are all tasks that can be accomplished by the use of special optical adhesives, explains **Neil Savage**.

Adhesives are used throughout the manufacturing world, from bonding wires to circuit boards to sealing packages. In the photonics industry, they are used to attach optical components to fibres, to encapsulate LEDs, to provide conductive coatings on touch-screen displays, and to package arrays of LEDs or diode lasers. Often, as when they're bonding optical components such as lenses, they need to be optically clear, with a refractive index similar to the parts that they are sticking together.

Depending on the application, optical adhesives can be single-component materials that cure when exposed to ultraviolet or blue light, or multiple-component systems that undergo a chemical reaction and thus harden when mixed. They come in a wide variety of specifications with different values of hardness, viscosity and curing times available. Harry Arnon, president and CEO of Hernon Manufacturing, says that his company formulates 5,000 different adhesives as well as systems for dispensing them and machines for curing them. "Some need to be softer, some need to be rigid. Some have excellent adhesion to plastic, some need to have better adhesion to glass. Some need to go to high temperatures," he says.

Around 200 to 250 of the company's products are ultraviolet-curable, which Arnon says is a growing trend. He also says that many users want adhesives that fix in place in seconds, which is very important when trying to position components and fibres accurately. "Instead of placing something that you have to wait for a long time and hold it in place till the product cures, you can have a perfect mounting," he says. "The fact that they are one-component, solvent-free and cure on demand makes them very desirable for many applications."

Although the need for adhesives for the permanent assembly of complex systems is clear, it is perhaps not so obvious that they are also useful in temporary grinding, polishing and cutting applications. Instead of struggling to clamp a substrate or part, users can for example apply a temporary adhesive to hold it in place while it is processed.

As far as curing is concerned, the arrival of a new generation of long-wavelength ultraviolet and blue LEDs is cutting curing costs, because they are cheaper and have longer lifetimes than other ultraviolet sources, Arnon says.

MASTER BOND

The development of adhesives that shrink very little while curing has also proved important, says Jon Galaska, programme manager for electronics (which includes optics) at Dymax. It means users can position components and know that they won't move when the adhesive hardens. Typically, he says, there has been a trade-off, where low shrinkage meant a longer curing time, which increased the risk of the components moving. The latest products, however, are fast-curing and low shrinkage at the same time, he says.

The downside of ultraviolet-cured adhesives is that they are more costly and require some sort of light source for curing. They also don't work in certain applications, such as potting, in which a component is placed inside a slot, because the ultraviolet light cannot reach all the material. That instead is a task for epoxies. Another common task for epoxies is to form domes over components, as is the case for LED encapsulation. "If you're getting into applications requiring very high chemical resistance or high temperature, you would definitely want to go with epoxies," Galaska says.

## PRODUCT ROUND-UP

A two-component epoxy adhesive for high-performance bonding applications, EP30 from **Master Bond** (Hackensack, New Jersey, USA) is used for bonding optical elements, as well as for potting and encapsulating electronic components. The company says that the epoxy has excellent adhesion to a wide variety of substrates, including glass, ceramics, metals and many plastics. It has a viscosity of 400 to 500 centipoise (cP) at room temperature. It has a cure time of 1–2 h at 93 °C and is stable from –51 °C to 121 °C. The mix ratio is 100:25 and preparation takes 25–30 min. It offers high chemical resistance, hardness, optical clarity and electrical insulation, and low shrinkage on cure. Typical lap shear strength is over 3,000 psi for aluminium-to-aluminium bonds. It is especially suited for assemblies that use only very thin bond lines.
**www.masterbond.com**

An optically clear silicone rubber encapsulant, Opti-tec 7020 from **Intertronics** (Oxfordshire, UK) is a two-part, clear liquid silicon that cures in 1 h at a temperature of 100 °C. Its combination of transparency and non-yellowing make it suitable for encapsulation of sensitive optoelectronic parts, such as LEDs.

It can also be used for solar panel applications and in optical assembly. It has a 10:1 mixing ratio and suits hand mixing as well as automatic dispensing equipment. Part A has viscosity of 4,000 cP and part B a viscosity of 500 cP; when mixed it is easily poured. The specific gravity is 1.02 for part A and 1.00 for part B. It has a shelf life of 12 months at ambient temperatures when unopened, and a pot life (ready for use once mixed) of 4 h. It cures to a Shore A hardness of 40, is good for a temperature range of –60 °C to 200 °C, and has a tensile strength of 750 psi, linear shrinkage of ~0.1%, refractive index of 1.406 and thermal conductivity of 0.18 W $m^{-1}$ $K^{-1}$.
**www.intertronics.co.uk**

EXFO

The OmniCure LX300 LED ultraviolet spot-curing system from **EXFO** (Quebec, Canada) incorporates up to four LED heads and uses LEDs with a maximum intensity of 8,000 mW $cm^{-2}$. Optimized monitoring and cooling provide a guaranteed life of 10,000 h, although the estimated life is 20,000 to 40,000 h. The system constantly monitors its temperature and has built-in overheat protection. The front panel controls do not require extensive operator training. It has a programmable trigger with an adjustable countdown range from 999.9 s to 0.1 s in 0.1-s intervals, and both a button and a foot pedal to start or stop LED emission. The system can be used as a stand-alone device or incorporated into automated manufacturing lines. When operating at full power, it consumes less than 72 V A. It is RoHS and CE compliant.
**www.exfo-omnicure.com**

The WaferGrip thin-film adhesive from **Dynatex International** (Santa Rosa, California, USA) is a composite film adhesive engineered to bond optics, wafers and other substrates during dicing, grinding, lapping and polishing. It is a heat-activated ethylene vinyl acetate polymer and comes in various thicknesses and sizes. It is available as an adhesive on a polyester backing or as an adhesive film on release paper. After the part has been processed, the film can be stripped from the substrate by placing it in WaferGrip Stripper for 10–45 min at 75 °C to 110 °C. Other chemicals used in semiconductor wafer processing can also be used as strippers. An electrically conductive version reduces static discharge. The film comes in thicknesses of 0.8 ± 0.2, 1.35 ± 0.15 and 3 ± 0.2 mil (1 mil being a thousandth of an inch or 25.4 μm).
**www.dynatex.com**

**Norland Products** (Cranbury, New Jersey, USA) offers a variety of ultraviolet-curable optical adhesives such as Norland Optical Adhesive 71. The optically clear liquid adhesive cures with ultraviolet light with a wavelength between 315 and 400 nm, with peak absorption at 365 nm. The total energy of ultraviolet light required for a full cure is 3.5 J $cm^{-2}$. The adhesive is designed for bonding applications that require optical clarity or fast curing and long-term stability over a wide range of temperatures. Typical applications include laminating solar cells, holographic plates, flat panel displays and touch screens. Medium-pressure mercury lamps or D lamps can cure the material in seconds. Lower-intensity sources such as fluorescent black lights can provide a cure in 10–15 min. The material has a viscosity of 200 cP at 25 °C. Refractive index of the cured polymer is 1.56.
**www.norlandprod.com**

**Epoxies Etc** (Cranston, Rhode Island, USA) offers a non-yellowing adhesive and potting compound called UV Cure 60-7108 which is designed for fibre-optic and electronic assemblies that require a clear adhesive or potting. It offers excellent adhesion for glass and polycarbonates, as well as aluminium, copper and PVC. It cures in 12 s under ultraviolet spot cure and 10 s in a conveyor system. It has a viscosity of 800 cP at 25 °C, tensile strength of 3,300 psi, elongation at failure of 90%, Shore D hardness of 80, operating temperature range of –50 °C to 155 °C, dielectric strength of 450 V per mil, dielectric constant of 4.5 at 60 Hz and volume resistivity of $5 \times 10^{16}$ Ω cm at 25 °C. Its expected shelf life is one year when stored below 30 °C in its original, unopened container, and refrigerated storage will extend the shelf life.
**www.epoxies.com**

Ultrabond 57112 from **Hernon Manufacturing** (Sanford, Florida, USA) is a fast-curing adhesive that forms a clear, impact-resistant bond with high light transmittance and a refractive index similar to glass. It can be used to bond glass components to glass or other substrates. Uncured, it is a modified acrylic resin in a clear liquid with a viscosity of 800 to 1,200 cP at 25 °C, a specific gravity of 1.04 and a refractive index of 1.48. Exposing it on glass slides to ultraviolet light of 100 mW $cm^{-2}$ at 365 nm results in a fixture time of 5 s or less. It has a Shore D hardness of 60 and a temperature range of –55 °C to 149 °C. Its shear strength for glass-to-glass bonds is 650 psi. It is resistant to prolonged immersion in water.
**www.hernonmfg.com**

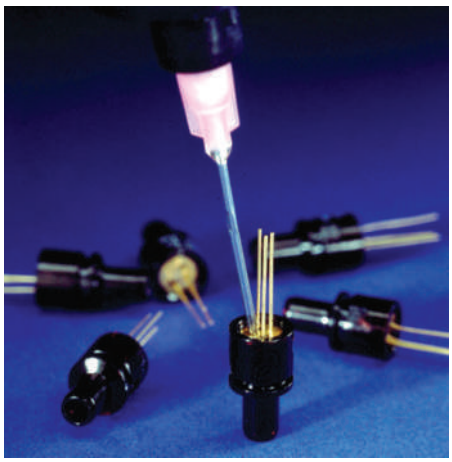
DYMAX

The OP-67-LS optical-mechanical adhesive from **Dymax** (Torrington, Connecticut, USA) is designed to hold components in place during optical assembly and in subsequent thermal cycling. It is designed as a low-shrinkage compound to virtually eliminate movement, and it cures in seconds with ultraviolet and visible light exposure. The uncured white acrylated urethane paste has no non-reactive solvents and is soluble in organic solvents. It has a density of 1.14 g $ml^{-1}$ and a nominal viscosity of 135,000 cP at 20 rpm. Once cured, it has a Shore D hardness of 80, a tensile strength of 4,000 psi, an elongation at break of 6.5% and a modulus of elasticity of 83,000 psi. Its water absorption over 24 h is 2.3% at 25 °C. Linear shrinkage is 0.2%. It adheres to various substrates, including acrylic and other plastics, and has low outgassing. Typical applications include alignment of optics and lenses, positioning of vertical-cavity surface-emitting lasers and prisms.
**www.dymax.com**

NEIL SAVAGE is a freelance science and technology journalist based in Lowell, Massachusetts, USA.

*The mention of a company's name or product is not an endorsement by* Nature Photonics *and* Nature Photonics *takes no responsibility for the accuracy of the product information or the claims made by companies.*

# Programmable liquid optical interfaces

*Nature Photonics* spoke to Carl Brown from Nottingham Trent University about the creation of a voltage-programmable liquid-oil surface that can rapidly switch and deflect light beams.

**What was the motivation for this work?**
Previously I was working on liquid crystals and was interested in using them to make displays and other voltage-configurable elements. When I came to Nottingham Trent University in 2003, I learnt that Glen McHale and Mike Newton were manipulating liquid droplets by electrowetting and were also interested in micro- and nanostructured superhydrophobic surfaces. We had the idea of investigating isotropic liquids and using them to make simple devices that would modulate the phase of light independent of the light's polarization. And we wanted liquid surfaces that were reconfigurable yet avoided the need for a contact line between the solid and the fluid surface.

**What are the current approaches for making reconfigurable optical elements?**
Well, actually there is a plethora of what you might call 'actuated technologies' out there: electro-acoustic and magneto optic modulators, various liquid-crystal devices based on different phases and geometries, micro-electromechanical devices and others. Each of these techniques performs well in specific applications. There are always trade-offs between size of components, speed, robustness, power consumption, stability and so on.

**Tell us about your approach.**
Our approach is based on liquid dielectrophoresis, which generates forces in a dielectric medium where there are gradients in the electric field. Our structure consists of an array of striped electrodes. Every other electrode is earthed and the one between we bias with a voltage. Between these electrodes there are strong and highly non-uniform fields, not unlike those at the edges of capacitor plates. What we do is coat the electrodes with a film of oil, and this fluid tends to gather in the region between the electrodes because that is where the strongest dielectrophoretic forces are. That in turn removes fluid from the regions directly above the electrodes, and as a result you get a wrinkle on the surface of the oil film.

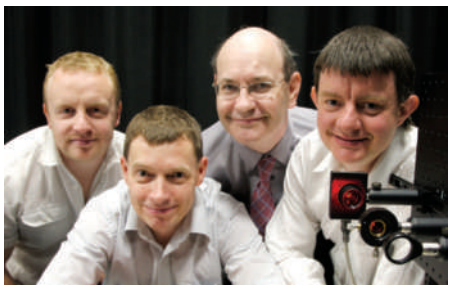

NOTTINGHAM TRENT UNIVERSITY

From left to right: Gary Wells, Michael Newton, Glen McHale and Carl Brown.

**What has been achieved with this scheme?**
We have demonstrated reconfigurable and switchable reflection and diffraction from our surface. To switch a first-order diffracted wave's intensity we've typically used a drive voltage of 70 $V_{rms}$ for a reflective device, or 190 $V_{rms}$ for a transmissive device. The undulation on the surface of the oil can be absolutely static and stable, and we can reproducibly reprogramme the amplitude of the wrinkle just by adjusting the potential between neighbouring electrodes. In our present work we consider oil films from 8 to 45 μm in thickness and in those we can obtain peak-to-peak height of wrinkles of up to about 5 μm. Gary Wells, who carried out and co-designed the experimental investigations as part of his PhD project, came up with a neat method to pre-stretch the oil into a thin uniform film. Unlike in some other techniques, including electrowetting, we don't need to make electrical contact with any fluids in the system. We also don't have a movable contact line between our fluid and the solid surface. In electrowetting devices you need a thin dielectric layer that is capable of withstanding high electric fields. We have used a thin dielectric layer, but we don't think this is essential, because the oil film itself effectively acts as the dielectric and we use much lower electric field strengths than would cause dielectric breakdown.

**How rapidly can you modify the profile?**
The fastest speeds we have demonstrated are for switching on the wrinkle in 35 μs and relaxing (switching off) the wrinkle about 80 μs. In other words, if you use the periodic wrinkle as a diffraction grating, you can modulate the intensity of a first diffracted order at frequencies of about 12 kHz. A decrease in the switching speed by a factor of 10 does look feasible, but we don't know beyond that.

**What surface profiles can be made?**
At first we demonstrated a sinusoidal pattern down to 20 μm in period. The fundamental physics doesn't change down to the micrometre scale and perhaps lower. The technical challenge is to get thinner films of oil that are uniform.

We have also demonstrated non-sinusoidal profiles, but if we introduce more gradients of the field, that costs in terms of energy. There is more work to be done there. There was a recent paper by Heikenfeld and collaborators (*Nature Photon.* **3,** 292; 2009) showing that you can make a pixellated fluidic device with individual micrometre-scale reservoirs, so we need not be limited by mass conservation. We think there is a lot more that can be done in this direction. We have shown one-dimensional profiles so far, but we think we can go to two dimensions as well.

**What are the applications and what are the next steps forwards?**
We think that there are applications for optical switches and miniature projection displays, and potentially on a different scale for programmable lenticular screens to switch a display between two-dimensional and three-dimensional views.

We are looking at going to shorter pitches and more arbitrary profiles, and going to two dimensions. In a practical device, you may need to operate it in any orientation. In that case you need to look at using an interface between two density-matched fluids. Creating the wrinkles at liquid–liquid interfaces is going to involve some interesting and challenging physics, we think.

INTERVIEW BY DAVID PILE

*Carl Brown and his colleagues have a Letter on reconfigurable liquid surfaces on page 403 of this issue.*